

6-24-2015

Electrochemical Investigation of Homogenous Species at an Electrode Interface

Christopher Larsen III

Follow this and additional works at: https://digitalrepository.unm.edu/chem_etds

 Part of the [Physical Chemistry Commons](#)

Recommended Citation

Larsen, Christopher III. "Electrochemical Investigation of Homogenous Species at an Electrode Interface." (2015).
https://digitalrepository.unm.edu/chem_etds/41

This Dissertation is brought to you for free and open access by the Electronic Theses and Dissertations at UNM Digital Repository. It has been accepted for inclusion in Chemistry ETDs by an authorized administrator of UNM Digital Repository. For more information, please contact disc@unm.edu.

Christopher A. Larsen III

Candidate

Chemistry & Chemical Biology

Department

This dissertation is approved, and it is acceptable in quality and form for publication:

Approved by the Dissertation Committee:

Richard Kemp

, Chairperson

Martin Kirk

Ramesh Giri

Zachary Sharp

Electrochemical Investigation of Homogenous Species at an Electrode Interface

BY

CHRISTOPHER ALAN LARSEN III

Bachelor of Science in Chemistry
University of New Mexico
2010

DISSERTATION

Submitted in Partial Fulfillment of the
Requirements for the Degree of

**Doctor of Philosophy
Chemistry**

The University of New Mexico
Albuquerque, New Mexico

April 6, 2015

“Misfortune is needed to plumb certain mysterious depths in the understanding of men; pressure is needed to explode the charge. My captivity concentrated all my faculties on a single point. They had previously been dispersed, now they clashed in a narrow space; and, as you know, the clash of clouds produces electricity, electricity produces lightning and lightning gives light.”

The Count of Monte Cristo, Alexander Dumas

First and foremost, I would like to thank my advisor, Dr. Richard Kemp, for all his vision and solidarity while working with me on this project. It was his intuition and keenness that inspired me to join the ranks of the UNM chemistry graduate students, and it was his belief in me that enabled me to persevere through challenges that presented themselves during my tenure.

I would also like to extend my gratitude to the post-doctoral fellows of our research group: To Dr. Diane Dickie, whose training and insight led to a firm foundation of scientific principles and practices. To Dr. Brian Barry, who aided me in the day-to-day problem solving and details of the project. And to Dr. Elizabeth Donovan, whose expertise in electrochemistry techniques proved invaluable in my research.

I would like to thank Dr. Thomas Peng, the principal investigator of the reversible mirror technology at the Air Force Research Laboratory, for trusting me and allowing me the freedom to investigate silver deposition on transparent conductors. His guidance and mentoring proved invaluable in my future pursuits as a scientist. I also thank the undergraduates who worked with me on this project: Rafal Dziedzic (University of Wisconsin) and Sarah Blair (University of New Mexico).

To the members of the Kemp group over the years: Dr. Raymond Lansing, Dr. Agnes Mrutu, Dr. Marie Parks, Nancy Bush, Aruny Loch, Regina Frances, Kira Hughes, Nicholas Cosgrove, Ujwal Chadha, Dr. Jerome Lisena, and Dr. Santosh Gurung. Thank you for your smiles, dedication, and advice.

To my ever-supportive wife, Jessica, I owe a thousand parades of thanks for her support and dedication. When the walls of academia began to bear down upon me, she was there as a stable anchor. This dissertation could not have become a reality without her confidence in me.

Electrochemical Investigation of Homogenous Species at an Electrode Interface

Christopher Alan Larsen III

B.S., Chemistry, University of New Mexico, 2010

Ph.D., Chemistry, University of New Mexico, 2015

ABSTRACT

CO₂ reduction is a pressing problem worldwide, and one obstacle in the electrochemical conversion of CO₂ to more useful C₁ products such as methanol and formic acid is the kinetic barrier known as overpotential. The overpotential of rearranging the nuclei in CO₂ to accommodate electron transfer can be lowered by pre-bending the CO₂ molecule in an adduct-mediated complex. The work presented in Part I utilizes a combination of hard and soft donors on pincer-like ligands to effect the bending of CO₂ prior to electrochemical reduction. A large majority of the work consists of using Group 4 metallocenes, but Chapter 3 outlines Zn-based compounds that also show promise in the reduction of CO₂.

A refined methodology has been employed to increase the yield of the ligand 2-di-*tert*-butylphosphinophenol. Previous literature preparations could only accommodate approximately 1 g of product per batch, but by using the methodology found in this dissertation, the ligand can now be synthesized in large batches (>15 g). 2-diisopropylphosphinothiophenol and 2-diphenyl-

phosphinothiophenol were synthesized for the first time by our group, and their utility was explored in relation to Group 4 metallocenes.

The work presented in Part II of this dissertation illustrates the usefulness of homogenous electrochemical interactions in space-based applications. New ventures toward reversible electrochemical mirror (REM) technology were explored using silver and copper cations solvated between two transparent conductive films. Silver deposited upon these conductive thin films to produce seamless mirrors, and by controlling silver nanoparticle growth clusters with ramping voltages, thin colored films were also deposited.

Table of Contents

ACKNOWLEDGEMENTS.....	iii
ABSTRACT	iv
TABLE OF CONTENTS	vi
LIST OF FIGURES	x
LIST OF TABLES	xiv
LIST OF SCHEMES	xv
LIST OF ABBREVIATIONS	xvi
PART 1: ELECTROCHEMICAL REDUCTION OF METAL-CO₂ ADDUCTS	1
Chapter 1: Introduction	2
1.1 The Need for CO ₂ Mitigation	2
1.2 Electrochemistry	7
1.3 Electrocatalysis	12
1.4 A Sampling of Electrocatalysis Efforts in CO ₂ Reduction	15
1.4.1 Titanium Oxide	16
1.4.2 Silver Metal.....	17
1.4.3 Gold Oxide.....	18
1.4.4 Copper.....	19
1.4.5 Homogenous Catalytic Reduction of CO ₂	20
1.5 Forming a CO ₂ Adduct	22

Chapter 2: Group 4 Transition Metal Complexation and Electrochemical Investigations	28
2.1 Ligand Preparations and Synthesis.....	28
2.1.1 Aromatic Structural Foundation for Ligand Synthesis	29
2.1.2 Development of OCCP/SCCP Bidentate Ligand Structures	34
2.1.3 Ligand Trends Through ³¹ P NMR Spectroscopy	39
2.2 Preparation of the Metal Complex.....	42
2.3 Analysis of Neutral Metal-Ligand Complexes.....	46
2.3.1 Titanocene Complexes.....	46
2.3.2 Zirconocene Complexes.....	52
2.3.3 Hafnocene Complexes	57
2.4 Analysis of Cationic Metal-Ligand Complexes	66
2.4.1 Titanocenium Complexes	68
2.4.2 Zirconocenium Complexes	71
2.4.3 Hafnocenium Complexes	75
Chapter 3: Zn(II) Complexes Used in CO ₂ Reduction	77
3.1 Introduction.....	77
3.2 Ligand and Complex Preparation	78
3.3 Results and Discussion	80
3.4 Summary and Future Work	89
Chapter 4: Experimental.....	90
4.1 Ligand Syntheses.....	90

4.2 Neutral Group 4 Metallocene Complexes.....	96
4.2.1 Titanocene Complexes.....	96
4.2.2 Zirconocene Complexes.....	100
4.2.3 Hafnocene Complexes	105
4.3 Group 4 Metallocenium Complexes	109
4.3.1 Titanocenium Complexes.....	111
4.3.2 Zirconocenium Complexes	115
4.3.3 Hafnocenium Complexes	119
4.4 Zn Complexes	122
4.4.1 Electrochemical Conditions and Analytical Methods.....	124
4.4.2 Calculation of Turnover Frequency	125
PART II: INVESTIGATION OF ORGANIC-BASED REVERSIBLE	
ELECTROCHEMICAL MIRRORS.....	126
Chapter 1: Introduction	127
1.1 Electroplating: Societal and Industrial Role	127
1.2 Optical Modulation of Smart Windows.....	130
1.3 Space Weather’s Effects on Space Vehicle Components.....	132
1.3.1 Cosmic Rays	132
1.3.2 Solar Events	133
1.3.3 Micrometeorites and Space Debris	135
1.4 Heat Transfer in Space.....	136
1.5 Electrophoretic Deposition in Fine-Tuning Thermal Control.....	139

Chapter 2: Results and Discussion	142
2.1 Electrolyte Performance	142
2.2 Optical Properties	149
2.3 Spot Deposition and Mirror Migration	157
Chapter 3: Experimental	159
3.1 Summary and Future Work	161
Appendix 1	163
Appendix 2	166
Appendix 3	167
References	168

List of Figures

Figure 1: Anthropogenic greenhouse gas emission shares	2
Figure 2: The electrical double layer	8
Figure 3: Time vs. potential plot of a general CV	10
Figure 4: CV of ferrocene	11
Figure 5: Catalyzed vs. uncatalyzed pathways	13
Figure 6: Total impedance as resistors in a circuit	15
Figure 7: Methanol production using titania nanoparticles	16
Figure 8: Ethanol & methanol production using silver electrodes.....	17
Figure 9: Formation of CO using gold oxide nanoparticles	18
Figure 10: Methanol production using copper oxide nanoparticles	19
Figure 11: Pyridine reactivity toward CO ₂	21
Figure 12: M/z distribution of C ₁ products using pyridinium	22
Figure 13: Amphoteric nature of CO ₂	22
Figure 14: PNP ligand bonding modes.....	23
Figure 15: Crystal structure of Sn complex	25
Figure 16: Structure of benzene	29
Figure 17: Effect of electron donating group on benzene.....	30
Figure 18: Effect of electron withdrawing group on benzene	31
Figure 19: Directed <i>ortho</i> metalation	32
Figure 20: Resonance effect on phenolate.....	33
Figure 21: Six ligands used in metallocene complexation.....	34

Figure 22: Crystal structure of 1	38
Figure 23: ^{31}P NMR spectroscopy comparison of 1-6	41
Figure 24: Generic dichlorometallocene	42
Figure 25: CV of complex 8 under Ar(g) and CO ₂ (g)	48
Figure 26: CV of complex 9 under Ar(g) and CO ₂ (g)	49
Figure 27: CV of complex 11 under Ar(g) and CO ₂ (g)	50
Figure 28: CV of complex 12 under Ar(g) and CO ₂ (g)	51
Figure 29: CV of complex 13 under Ar(g) and CO ₂ (g)	52
Figure 30: ^{31}P NMR comparison of 13 under Ar(g), CO ₂ (g), and electrolysis	54
Figure 31: Mass spectrum of electrolysis product of 13	55
Figure 32: CV of complex 14 under Ar(g) and CO ₂ (g)	56
Figure 33: Crystal structure of complex 17	57
Figure 34: CV of complex 24 under Ar(g) and CO ₂ (g)	58
Figure 35: CV of complex 19 under Ar(g) and CO ₂ (g)	59
Figure 36: IR spectra of complex 19 under Ar(g) and CO ₂ (g)	60
Figure 37: ^{31}P NMR comparison of 19 under Ar(g), CO ₂ (g), and electrolysis	61
Figure 38: ^1H NMR comparison of 19 under Ar(g) and CO ₂ (g)	62
Figure 39: Proposed CO ₂ complex with 19	63
Figure 40: Mass spectrum of electrolysis product of 19	64
Figure 41: CV of complex 9⁺ under Ar(g) and CO ₂ (g)	69
Figure 42: CV of complex 12⁺ under Ar(g) and CO ₂ (g)	70
Figure 43: CV of complex 13⁺ under Ar(g) and CO ₂ (g)	72

Figure 44: CV of complex 15⁺ under Ar(g) and CO ₂ (g)	73
Figure 45: Crystal structure of complex 17⁺	74
Figure 46: CV of complex 21⁺ under Ar(g) and CO ₂ (g)	75
Figure 47: Structure of Ph ₂ Ppy	77
Figure 48: Structure of PhPpy ₂	77
Figure 49: Structure of complex 25	78
Figure 50: Structure of complex 26	79
Figure 51: Crystal structure of complex 25	79
Figure 52: Crystal structure of complex 26	79
Figure 53: CV comparison of reduction potentials for complexes 25 and 26	81
Figure 54: CV of the entire electrochemical window for 25 and 26	82
Figure 55: CV of 25 with inset diffusion curve	82
Figure 56: IR spectra comparison of complex 25 before and after CO ₂	83
Figure 57: CV comparison of complex 25 before and after CO ₂	84
Figure 58: LSV of complex 25	84
Figure 59: Current vs. concentration plot of 25	85
Figure 60: Mass spectra before and after electrolysis of complex 25	86
Figure 61: Acetic acid addition to complex 25	87
Figure 62: Water addition to complex 25	88
Figure 63: CV of complex 26 before and after CO ₂	88
Figure 64: Electroplated gold dome	127
Figure 65: Survey of ITO research since 1991	129

Figure 66: Illustration of a two-stage electrochromic window	131
Figure 67: NASA space investments dedicated to solar flare warning	133
Figure 68: Total space debris tracked by the Department of Defense	135
Figure 69: Reversible mirrors' utility in space	141
Figure 70: CV of DMSO-based electrolyte at different potential rates.....	142
Figure 71: Diffusion test.....	143
Figure 72: CV of each component of the DMSO electrolyte.....	144
Figure 73: Labeled regions of REM redox.....	144
Figure 74: Weekly CV of REM solution	145
Figure 75: Stabilization CV of REM solution.....	146
Figure 76: Reversible stepping voltages for REM device.....	147
Figure 77: Plating distances for REM device.....	148
Figure 78: IR spectra through REM device after different plating times	150
Figure 79: Natural dissolution of the silver mirror	151
Figure 80: Possible geometries of plating deposition	152
Figure 81: Edge vs. center plating.....	153
Figure 82: Teflon housing used in REM experiments.....	154
Figure 83: Transmittance control.....	154
Figure 84: Visible light reflectivity	155
Figure 85: Various optical properties provided by the REM device	156
Figure 86: Mirror migration	158
Figure 87: Full transparency REM device	159
Figure 88: Exploded side-view of the REM device	160

List of Tables

Table 1: Reduction parameters for free CO ₂	5
Table 2: Numbering of mono-substituted Group 4 complexes	45
Table 3: ³¹ P NMR comparison of complexes 7—24	65
Table 4: Thermal conductivities of an array of metals	138

List of Schemes

Scheme 1: Bidentate attachment of a PNP ligand	24
Scheme 2: CO ₂ attachment to a zirconocenium complex	27
Scheme 3: Synthesis of ligands 4-6	35
Scheme 4: Attempted pathway for ligands 1-2	36
Scheme 5: Literature preparation of ligand 1	37
Scheme 6: Lithiation of 1 st and 2 nd row metallocenes	42
Scheme 7: Grignard reaction for 3 rd row metallocene lithiation	43
Scheme 8: Typical reaction of metallocene complexation.....	43
Scheme 9: Proposed CO ₂ insertion reaction	44
Scheme 10: Byproduct of dimethylanilinium salts with Group 4 metals	67
Scheme 11: Formation of cationic Group 4 metallocenes	68
Scheme 12: Proposed mechanism for CO ₂ attachment to 25	83

List Of Abbreviations (in order of appearance)

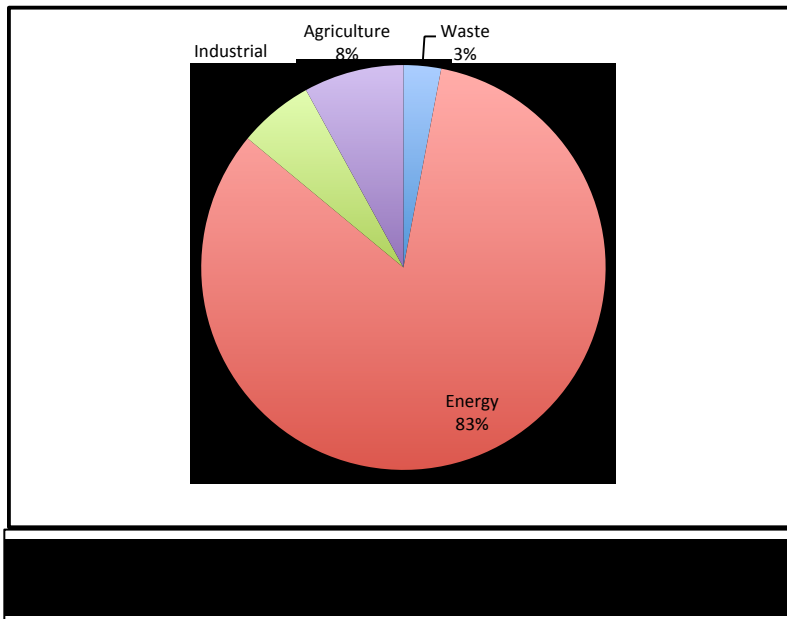
IGCC	Integrated Gasification Combined Cycle
HCOOH	Formic Acid
HCHO	Formaldehyde
NHE	Normal Hydrogen Electrode
ΔG	Gibbs Free Energy
DFT	Density Functional Theory
GC/MS	Gas Chromatography-Mass Spectrometry
HSAB	Hard and Soft Acid/Base
RHE	Reversible Hydrogen Electrode
n-PrOH	1-Propanol, $\text{CH}_3\text{CH}_2\text{CH}_2\text{OH}$
SCE	Saturated Calomel Electrode
R	Organic Substituent, used in chemical formulae
THF	Tetrahydrofuran, $\text{C}_4\text{H}_8\text{O}$
i-Pr	Isopropyl, $\text{CH}(\text{CH}_3)_2$
t-Bu	<i>tert</i> -Butyl, $\text{C}(\text{CH}_3)_3$
Ph	Phenyl, (C_6H_5)
Cp	Cyclopentadienyl ⁻ , $(\text{C}_5\text{H}_5)^-$
STP	Standard Temperature and Pressure (273.15 K and 1.00 atm)
FLP	Frustrated Lewis Pairs
<i>o</i>	<i>ortho</i> , adjacent groups in a phenyl ring
<i>m</i>	<i>meta</i> , occupying positions 1 and 3 in a phenyl ring
<i>p</i>	<i>para</i> , occupying positions 1 and 4 in a phenyl ring
DOM	Directed <i>ortho</i> Metalation
TMEDA	N,N',N'',N'''-Tetramethylethylenediamine, $\text{C}_6\text{H}_{16}\text{N}_2$
Cy	Cyclohexane, C_6H_{12}
MOM	Methoxymethyl Ether, $\text{CH}_3\text{OCH}_2\text{OCH}_3$
MeOH	Methanol, CH_3OH
CV	Cyclic Voltammetry
LSV	Linear Sweep Voltammetry
DTBP	2,6-di- <i>tert</i> -butylpyridine, $\text{C}_{13}\text{H}_{21}\text{N}$
BArF	Tetrakis(pentafluorophenyl)borane, $\text{B}(\text{C}_6\text{F}_5)_4^-$
CPE	Controlled Potential Electrolysis
ITO	Indium Tin Oxide

PART I: Electrochemical Reduction Of Metal-CO₂ Adducts

Chapter 1: Introduction

1.1 The Need for CO₂ Mitigation

As urbanized populations steadily increase worldwide, the need for high energy output also increases. A majority of the world's current energy output is derived from burning fossil fuels, inevitably producing carbon dioxide (CO₂), methane (CH₄), and other greenhouse gases in the waste stream. According to the International Energy Agency (IEA), global demand for fossil fuel-based energy is expected to be at 76% in 2035, while the remaining 24% will be from



low-carbon sources, such as nuclear and renewables.¹ Currently, the global energy demand for fossil fuel-based energy is at 82%, and even though this is a 6% decrease in expected reliance

upon fossil fuels, population projections model a 21% increase in world population in 2035.² In 2011, the emission of CO₂ due to anthropogenic activities equaled more than 31,000 Mt (megatons).³ Figure 1 displays the breakdown of

anthropogenic greenhouse gas emissions, and within the energy sector, 43% of greenhouse gas emission originates from coal combustion, 36% from oil, and 20% from gas. An abundance of greenhouse gases will lead to severe long-term effects on climate and living conditions across the globe,⁴ with climate change predicted to have adverse effects on all ecosystems of life, including the oceans,⁵ rain forests,⁶ deserts,⁷ tundras,⁸ plains,⁹ mountainous regions,¹⁰ and all other ecosystems in-between. Since the world will only see a projected 6% decrease in the demand of these non-renewable energy sources, it is the hope that scientists will be able to develop a method to transform, reduce, and/or sequester greenhouse gases so as to curb global climate change.

In order to reduce the amount of greenhouse gas production, higher efficiency power plants and methods need to be utilized. IGCC (Integrated Gasification Combined Cycle) coal power plants, for example, are capable of turning coal into synthesis gas (a mixture of carbon monoxide and hydrogen), making the purification of the carbon source more efficient. Mercury and sulfur dioxide emissions are greatly reduced as well. The problem with converting the world's coal power plants is that it would be extremely cost-prohibitive, and the products of the synthesis gas will still eventually produce CO₂, and so the problem will still persist. From a commercial and residential standpoint, consumers and companies can be educated about greenhouse gas emissions and can reduce their carbon footprints by reducing the amount of climate control for buildings like air conditioning and heating (better insulation and other

technologies would help in this effort), driving more fuel-efficient vehicles, and developing a more conscious attitude toward energy use. Again, these may help mitigate but do not solve the problem, and these attitude changes are merely a drop in the bucket when considering burgeoning industrialized countries like China and India that do not have the same education and infrastructure on greenhouse gas emission and their consequences. The reduction of CO₂, in a chemical sense rather than the literal decrease in the production of CO₂, is a problem scientists the world over have been researching for decades, but this will provide the avenue toward a drastic decrease in greenhouse gas production.¹¹

Some scientists have suggested that carbon sequestration will curb anthropogenic climate change. Sequestering CO₂ is the process of separating and capturing CO₂, typically from a bulk mixture of gases. Many advances have been made in this field,^{12,13} but the technology will be essentially useless if the sequestered carbon cannot be utilized, as large CO₂-dumps in oceans or caves would prove to be only a short-term solution. Proposals have been issued for high-efficiency carbon capture techniques including zeolites,¹⁴ metal-organic frameworks,¹⁵ and inorganic selective membranes,¹⁶ but none of these proposed pathways even suggest a route to converting the carbon source to a more useful product after its capture. Carbon capture, coupled with the catalytic reduction of the molecule to useful chemicals like fuels or precursor chemicals (such as ethylene, a precursor chemical for the production of polyethylene, one of the world's most abundant plastics) is the only viable option to enable energy

independence for burgeoning communities and established metropolises while conjointly curbing greenhouse gas accumulation in the atmosphere.

CO₂ reduction is an energetically unfavored reaction. Thermodynamic and kinetic obstacles abound in the direct reduction of CO₂ to useful organic compounds. Thermodynamically, CO₂ is very stable, and proton-coupled multi-electron steps are generally more favored in a direct reduction than single electron reductions because more stable products are formed.¹⁷ Table 1 displays

CO₂ + 2H⁺ + 2e⁻ → CO + H₂O	E° = -0.53V	ΔG°_{cell} = 102.3 kJ/mol
CO₂ + 2H⁺ + 2e⁻ → HCOOH	E° = -0.61V	ΔG°_{cell} = 117.7 kJ/mol
CO₂ + 4H⁺ + 4e⁻ → HCHO + H₂O	E° = -0.48V	ΔG°_{cell} = 185.3 kJ/mol
CO₂ + 6H⁺ + 6e⁻ → CH₃OH + H₂O	E° = -0.38V	ΔG°_{cell} = 220.0 kJ/mol
CO₂ + 8H⁺ + 8e⁻ → CH₄ + 2H₂O	E° = -0.24V	ΔG°_{cell} = 185.3 kJ/mol
CO₂ + e⁻ → CO₂^{•-}	E° = -1.90V	ΔG°_{cell} = 183.3 kJ/mol

a list of standard reduction potentials for a variety of CO₂ reduction products, with respect to the Normal Hydrogen Electrode (NHE). A negative reduction potential indicates thermodynamic unfavorability, while a positive reduction potential for a reaction indicates that the reaction is theoretically spontaneous, given the conditions. ΔG° was also calculated, using a rearrangement of the Nernst Equation, ΔG° = -n \mathcal{F} E°, where n = number of electrons and \mathcal{F} = Faraday's constant (96,485 C mol⁻¹) (C = coulomb). The formation of the simple radical species CO₂^{•-} requires nearly the same amount of energy as the formation of methane and formaldehyde, and it requires a significantly more energy than the

formation of formic acid and carbon monoxide. This shows that the multi-electron, proton-coupled reduction of CO₂ will be the most energy-efficient pathway to organic products. Table 1 also shows that the thermodynamic barriers are too steep for the direct reduction of CO₂ to fuel precursors for it to be a viable option in curbing CO₂ accumulation in the atmosphere, even if renewable sources of energy like solar and wind are employed as sources of voltage.¹⁸

In addition to thermodynamic constraints, the rearrangement of the nuclei and chemical bonds of CO₂ to form more complex molecules will prove to be a kinetic obstacle in the pursuit of useful compounds from gaseous CO₂. CO₂ is a linear molecule with a D_{∞h} molecular symmetry. Methane (tetrahedral geometry, T_d), formaldehyde (trigonal, C_{2v}), formic acid (trigonal, C_s), and methanol (trigonal, C_s) all have different geometries from CO₂, and therefore changing orbital hybridization and bonding elements will have kinetic barriers.¹⁹ Activating CO₂, or increasing the internal energy of the molecule, is required prior to its reduction in order to lessen the potential needed to scale the energy barrier. This is known as lowering the overpotential of the molecule. One of the most common methods employed in activating molecules is the use of catalysts, which will be discussed in more detail in section 1.3.

One of the long-term goals of CO₂-reduction research is to find a viable pathway to methanol, since methanol is a very useful feedstock chemical and fuel precursor. Methanol can be converted to gasoline, for example, by using high surface area zeolite catalysts such as ZSM-5.²⁰ The current method of

producing methanol on an industrial scale is the conversion of synthesis gas (CO/H₂) by using a catalytic mixture of copper, zinc oxide, and alumina. Currently, the process requires high temperatures and high pressures, and a more energy-efficient process is desired. Our feedstock CO₂ can be converted into methanol or other useful organic compounds,^{21, 22, 23} but it will require complex molecular manipulations rather than a high-cost direct route.

1.2 Electrochemistry

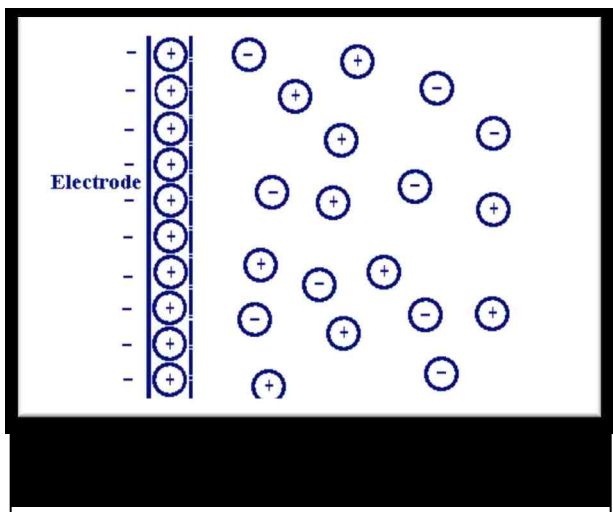
The interaction between electrical and chemical energies and processes is the major topic of study within the field of electrochemistry. The two major sub-fields of study within electrochemistry include the study of the effects of an electrical current on a molecule or chemical reaction, and the study of the production of electricity as a result of chemical reactions. For the purposes of this section, we will focus on the first area and delve into the effects of electrical energy upon chemicals and their associated reactions.

The interaction between two chemical phases is of utmost importance to electrochemists.²⁴ Chemical phases (in the electrochemical sense) need to be defined, as they are different than traditional phases of matter like solid, liquid, and gas. Very commonly, there are two phases in a typical electrochemical cell: the electronic conductor and the ionic conductor. The electronic conductor is most typically the site of a build-up of charge (capacitance), without the

accumulation or movement of ions within the substrate. The capacitance of the electronic conductor increases as applied potential increases until the thermodynamic threshold of the solvated compound is attained, and then charge is distributed throughout the

medium. Electronic conductors are typically homogenous.

Materials commonly used in electronic conductors are platinum, titanium, mercury, and carbon. All electronic conductors are referred



to as electrodes. The second phase within an electrochemical cell is the ionic conductor. Their compositions vary widely, but they are invariably electrolyte solutions (aqueous or non-aqueous) or gels that allow electrons and ions to freely move to form a circuit with another electrode. The interface between these two phases is called the electrical double layer, which is the location of all the redox reactions in the electrochemical cell. Figure 2 displays an electrical double layer as the interface between the two phases.

As the electrode builds charge (negative charge for a reducing potential, and a positive charge for an oxidizing potential) from an external source, ions or polar molecules form a layer, adsorbing onto the electrode. If the electrode has a negative charge, then cations or the positively charged dipole of the polar molecule will adsorb onto the electrode. Next, solvated anions or other

negatively charged species approach the positively charged layer, forming the double layer of ions. The reverse is true for an oxidizing potential. The kinetics of a chemical reaction rely greatly upon the formation and structure of the double layer because it is through the electrical double layer that molecules are reduced or oxidized—meaning, the nature of the double layer allows for electron movement from the electrode to the electrolyte solution and then transferred to the solvated compound to be reduced or oxidized. For most electrochemical cells, the electrical double layer is no more than 100 Å thick.²⁵

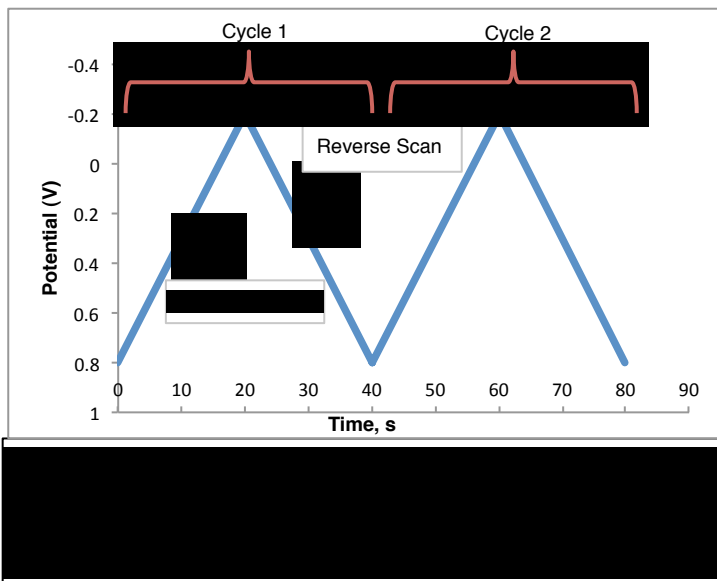
The charge distribution in the double layer behaves predictably, so electrochemistry can be a very valuable tool in determining thermodynamic and kinetic data of an electroactive species. For electrochemistry experiments to work properly, the species in question must be able to accept or donate electrons in order for characteristic data to be obtained. A precise potential supplied by a potentiostat is applied through one electrode, and the potential is measured at the opposing electrode. The difference in potential between the two measures the electroactivity of the complex in question.

Many electrochemistry experiments utilize a three-electrode system to determine standard potentials, namely, the working, counter, and reference electrodes. A working electrode has a definite surface area and is polished regularly to maintain the known surface area—a value that must be known in quantitative experiments in determining reaction rates and diffusion constants. The current passes from the working electrode to a counter electrode, also

known as an auxiliary electrode. By design, the properties of the counter electrode do not affect the behavior of the reactions occurring at the working electrode. The counter electrode has a very high surface area compared to the working electrode coupled with very low impedance, and it carries all the current from the system to complete the circuit. The third electrode, the reference electrode, does not carry any current because it has very high impedance, and it has a very stable and well-known electrode potential. All electrochemical reactions must be referenced to one of these electrodes for comparability to other reactions in the literature—most typically, this electrode is Ag/Ag^+ .

There are many different types of electrochemical experiments that one may employ. In order to determine electroactivity and standard potentials, cyclic voltammetry (CV) is the most powerful and most common tool. In cyclic voltammetry, the voltage of the electrode fluctuates at a steady rate between a

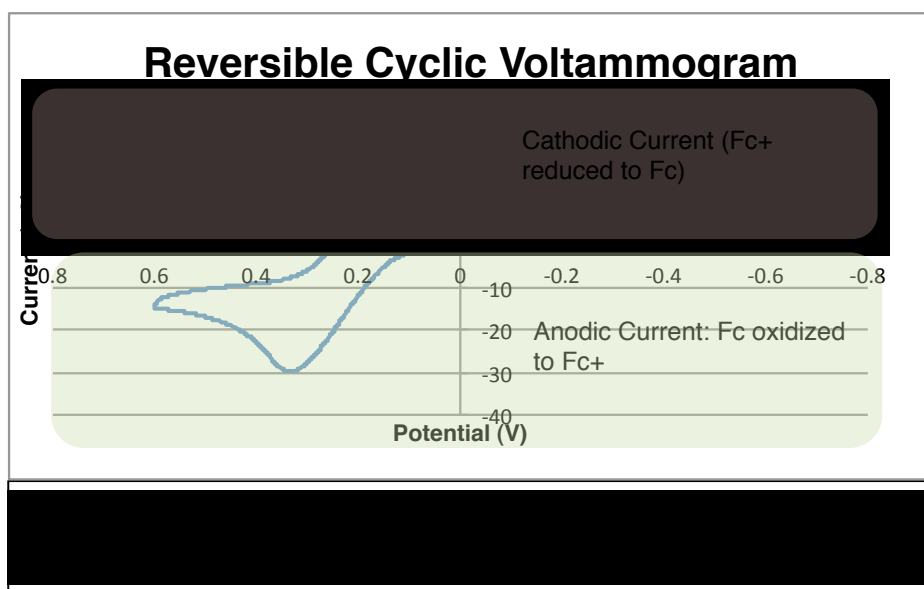
high and a low voltage (see Figure 3), measuring the current as the potential cycle progresses. Increases in current depict a change in the system—most often, a small peak is interpreted by a



conformational change in the system, such as molecular alignment. A sharp

peak typically depicts a change in the oxidation state of a species. This cycle between a high and low potential can repeat itself many times—a useful method in determining chemical and/or electrical reversibility.

Figure 4 depicts a typical cyclic voltammogram of ferrocene (Fc)—the internationally recognized standard for all electrochemistry in non-aqueous solutions.²⁶ The voltammogram begins at -0.6 V—note the sign convention of the horizontal axis utilized by electrochemists—and proceeds in the positive direction, until the ferrocene begins to oxidize slowly, eventually reaching a reduction peak at ~0.34 V. The product formed at the double layer is ferrocenium (Fc⁺). The potential then switches toward negative voltages at 0.6 V, and ferrocenium is reduced back to its original form at approximately 0.1 V. This reaction is completely reversible, and so the cycle could repeat itself thousands of times without any variance in the peak heights or peak separation.

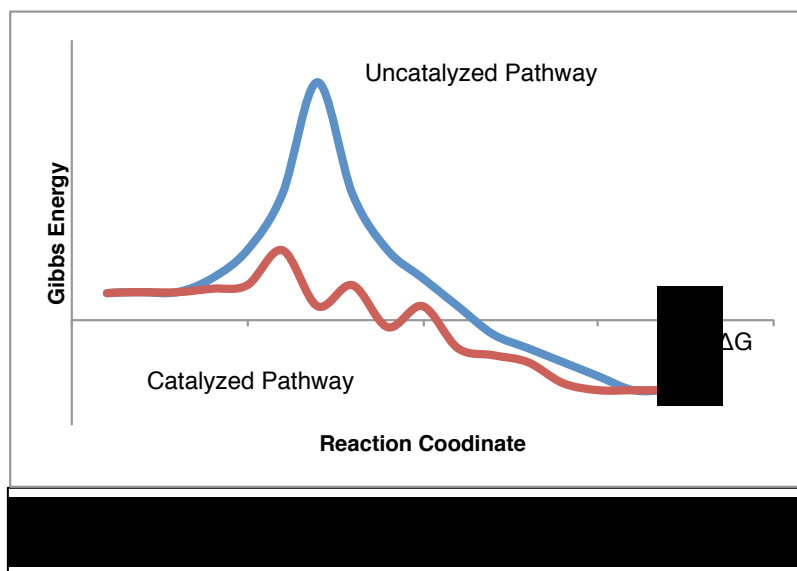


The standard reduction potential, or the intrinsic ability for a species to accept electrons from a voltage source, is a very useful piece of data acquired from cyclic voltammograms. CVs are also used to determine the number of electrons transferred during a redox reaction (it is typical to see a one electron transfer, but two or more electron transfers are not uncommon). Diffusion rates can be determined by a rearrangement of the Cottrell Equation, $D = \frac{i^2}{vn^3(FAC)^2}$, where i = peak reduction current (amps), v = scan rate (Vs^{-1}), n = number of electrons gained during the reduction, A = surface area of the electrode (cm^2), C = initial concentration of the analyte (mol/cm^3), and F = Faraday's constant.

1.3 Electrocatalysis

Although the breadth of electrocatalysis is wide, all electrocatalysts are defined by their ability to shuttle electrons directly into an electroactive species. In a general sense, there are two types of catalysts: heterogeneous and homogeneous. Heterogeneous catalysts exist in a different phase than the medium, *e.g.*, a solid nanoparticle in a liquid solution. Homogeneous catalysts exist within the same phase as the reactants and are codissolved in a solvent (typically liquid, but it can be a gaseous solvent as well). Heterogeneous and homogeneous catalysts both offer advantages relative to the other. Heterogeneous electrocatalysts come in the form of indissoluble, high surface area nanoparticles adsorbed onto a conductive surface or material, and it is

possible for the electrode itself to act as an electrocatalyst. These are typically able to withstand a wide range of reaction conditions, and an extra step is not required to separate the catalyst from the product. Homogeneous electrocatalysts are typically coordination compounds or biomolecules, like enzymes. Homogeneous catalysts are attractive because they exist in the same phase as the reactants, thus limiting diffusion issues to/from the catalyst. As



well, it is much easier to dissipate heat from the solution than it is a solid bed of catalytic material.

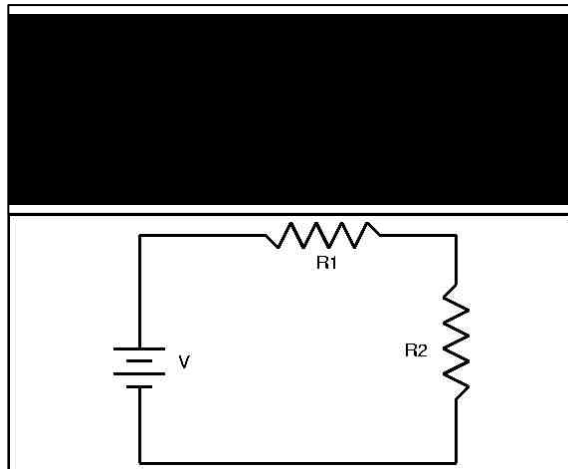
One unique aspect of catalysts in general is their ability

to increase the rate of product formation through the lowering of the Gibbs energy of activation. Figure 5 displays an elementary view of the lowering of energy of activation via catalysis.²⁷ The total Gibbs free energy (ΔG) will not change since G is a state function, but the pathway changes between the catalyzed (red line) and uncatalyzed (blue line) reaction, effectively lowering the activation energy for the catalyzed pathway. Many times during catalysis, rearrangement and oxidation state changes occur, resulting in many intermediates and transition states that are not normally formed during

uncatalyzed reactions. Because of this, care must be taken that none of the intermediates are thermodynamically more stable than the desired product, as this would create undesired stable products. In addition, impurities may coordinate to the active catalyst sites and act as catalyst poisons, so these specific impurities must not be present in the reaction cell.

Although catalysts decrease the activation energy of a reaction pathway, electrocatalysts have additional kinetic barriers not shared among other types of catalysts. Equilibrium levels of energy delivered through a potential difference may be achieved, but significant rates of reaction may not be attained due to overpotentials. Simply put, the overpotential of a given system is the actual experimental potential needed in addition to equilibrium values in order to observe reaction progression and is greater than the thermodynamic potential. The unique chemistry occurring at the interface between the bulk solution/solute and the electrode surface justifies the increased activation energies of analytes due to overpotentials. The total overpotential can be thought of as a sum of smaller parts. For example, energy is required to transfer a molecule from the bulk solution to the electrode interface, a process known as mass transfer. Other factors that contribute to overpotentials include electron transfer from the electrode to the catalyst, chemical reactions occurring before or after the electron transfer, and surface reactions like adsorption, desorption, or decomposition. Another way to envision overpotentials is to think of the electrochemical reaction as a circuit, and each factor contributing to the overpotential (mass transfer,

charge transfer, etc.) can be thought of as resistors (more exactly, impedances) in the circuit. Figure 6 displays a common circuit with two impedances in series to illustrate the concept of overpotentials.



One of the largest impedances to CO₂ reduction is the overpotential associated with the bending of each CO₂ molecule beyond its stable linear conformation.²⁸ Even density functional theory (DFT) calculations are unable to reliably predict overpotentials of CO₂,²⁹ and an understanding of how to lower overpotentials associated with CO₂ reduction is largely unknown.

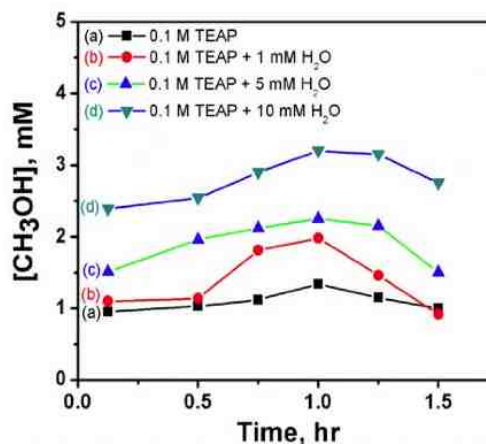
1.4 A Sampling of Electrocatalysis Efforts in CO₂ Reduction

Since research efforts toward effective CO₂ reduction is so important, nearly every class of molecules has been attempted to bind and/or reduce CO₂. An exhaustive review is available to the interested reader,³⁰ yet it remains that high overpotentials and competing H₂ production on the cathode hinder the catalytic activity.

1.4.1 Titanium Oxide

Titania (TiO_2) forms nanoparticles readily and is used in many colloidal suspensions like sunscreen and pigments. TiO_2 nanoparticles are also known to exhibit different behaviors than their bulk counterpart, and even though CO_2 does not naturally adsorb onto bulk rutile (the natural crystalline form of TiO_2), it does adsorb onto TiO_2 nanoparticles. Ramesha *et al.* drop-coated TiO_2 nanoparticles onto a glassy carbon working electrode, and since TiO_2 is conductive this secured CO_2 adsorption onto the electrode.³¹ By using tetraethylammonium perchlorate as a supporting electrolyte in acetonitrile, a one-electron reduction of CO_2 was achieved at -0.95 V vs. NHE. Referencing back to Table 1 will refresh the reader that a one-electron reduction of CO_2 to $\text{CO}_2^{\cdot-}$ is normally -1.90 V vs. NHE. The reduction potential dropped by half, but it is still significantly higher than other, proton-coupled multi-

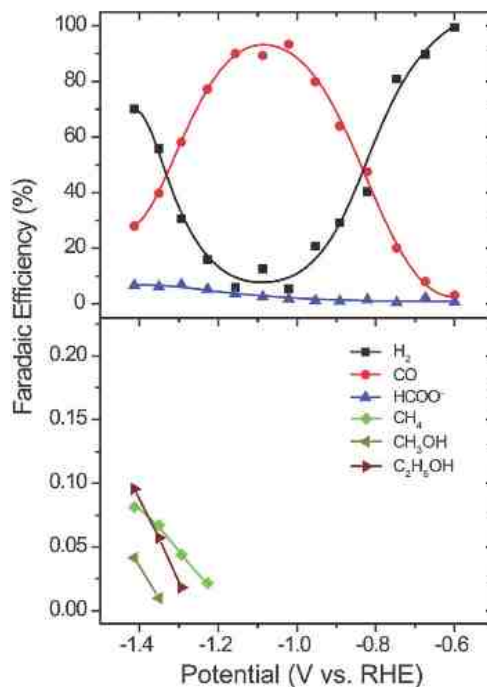
electron reductions. An interesting product conversion from the radical species occurred when the acetonitrile was not completely dry. When traces of water were present in the electrochemical cell, it was found using gas chromatography/mass



spectrometry (GC/MS) that methanol was a major product (see Figure 7). Investigation of other weak acids as proton donors was not explored. The greatest concentration of methanol achieved by the group was ~3 mM from a 10 mM water doping. Methanol production was far from selective, as there were several C₁ products formed during the reduction. Separating the products from each other in the electrolyte solution would also prove to be very challenging if this process were scaled up.

1.4.2 Silver Metal

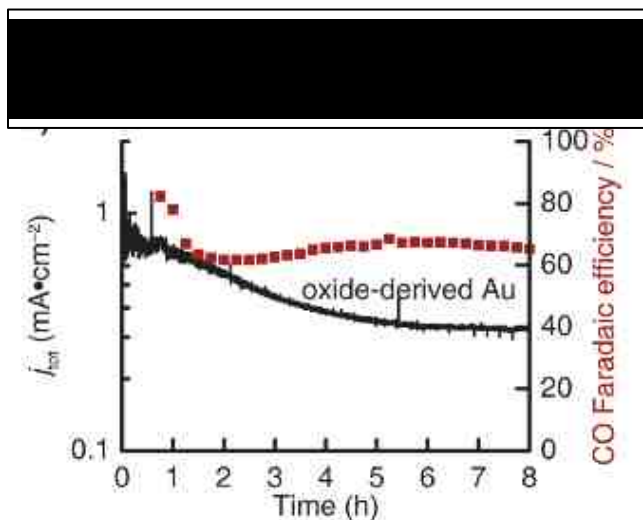
When directly reducing CO₂ on an electrode in a protic environment, there is always a risk of producing hydrogen gas, since gaseous H₂ and CO₂ have similar reduction potentials and H₂ evolution is more facile.³² Silver is known to exhibit low activity for hydrogen reduction and evolution,³³ so Hatsukade *et al.* explored reduction of CO₂ on silver electrodes.³⁴ Most



working electrodes are very small (on the order of 500 mm²), but this research utilized a sheet of silver foil several orders of magnitude larger in surface area than normal working electrodes. This provided a larger area for CO₂ reduction. The electrochemical cell used water as a solvent, with potassium bicarbonate as the supporting electrolyte. CO₂ was added stoichiometrically to the cell, and a gas outlet was connected directly to a gas chromatograph for immediate identification and product formation. Figure 8 displays the faradaic efficiencies of each of the six products formed during electrolysis. Beginning at -1.2 V vs. NHE, methane begins to form. At -1.3 V ethanol forms, and then at -1.35 V methanol begins to form. These are still very large overpotentials that need to eventually be addressed (compare -0.24 V for methane production). Even though silver has a reduced activity toward H₂ production, H₂ was still a major product, exposing just how much energy is really required in the reduction of CO₂ on silver metal. No other electrolyte solutions were used in these studies.

1.4.3 Gold Oxide

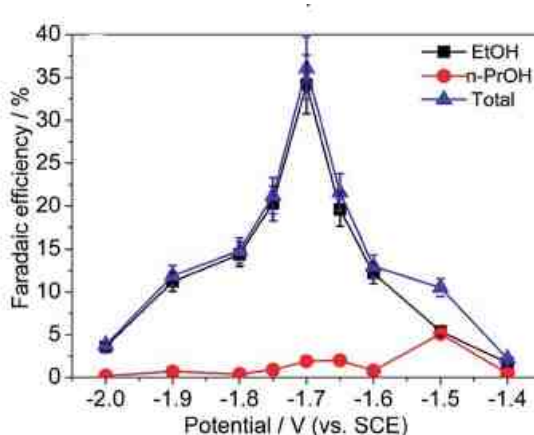
Gold oxide (Au₂O₃) nanoparticles were shown to have high activity toward the reduction of CO₂ to CO.³⁵ By coating a glassy carbon electrode with gold oxide



nanoparticles, experiments were conducted to determine if Au_2O_3 could function as an electrocatalyst for CO_2 reduction. At potentials more negative than -0.5 V vs. NHE, Au_2O_3 catalyzed hydrogen production much more favorably than CO production, but it was found that at -0.25 V, CO_2 readily reduces to CO without the formation of H_2 . Au nanoparticles may not be able to electrocatalytically reduce CO_2 to methanol, but they could be used to create a stepwise catalytic process to form many products from CO.

1.4.4 Copper

CO_2 reduction via CuO nanoparticles has been shown to produce a number of products in different yields; however, high selectivity is required for any meaningful production of C_1 chemicals.³⁶ A unique approach to using Cu^0 in the reduction of CO_2 was recently reported.³⁷ In this article, the authors synthesized specific morphologies of CuO nanoparticles via hydrothermal techniques. The nanoparticles were then loaded onto a glassy carbon electrode and reduced to metallic copper. One morphology (4 μm -diameter spheres) yielded quite



surprising results, as can be seen in Figure 10. Unexpectedly, ethanol was the major product formed in the reaction. Methanol was formed as well, but it only appeared in trace amounts. It was also surprising to see that n-propanol (n-PrOH) (a three-carbon chain) formed during this reduction. The reduction occurred in an aqueous environment with potassium iodide (KI) used as the supporting electrolyte. No explanation was given as to the mechanism of the reductions, nor was there any discussion on why ethanol formed more readily than methanol. Also, the potentials used are quite high, as -1.7 V vs. SCE (saturated calomel electrode) converts to -1.94 V vs. NHE, as the SCE is 0.241 V more positive than NHE.

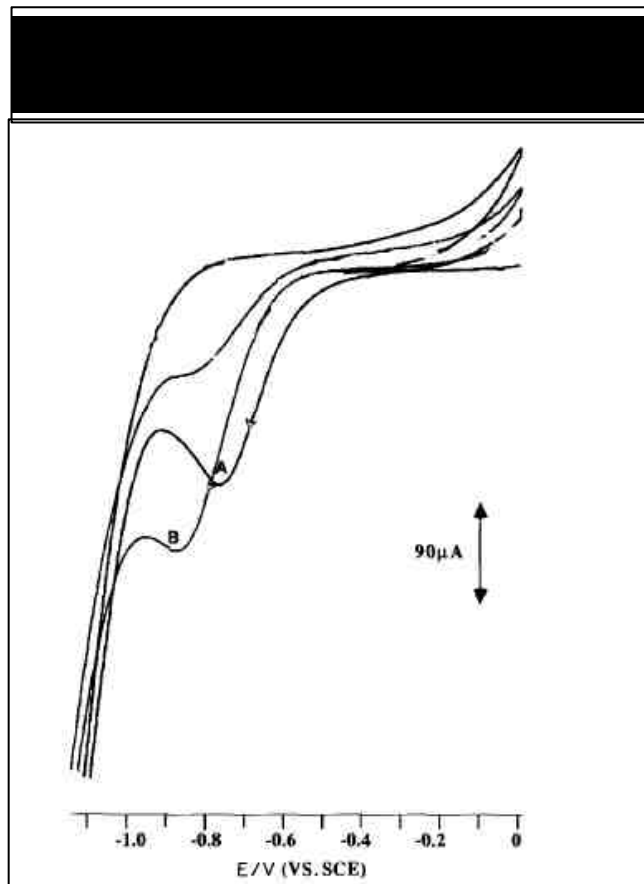
1.4.5 Homogeneous Catalytic Reduction of CO₂

All the above catalysts are representative of the active current research in heterogeneous catalysts. Far less common is the use of homogeneous catalysts, but they too can be very effective in reducing CO₂. One of the most promising homogenous electrocatalysts is the pyridinium ion. First used in 1993 to effectively catalyze CO₂ reduction to methanol while also poisoning the catalysis for H₂ production,³⁸ the pyridinium ion proves to show promise in homogenous catalysis in forming C₁ products from CO₂ feedstocks.

Seshadri *et al.* utilized a 0.5 M NaClO₄, 0.01 M pyridine aqueous solution, fixed at pH 5.4 by addition of dilute H₂SO₄. The working electrode was

palladium, but no data were reported on the efficacy of other, more common electrode materials like glassy carbon or platinum. Figure 11 displays the reduction curves for the electrolyte solution under an argon and CO₂ atmosphere.

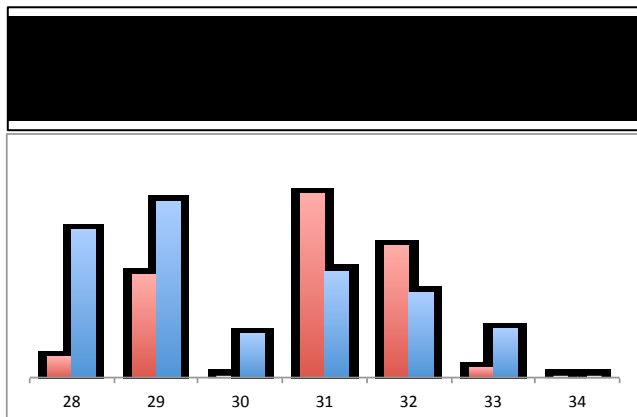
Curve A clearly shows the non-reversible reduction of pyridine, but curve B shows an increase in activity due to the presence of CO₂. In order to determine the products formed during the electroactivity, Seshadri subjected the headspace of the electrochemical cell to GC/MS analysis. Figure 12 displays the results of this experiment. Figure 12(A) displays the theoretical



distribution of mass/charge (m/z) for pure methanol, so it can easily be concluded that there is at least one other component in the headspace of the electrochemical cell. Although not pure, the aqueous solution was shown to contain 0.5 mM methanol after 12 hours of electrolysis held constant at -0.75 V, but there was no investigation as to the concentrations of other compounds in the solution. The approach of enhancing the electroactivity of the CO₂ molecules while also poisoning the H₂ route is a difficult balance, but it will need to be

optimized in order to develop a system for CO₂ reduction using the pyridinium ion.

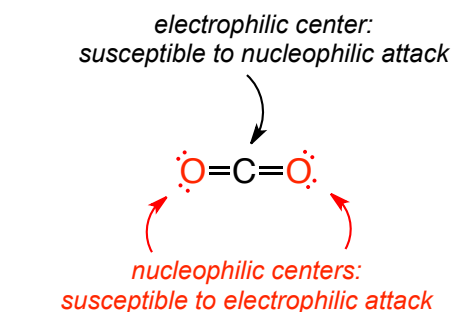
While utilizing nanoparticles on an electrode surface or using the conductive surface to catalyze a CO₂ reduction has shown some promise, there really has not been a clear and universal



electrocatalyst for the reduction of CO₂. Most homogeneous electrocatalysts are not probed because their intermediates are fleeting or are present only during an electrolytic environment. Rather than form clear, covalent bonds with CO₂, we propose using adduct-mediated CO₂ complexes to enable CO₂ reduction through homogenous catalysis.

1.5 Forming a CO₂ Adduct

One of the unique properties of CO₂ is that it is an amphoteric molecule, meaning that it can act as a Lewis base (electron donor) or a Lewis acid (electron acceptor) even though the molecule overall is nonpolar. As shown in Figure



13, the lone pairs on the terminal oxygen atoms are nucleophilic in nature, and the carbon atom is electrophilic in nature due to the electronegativity difference between oxygen and carbon. Thus, even though CO_2 is often thought of “energetically spent” or a thermodynamic sink, it can be used as a reactant under special conditions.

Prior to this research, our group developed tin and zinc complexes that form CO_2 adducts, rather than the traditional insertion of CO_2 into a polarized M-X bond.³⁹ Much of this work focused on the multidentate bis(diphosphinoamine) $(\text{R}_2\text{P})_2\text{NH}$ (R = alkyl, aryl), or PNP ligand. Denticity is a term that refers to the number of groups donating electrons to a coordination complex from one ligand (mono-, bi-, tri-, etc.), and multidentate ligands can donate a variety of groups to a coordination complex depending on the environment. The multidenticity of these PNP ligands are determined by the presence of the central metal atom, and several divalent metals were used, including Sn^{2+} , Zn^{2+} , Mg^{2+} , and Ca^{2+} .

The PNP ligand has both a hard bonding mode (through the N atom) and a soft bonding mode (through the

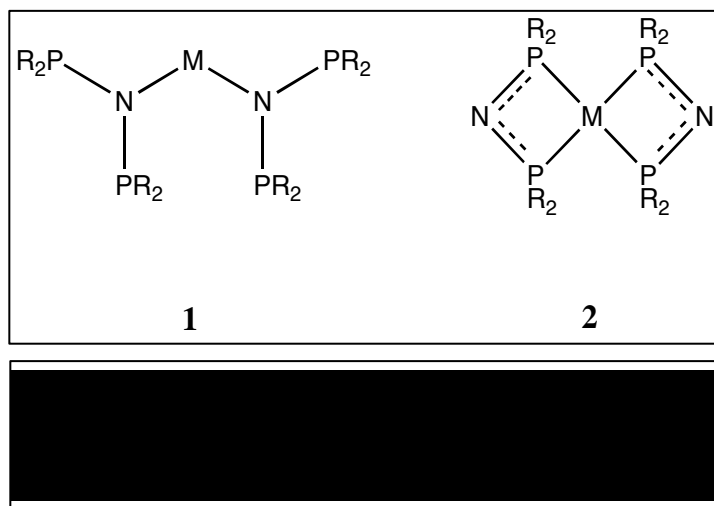
P atoms). In Hard/Soft Acid/Base Theory (HSAB), a

hard acid or base is a

species that is small

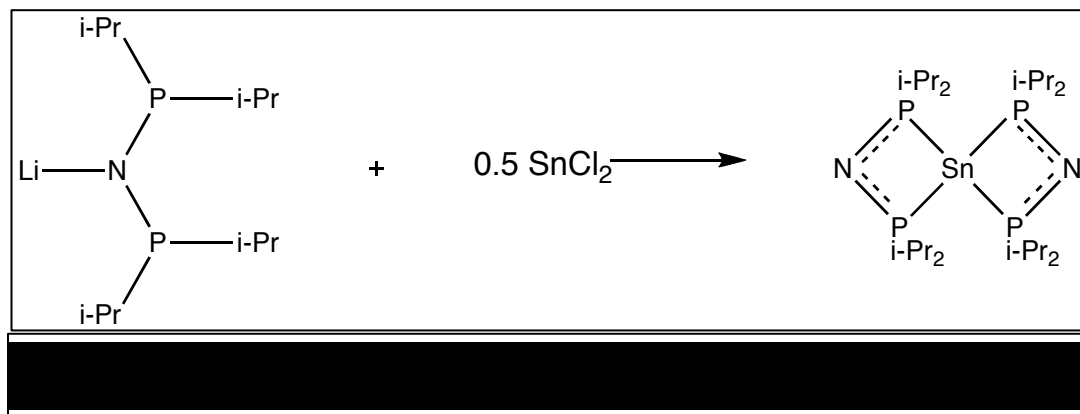
(typically a high charge for

acids) and is weakly



polarizable. The exact opposite is true of a soft acid or base—they are typically large and easily polarizable.⁴⁰ Hard acids prefer binding with hard bases and vice versa. Depending on the hard/soft attributes of the divalent metal, the PNP ligand would bind differently to it. Figure 14 displays these two bonding modes.

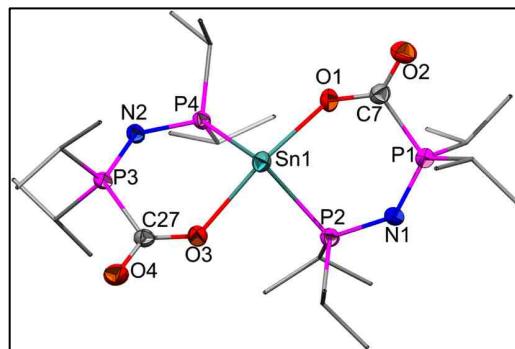
The synthetic pathway to these products was fortunately relatively simple. For example, in the synthesis of $\text{Sn}[\text{N}(\text{Pi-Pr}_2)_2]_2$, lithiated PNP ligand was combined with 0.5 molar equivalent of SnCl_2 in tetrahydrofuran (THF) (see Scheme 1). After isolation via filtration and crystallization techniques, the compound was shown to exhibit bonding mode 2, as verified by single crystal X-ray diffraction. The negative charge from the PNP ligand was distributed evenly along the P-N-P backbone, reminiscent of a π -allyl anion. After bubbling CO_2 at room temperature in pentane for 10 minutes, the CO_2 complex in Figure 15 formed readily. Typical CO_2 insertions into polar M-element bonds yield products that exhibit a C-O single bond ($\sim 1.4 \text{ \AA}$) and a C=O double bond ($\sim 1.2 \text{ \AA}$), while this particular Sn complex exhibits near-equivalent distances for both C-O bonds. Other indicators that show this product is not a traditional insertion product is the reversibility of association and dissociation of the bound CO_2 (heating the product



gently loses 12% by weight, indicative of the loss of two equivalents of CO₂), and the complex exhibits a long-term stability under a carbon dioxide atmosphere. As well, adding labeled ¹³CO₂ to the complex results in rapid incorporation of the labeled CO₂. The most important quality of the Sn complex in Figure 15 is the extreme bending of the CO₂ molecule from its original linear geometry to ~130°. Since bending the CO₂ molecule prior to reduction should drastically reduce the overpotential of reducing it electrochemically, it was thought that this pre-bent CO₂ molecule could lead to significant advances in the reduction of CO₂ to other C₁ molecules.

In order to test this hypothesis, the Sn complex needed to be subject to an electrochemically reductive environment to determine its usefulness as an effective electrocatalyst toward CO₂ reduction. Without an in-house electrochemist available, samples were sent to collaborators at the University of Vermont for testing (Prof. W.E.

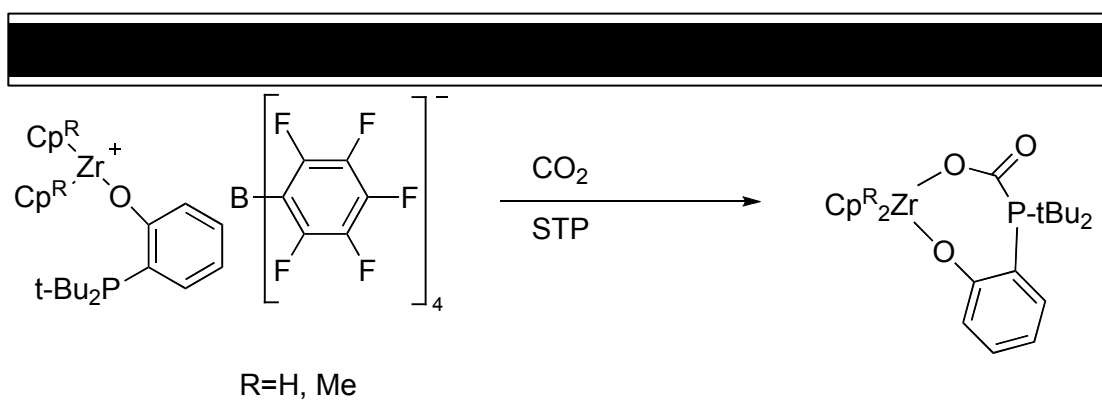
Geiger). After extensive experimentation, it was found that these compounds were unfortunately unstable to a persistent voltage and were unable to reduce the CO₂ molecule before the metal-ligand architecture began to degrade and decompose. It was felt that the PNP-metal complex was too fragile to survive the electrochemical cell setup.



It became quite clear to us that new complexes needed to be synthesized to reach the long-term goal of CO₂ reduction to useful organic products or fuel precursors. One requirement for an effective electrocatalyst is the ability to shuttle electrons to the target molecule unhindered, and it was evident that the (PNP)₂Sn structure could not manage electron shuttling to the attached CO₂ without decomposition. The multidentate motif gave very promising results as to bending the CO₂ molecule, and so research was conducted to find other viable ligand systems that could pre-bend CO₂ while also remaining capable of shuttling electrons to the attached CO₂.

At the outset of this new direction, it was shown by Chapman *et al.* that a sampling of cationic zirconocene species also activated CO₂.⁴¹ In fact, the reactivity of said species was due in part to a unique OCCP bidentate ligand, and also in part to a growing field of chemistry involving “frustrated Lewis pairs” (FLP), first reported by Stephan.⁴² FLPs are Lewis acid and base pairs that cannot interact directly due to steric hindrances. Because of these “frustrations”, FLP molecules are very reactive and have been shown to react with small, inert molecules.^{43,44,45,46,47} The afore-mentioned research of Chapman *et al.* concerning FLP-zirconocene complexes reactivity towards CO₂ showed a reversible insertion of CO₂ as shown in Scheme 2. Although the O-C-O bonds of the CO₂ insertion are inequivalent in this example, the type of amphoteric insertion is very similar to the adduct-mediated Sn complex prepared above in our group. The scope of Chapman’s research was to determine reactivity of

these FLP compounds toward small molecules, and there was no interest in converting them to other products. The intention of this research is to further develop the ideas brought upon by our long-term research goals with that of Chapman's research by expanding the bidentate ligands and Group 4 metals to determine if adduct-like insertion can be achieved, while also subjecting these complexes to a reductive potential to form other C₁ products.



Chapter 2: Group 4 Transition Metal Complexation and Electrochemical Investigations

2.1 Ligand Preparations and Synthesis

In metal coordination chemistry, a “complex” indicates a central metal atom with attached ligands to form a species that can exist in a variety of geometries. Ligands are independently charged or neutral species and serve as electron donors (Lewis bases) in coordination complexes, while the metal center acts as the electron acceptor (Lewis acid). Coordination complexes, like ligands, can be neutral, *e.g.*, $\text{Ni}(\text{CO})_4$, or charged such as $[\text{Co}(\text{NH}_3)_6]^{3+}$ or $[\text{Fe}(\text{CN})_6]^{3-}$. All metals across the periodic table can form complexes, and these complexes, virtually innumerable due to the vast amount of ligand possibilities, can be utilized in designing efficient catalysts.⁴⁸

Changing the ligand structure around a metal core largely has a combination of two effects, namely electronic and steric. Electronic effects change depending on the electronegativity differences between the metal center and the ligands themselves. For example, highly electronegative ligands such as halogens and nitriles transfer electron density through σ bonds from the metal center to the ligand via electronic induction, forming a permanent dipole. These ligands are known as electron withdrawing ligands. Polarizable bonds like those found in methyl groups and carbonyls donate electron density to the metal

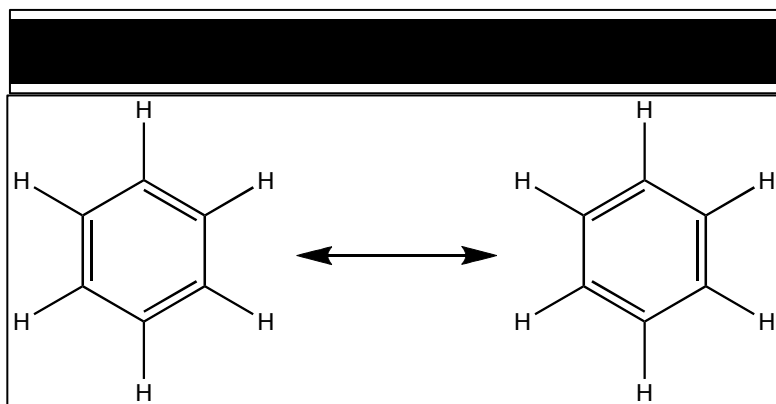
center, allowing for greater positive charges on the metal center to be stable.

These ligands are known as electron donating ligands.

The size of the ligands attached to the metal also plays a significant role in determining the reaction chemistry of the complex. Small ligands can often lead to dimerization or condensation of the metal complexes to form multi-metallic species, thus affecting the resulting structures. Steric hindrance effects can often occur with large or bulky ligands. Since each atom occupies a given space, ligand structures that impede each other will change their conformation due to electron cloud repulsion. These changes in conformation can then have a drastic effect on reactivity.⁴⁹ Most often, chemists utilize both steric and electronic properties of ligands to design metal complexes in order to catalyze specific chemical reactions.

2.1.1 Aromatic Structural Foundation for Ligand Synthesis

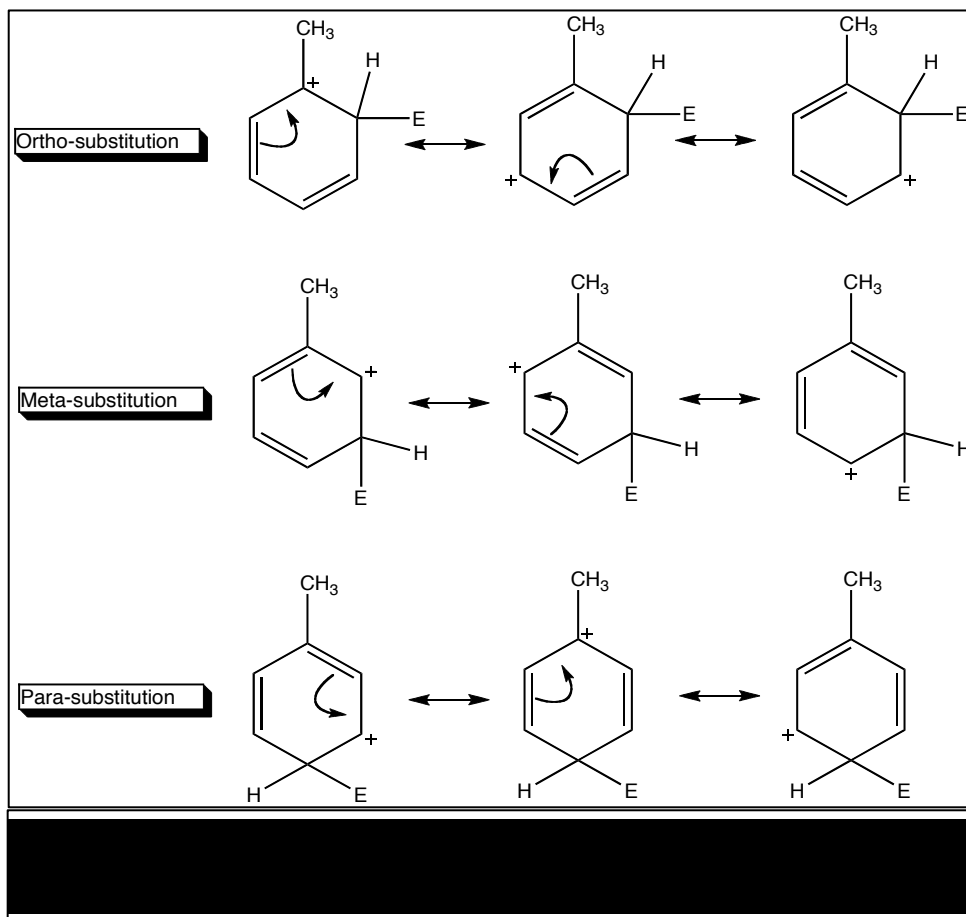
Benzene (C_6H_6) is an especially stable compound (see Figure 16 for structure), due to its aromaticity.⁵⁰ The energy levels of the overlapping p orbitals



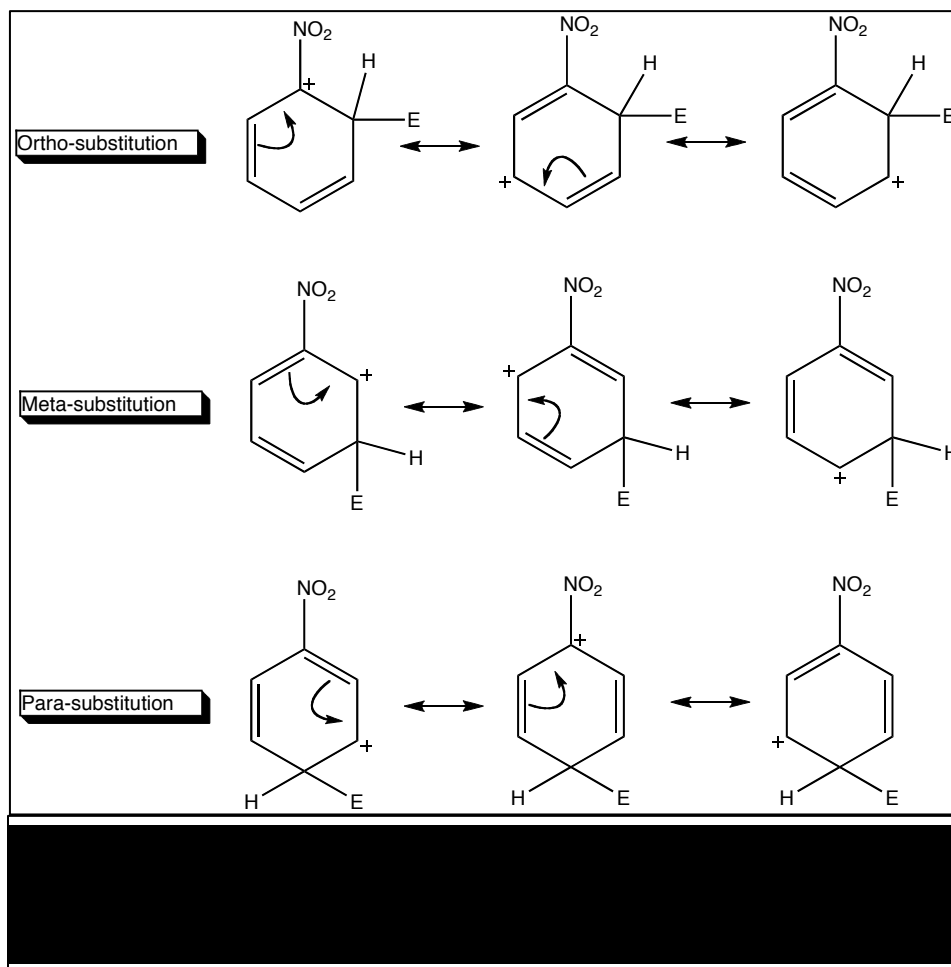
of the carbon atoms can be adjusted by adding constituents to the ring, making the system either more or less

reactive. For example, a monosubstituted benzene ring when treated with an electrophile will undergo an aromatic substitution reaction. However, the electronic effects from the substituent onto the benzene ring can affect the outcome of the final disubstituted product. Toluene and nitrobenzene can serve as two illustrative examples.

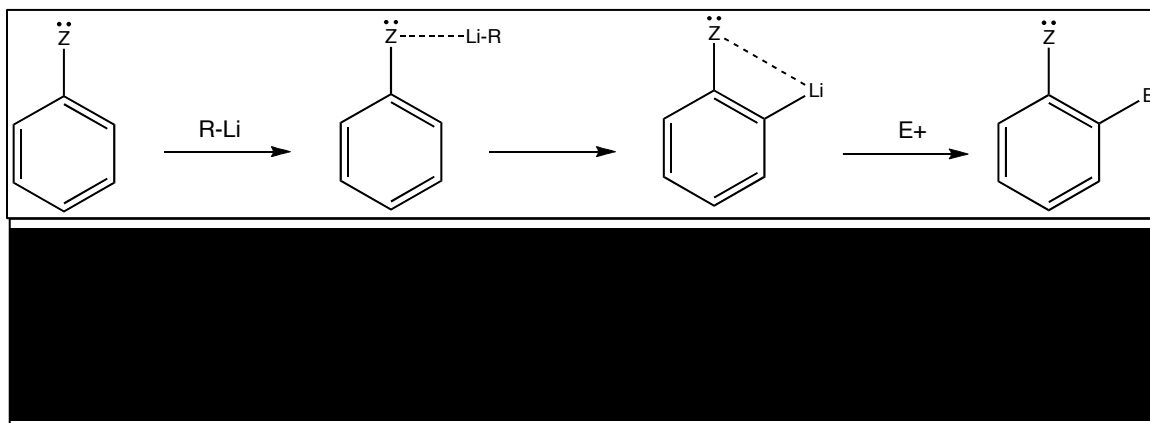
Toluene (C_7H_8), due to its electron-donating methyl group, undergoes aromatic substitution reactions faster than benzene. The methyl group activates the ring by stabilizing the carbocation intermediate. The methyl group, similarly to any other monosubstituted electron-donating group, also effectively directs the electrophile to substitute at the *ortho* or *para* positions. Figure 17 illustrates this example. The carbocation formed within the ring is stabilized by the partial



negative charge donated by the methyl group, as is illustrated via the resonance effect. However, nitrobenzene ($C_6H_5NO_2$) contains an electron-withdrawing nitrate group, and therefore the electrophilic attack in aromatic substitution reactions behaves differently. Figure 18 displays the resonance effect on the carbocation intermediate for nitrobenzene. Instead of a stabilizing effect on a particular orientation, the *ortho* and *para* substitutions are destabilized due to the partial positive charge on the nitrogen atom adjacent to the carbocation in the ring.

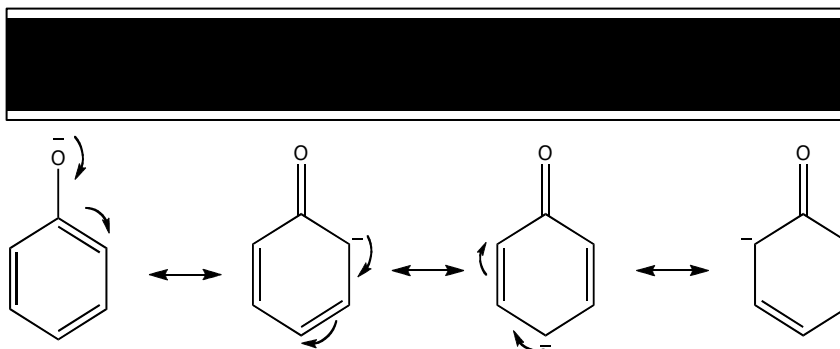


Monosubstituted, heteroatom-bound ligands such as phenol and thiophenol donate electron density to the ring, allowing for fast *ortho/para* directing of aromatic substitution reactions. Cleanly separating *ortho* and *para* disubstituted products can be a challenge in workup, but when using lithiating agents like *n*-butyllithium, the *ortho/para* directing group is changed to specifically foster *ortho* lithiation by means of an aryl-lithium intermediate (see Figure 19)⁵¹ in a process called directed *ortho* metalation. This is the preferred method of substituting an electrophile selectively into the *ortho* position on the monosubstituted benzene.



Phenol and thiophenol are the foundational structures that were manipulated with *o*-disubstituted phosphines for this research, utilizing alkyllithium reagents to foster *ortho* substitution. Aryl phenols and thiophenols are generally more acidic than their non-aryl alcohol and thiol counterparts due to the resonance effect from the phenyl ring, thus stabilizing the conjugate base of each (See Figure 20). Thiophenol is approximately 10,000 times more acidic than phenol ($pK_a = 6$ vs. 10) because sulfur is a third period element, and

therefore it has access to larger, higher-energy frontier orbitals than oxygen. These high-energy valence shells form weaker and thus longer σ bonds to hydrogen than oxygen can. Even though oxygen is more electronegative than



sulfur (thus creating a stronger dipole with hydrogen), the weakening of the S-H bond due to larger atomic radius of sulfur makes thiophenol more acidic than phenol.⁵²

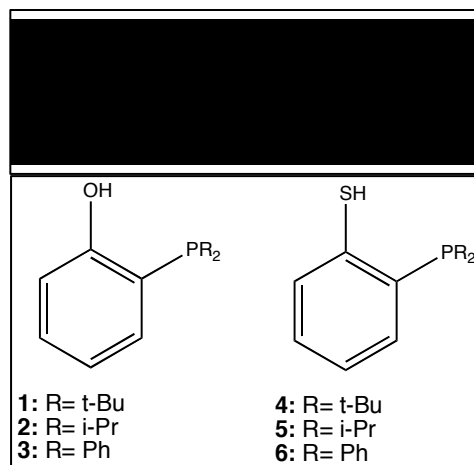
As substituents are added to the *ortho* position, the electronics and sterics of the aryl ligand change. Three di-substituted phosphines were utilized in this research, *i.e.*, diphenylphosphide ($-PPh_2$; smallest sterics, less electron donating), diisopropylphosphide ($-Pi-Pr_2$; large sterics, average electron donating), di-*tert*-butylphosphide ($-Pt-Bu_2$; largest sterics, more electron donating).⁵³ The sterics of each phosphine directly affect the acidity of the thiophenol or phenol, since large, bulky ligands might shift the oxygen or sulfur atom out of plane with the benzene ring due to electron cloud repulsion. As the acidic heteroatom moves out of plane, the resonance offered inductively from the benzene ring would be diminished, thus decreasing the stability of the conjugate base and forcing the O or S atom to become less acidic. *Ortho* effects are never so simple,⁵⁴ and near-field hydrogen atoms within close proximity to the

conjugate base can also stabilize it. A quantitative study has not been performed with respect to these six ligands' acidities, but electronic and steric trends will be able to be determined through ^{31}P NMR spectroscopy.

2.1.2 Development of OCCP/SCCP Bidentate Ligand Structures

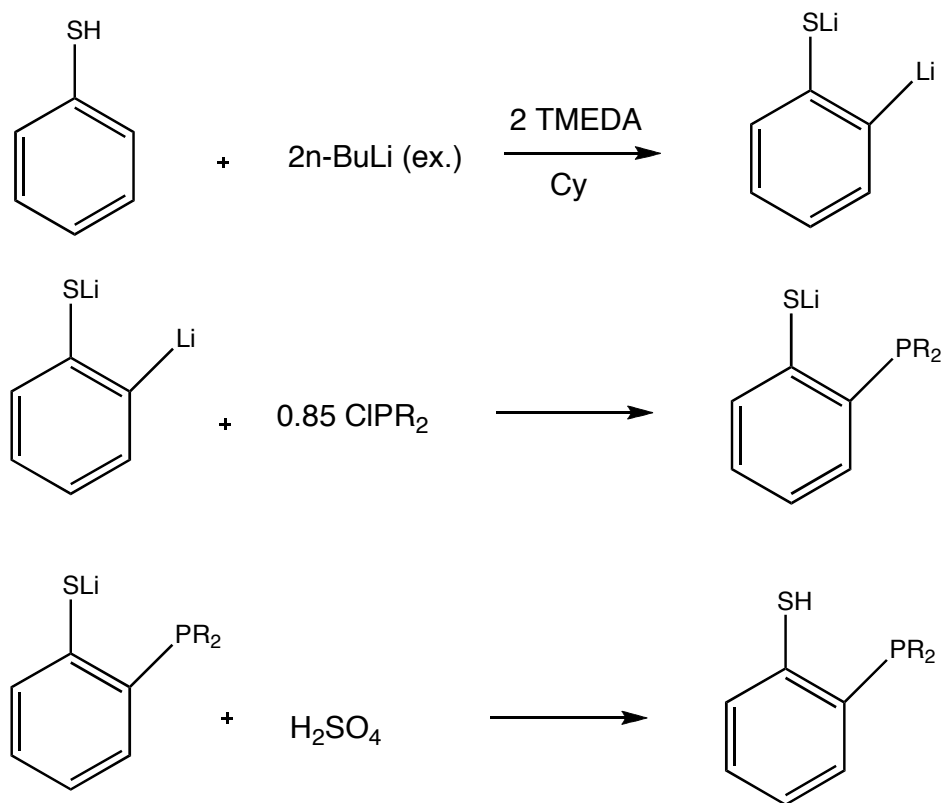
The ligand, *o*-di-*tert*-butylphosphinophenol, is unique in that it can bond covalently to a metal through the O atom and datively via the P atom. The current procedure for synthesizing this ligand is both lengthy and very inefficient (68% yield, and only <1.0 g can be made in a single batch).⁵⁵ The reason for the inefficiency is the very last step of the synthesis, which required the use of a Kugelrohr oven. A Kugelrohr oven is utilized in short-path vacuum distillations of small amounts of compound that have very high boiling points. As our research group did not have access to a Kugelrohr oven, it became extremely important to synthesize this ligand using a different pathway.

An analogous ligand, diphenylphosphinothiophenol (**6**), is well known,⁵⁶ and its synthetic pathway was used for ligands **4** and **5**. Although lengthy, they did not require the use of a Kugelrohr oven. A list of target molecules was formulated, and Figure 21 displays the target molecules to be



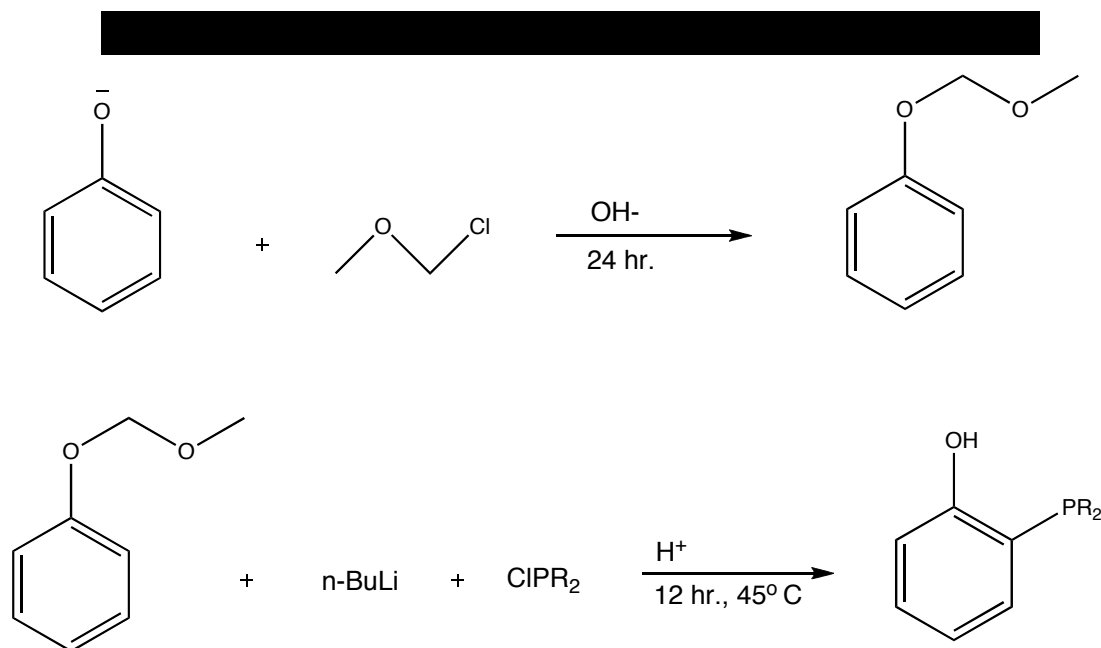
used as ligands in metal complexes for the eventual purpose of bending CO₂.

Adapting the synthesis of **6** to **4** and **5** proved to be very successful, as both were isolated in high yields and purity. **5** had been synthesized before,⁵⁷ but its use in coordination chemistry has been limited to one study for Ir complexes and to our knowledge has never been used in Group 4 chemistry. Ligand **4** had not been reported in the literature previous to this research, and so consequently all metal coordination complexes with **4** are unexplored. Unfortunately, all crystallization attempts for **4** in order to obtain X-ray quality crystals have been unsuccessful thus far. As detailed in Scheme 3, the syntheses of **4-6** begin with a double lithiation of thiophenol. The thiol proton is

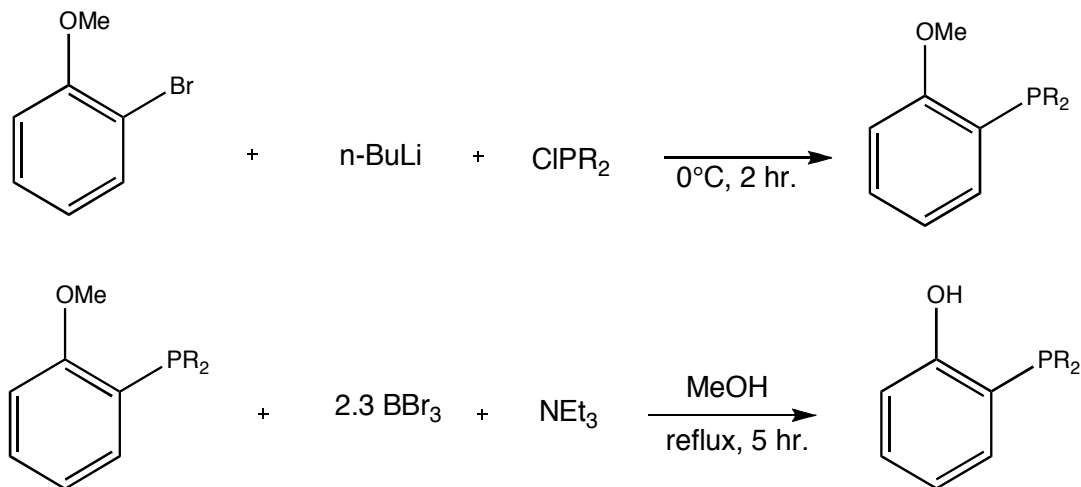


much more acidic than the *ortho* proton, and so both must be lithiated in order to facilitate the desired *ortho* substitution. Then, 85 mol% of the disubstituted chlorophosphine is added very slowly to the di-lithio intermediate. The original preparation calls for 75 mol%, but through careful optimization, we have found that 85 mol% augments the total yield without sacrificing purity. The final step is a careful addition of cold sulfuric acid until the pH reaches 6.5-7.0. This last step is delicate due to the fact that the lithium thiol is very air sensitive, and so pH must be tested sparingly under a positive argon flow.

The oxygenated ligands **1-2** proved to be more difficult to synthesize than their thiophenol counterparts. Fortunately, **3** is commercially available and as such required no synthetic effort. In order to avoid a Kugelrohr distillation, the reaction pathway in Scheme 3 was employed, with phenol being used rather than thiophenol. This method produced an impure mixture containing **1** in 85%



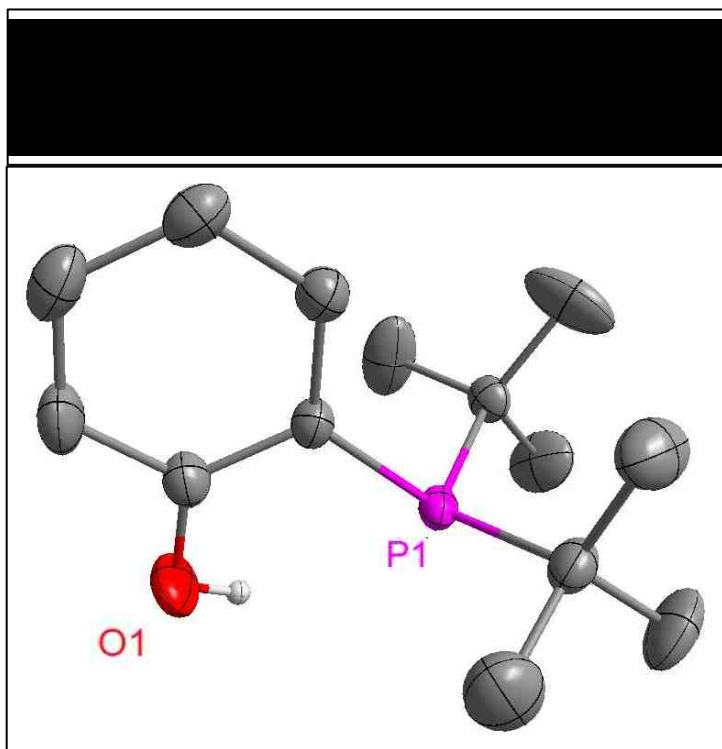
conversion of phenol but with a poor purity of ~50%. In a second synthetic pathway, a protecting group for the alcohol was attempted. Methoxymethyl ether (MOM) was a prime candidate for alcohol protection.⁵⁸ Scheme 4 shows the proposed pathway for using MOM/phenol to insert a disubstituted phosphine at the *ortho* position. First, phenol is to be reduced to phenolate by sodium metal and then reacted with chloromethyl methyl ether (prepared separately) to produce the protected phenol. Then, by reacting the protected ring with *n*-butyllithium to lithiate the *ortho* position and exchanging the lithium with a disubstituted phosphine, it was anticipated that the ligands **1-2** could be isolated and characterized. Unfortunately, the crude product revealed dozens of singlet peaks in the ³¹P NMR, and even after careful and meticulous fractional distillation and column separation, the product could not be isolated and removed from the crude mixture.



The next attempt was to utilize Bornand's original synthetic pathway and adapt it to again avoid using a Kugelrohr oven. Scheme 5 displays this reaction pathway.

2-Bromoanisole was first lithiated in a halogen/lithium exchange and then treated with the cold addition of a disubstituted chlorophosphine to form the *ortho*-substituted diphosphinoanisole. In a second step, boron tribromide was added dropwise to remove the methyl group from the oxygen atom, and finally, triethylamine and methanol were added to remove triethylammonium bromide and protonate the phenolate oxygen atom. In the original preparation, this sludgy final product would be distilled using the Kugelrohr oven. In our adapted pathway, in order to increase the yield dramatically the crude product was

dissolved in benzene and filtered through Celite[®] filter aid. Although this filtration step was very slow due to the viscosity of the crude mixture, this proved to be an invaluable step in increasing the yield of the products. The benzene was then removed *in vacuo*



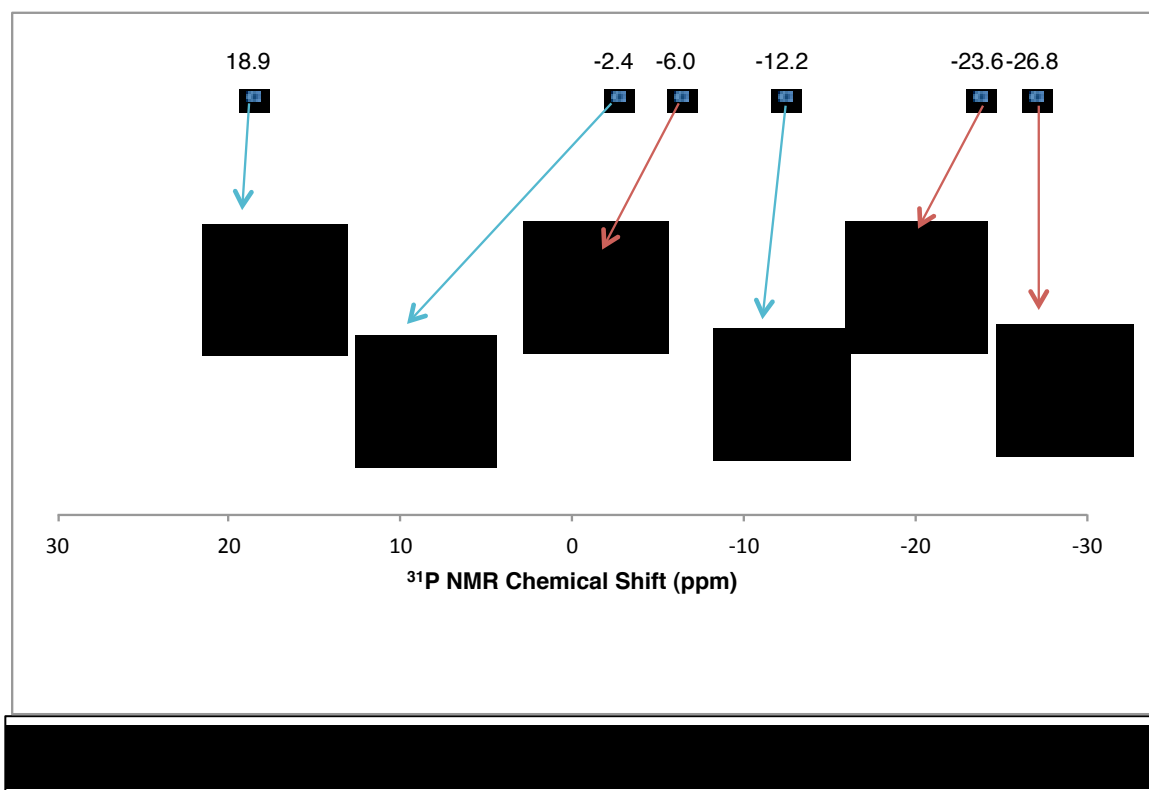
from the reaction flask, and the remaining crude product was distilled through a

simple short-arm distillation apparatus, while maintaining 85°C in the cold arm. The hot water circulation in the cold arm is key in this synthesis because the final products crystallize near room temperature. This method gives a very high purity, and we were able to collect large amounts of product, upwards of 15 g with an 83% yield, as opposed to the previous method, which gave < 1 g with a 68% yield. This method can be employed for both phenol-based ligands needed for this research, **1-2**. **1** crystallized at room temperature, and the single crystal X-ray structure is shown in Figure 22. The structure has no extraordinary features, and there are no special bond lengths or bond angles. There is no unusual geometry and the compound is as expected. Attempts to crystallize **2** have been thus far unsuccessful.

2.1.3 Ligand Trends Through ³¹P NMR Spectroscopy

By comparing the ³¹P NMR chemical shifts of each of the six ligands, one may be able to identify a trend in the electronic behavior of the ligand by extrapolating the information garnered from the electronic environment surrounding the phosphorus atom.⁵⁹ There are many factors that can affect the chemical shifts in ³¹P NMR spectroscopy, including degree of σ -bonding of the P atom (correlated to bond angle), degree of π -bonding of the substituents (known as shielding cones), and electronegativity of substituents (electron density centered at the P atom). Figure 23 displays the ³¹P NMR chemical shifts of each

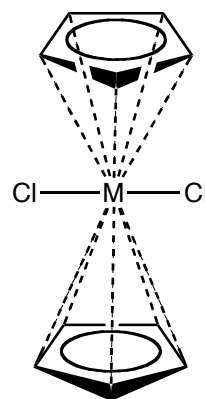
of the six ligands, **1-6**. In NMR spectroscopy terminology, “downfield” and “upfield” are relative terms—downfield refers to a chemical shift more positive than a referenced peak, while upfield refers to chemical shifts more negative. Nuclei that have chemical shifts more downfield have more deshielded environments, caused by the loss of electron density around the nucleus in question. The opposite is true as well - shielded nuclei are those with a greater abundance of electron density around the nucleus, and thus are observed upfield. Typically, in ^1H NMR spectroscopy, aromatic protons are found downfield while alkyl protons are found more upfield. Chemical shifts in phosphorus behave very differently.⁶⁰ Phosphorus atoms attached to alkyl carbons are seen downfield of aryl carbon-attached phosphorus atoms. This is because phosphines are less electronegative than carbon, and so a larger *s* character C-P bond would appear more downfield than a lower *s*-character C-P bond.



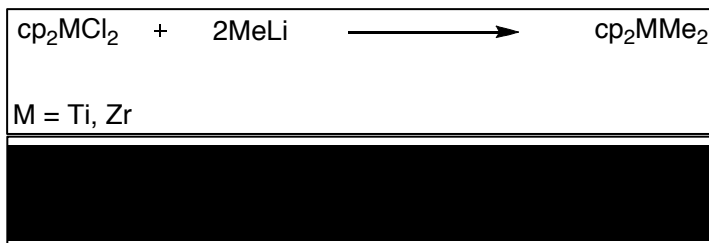
The blue arrows in Figure 23 represent the ^{31}P NMR chemical shifts for the thiophenol ligands **4-6**, whereas the red arrows point to the phenol ligands, **1-3**. The trend holds for both sets of ligands that $-\text{PPh}_2 < -\text{P}i\text{-Pr}_2 < -\text{P}t\text{-Bu}_2$. The difference between the largest and smallest chemical shifts are δ 31.1 ppm for the thiophenols and δ 20.8 ppm for the phenols, indicating that the larger sulfur atomic radii affects the phosphorus electronic environment more than do the smaller oxygen radii. After the ligands were isolated and characterized, they were utilized in a series of metal complexations in order to determine their efficacy in pre-bending an adduct-mediated CO_2 molecule in order to shuttle electrons to CO_2 in an electrochemical system.

2.2 Preparation of the Metal Complex

Group 4 metallocenes are commercially available in their dichlorinated forms (see Figure 24). Ligands **1-6** (see Figure 21, pg. 34) are protic enough to enable reaction of the metallocene and attach through the O or S atoms. However, Cp_2MCl_2 species have two similar sites for proton reactivity – cleaving the M-C bond(s) or cleaving the M-Cl bond(s).

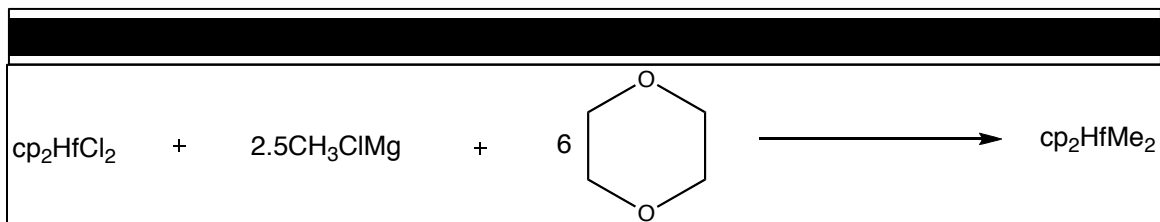


If these protic ligands were used with the dichlorometallocenes, HCl could theoretically form, which is more acidic than any of the six ligands to be added. This would result in a protonation of the original ligand, and effectively no net reaction would occur. Therefore, these ligands are unsuitable to react with the dichlorinated reactants to substitute for the chlorides, and so an alternative route



would have to be employed to facilitate ligand attachment to the metallocenes.

Organolithium reagents are commonly used to remove halogens from compounds and allow substitution with alkyl groups. In our case, methyllithium was used to substitute the chlorine atoms with methyl groups. Scheme 6 illustrates the preparation of dimethyltitanocene and dimethylzirconocene. As the Group 4 metals become larger, they become softer Lewis acids. Lithium is very



small and therefore is a hard acid, so a different approach was required to substitute chlorine atoms with methyl groups on hafnocene, as several attempts to lithiate dichlorohafnocene with methyllithium proved to be unsuccessful. A magnesium Grignard reagent was utilized in this effort because magnesium is softer than lithium. Scheme 7 illustrates this method, utilizing the coordinating ligand dioxane in this Grignard reaction, to facilitate methyl substitution. Each of the Group 4 dimethyl-metals--titanocene,⁶¹ zirconocene,⁶² and hafnocene⁶³— were prepared using previously reported methods.

Once all three dimethylmetallocenes were isolated and purified, each was reacted with ligands **1-6** in a 1:1 ratio at room temperature. These monosubstitution reactions generally proceeded with good yields, and since methane is the leaving group the gas escaped the reaction flask and further purification was typically unnecessary (unless noted below). Scheme 8 illustrates the general reaction for these syntheses.

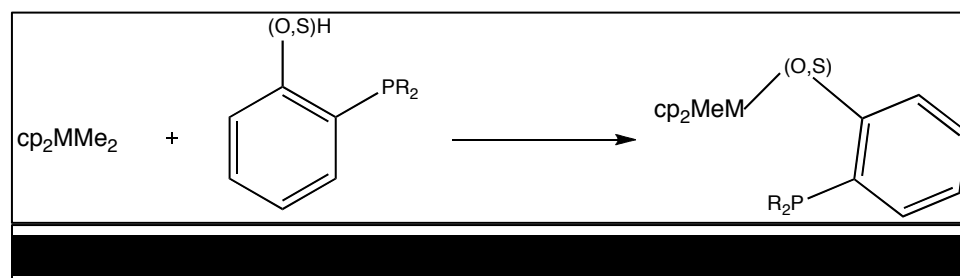
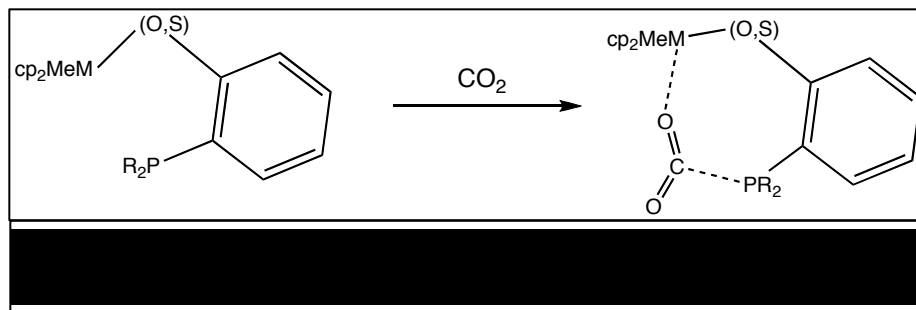
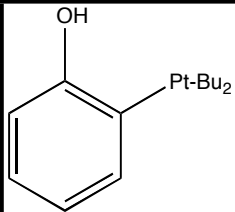
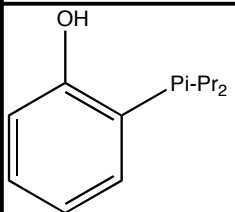
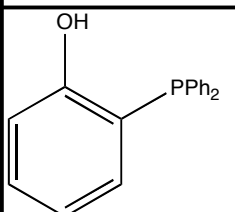
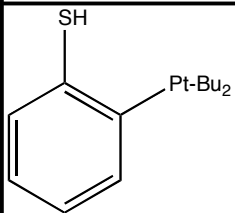
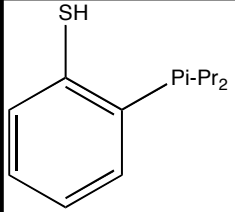
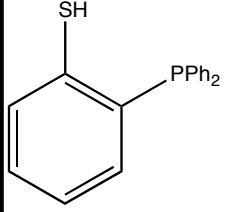


Table 2 may be used as a reference point, as it displays all the combinations of ligand-metal complexes that were explored for this research effort. The columns represent the metal center of the metal-ligand complex, while each row represents the six ligands. Detailed characterization data, including % yields, NMR, and elemental analyses for these complexes are provided in Chapter 4: Experimental.

The overarching goal of these complexes is to form an adduct-mediated complex with CO_2 (see Scheme 9). IR spectroscopy can easily determine if CO_2 has bound to the complex due to an obvious stretching frequency $1500\text{-}1700\text{ cm}^{-1}$. Since metallocenes are capable of shuttling electrons, it is hoped that CO_2 can be reduced electrochemically by forming these types of adducts.



		cp ₂ MMeL		
		M = Ti	M = Zr	M = Hf
1		7	13	19
2		8	14	20
3		9	15	21
4		10	16	22
5		11	17	23
6		12	18	24

2.3 Analysis of Neutral Metal-Ligand Complexes

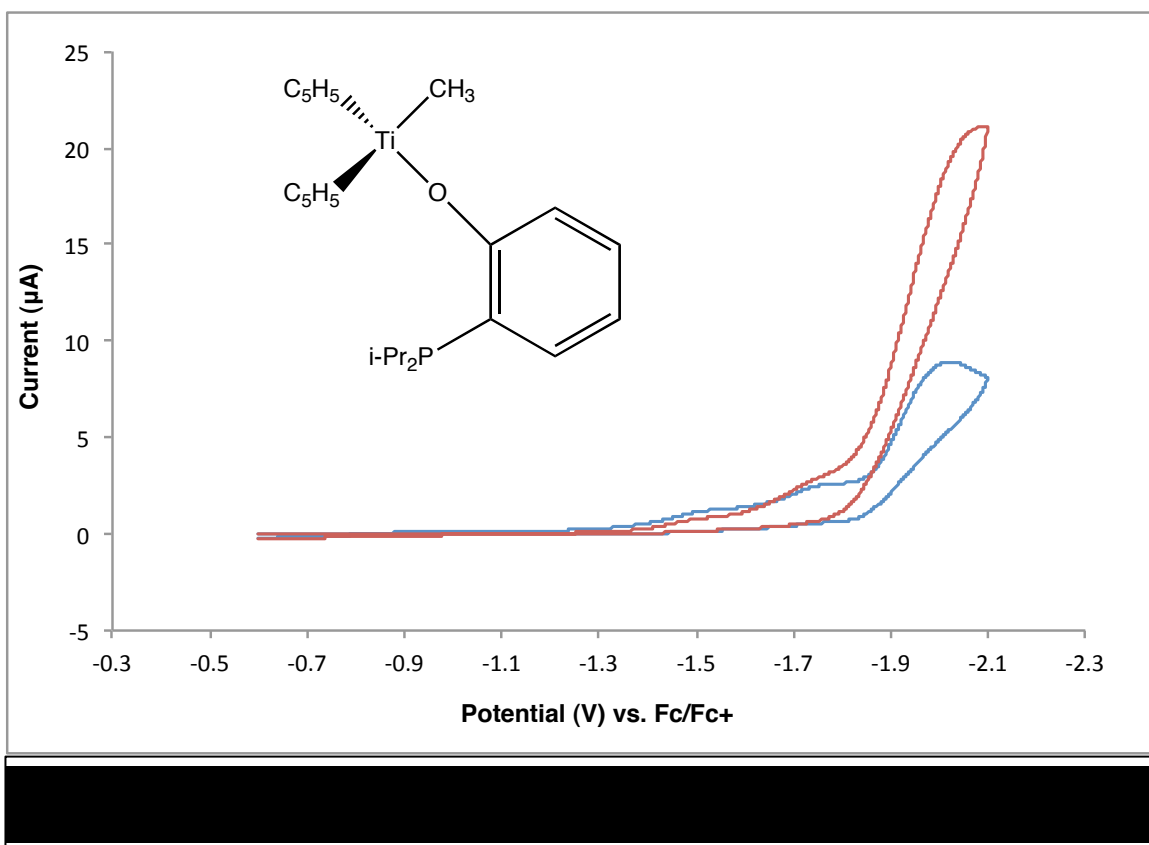
2.3.1 Titanocene complexes

Of the Group 4 transition metals, titanium has the smallest atomic and ionic radii. As such, $\text{Cp}_2\text{Ti}(\text{CH}_3)_2$ is the hardest Lewis acid used in the preparation of these mono-substituted metal-ligand complexes. $\text{Cp}_2\text{Ti}(\text{CH}_3)_2$ is very unstable when uncoordinated in THF—so much so that the complex undergoes α -elimination, forming methane and titanocene methylidene.⁶⁴ Typically, a solution of free ligand in THF was added dropwise to a stirring solution of the $\text{Cp}_2\text{Ti}(\text{CH}_3)_2$, and immediately methane bubbles would form with each drop. However, neither O nor S-derived di-*tert*-butylphosphine ligands readily formed visible gas bubbles. Redissolving the products into THF and precipitating them into pentane increased their purities significantly. The complexes **7-12** were successfully synthesized and isolated and are much more stable than the reactant, $\text{Cp}_2\text{Ti}(\text{CH}_3)_2$; i.e., they do not decompose over time.

Initial CO_2 reactivity was evaluated by dissolving the product in solvent, typically THF or CH_2Cl_2 , and bubbling CO_2 through the solution for 30 minutes. Then, the solution was evaporated onto a KBr plate within an Ar-filled glovebox, and IR spectra were taken. Bound CO_2 IR stretches are easily identifiable at $1600\text{-}1800\text{ cm}^{-1}$, but these could not be identified in any of the titanocene products. It is still possible that molecular CO_2 bound to the product and

evaporated with the solvent, so electrochemical methods were developed to determine if CO₂ bound to the complex *in situ*.

Electrochemical data was taken for each compound, and only a few complexes showed any significant increase or changes in reduction potentials under a CO₂ atmosphere. Changes in the current indicate resistance changes within the solution—a higher peak indicates a lower resistance. More importantly, a change in potential indicates that a different species is being reduced, which is indicative of a CO₂ adduct. A more positive shift indicates that the complex reduces at a thermodynamically lower limit than the free complex, while the opposite is true if the potential shifts more negatively. Compounds **7** and **10** showed no level of reduction curve increase. Figures 25-28 illustrate the titanocene products that did show some level of increase and changes in the reduction potential regime.



Each titanocene complex reduced from Ti^{4+} to Ti^{3+} between -1.7 and -2.0 V, relative to a ferrocene standard. Figure 25 displays the increase of reduction current to a near 2.5-fold increase (8.9 μA to 21.1 μA) for complex **8**. The shapes of the CV for each Ar-saturated and CO_2 -saturated environments are important. The Ar-saturated atmosphere peak is nearly completely resolved at the edge of the electrochemical window, and the CO_2 -saturated atmosphere peak begins to taper off near the edge of the electrochemical window. If CO_2 were being reduced in any of the complexes of this section, the reduction peak would be shifted away from the complex— anodically, or more positive, would be more thermodynamically favorable while cathodically would be more unfavorable. While the onset potential remains the same for both pre and post- CO_2 saturation,

it can be observed that CO₂ fosters an increase electron flow to the metal center. Further investigations are required, but one viable explanation for this sudden jump in electron flow is that the CO₂ molecules link the titanocene complexes together, essentially forming another layer of molecules that can be reduced at the electrode.

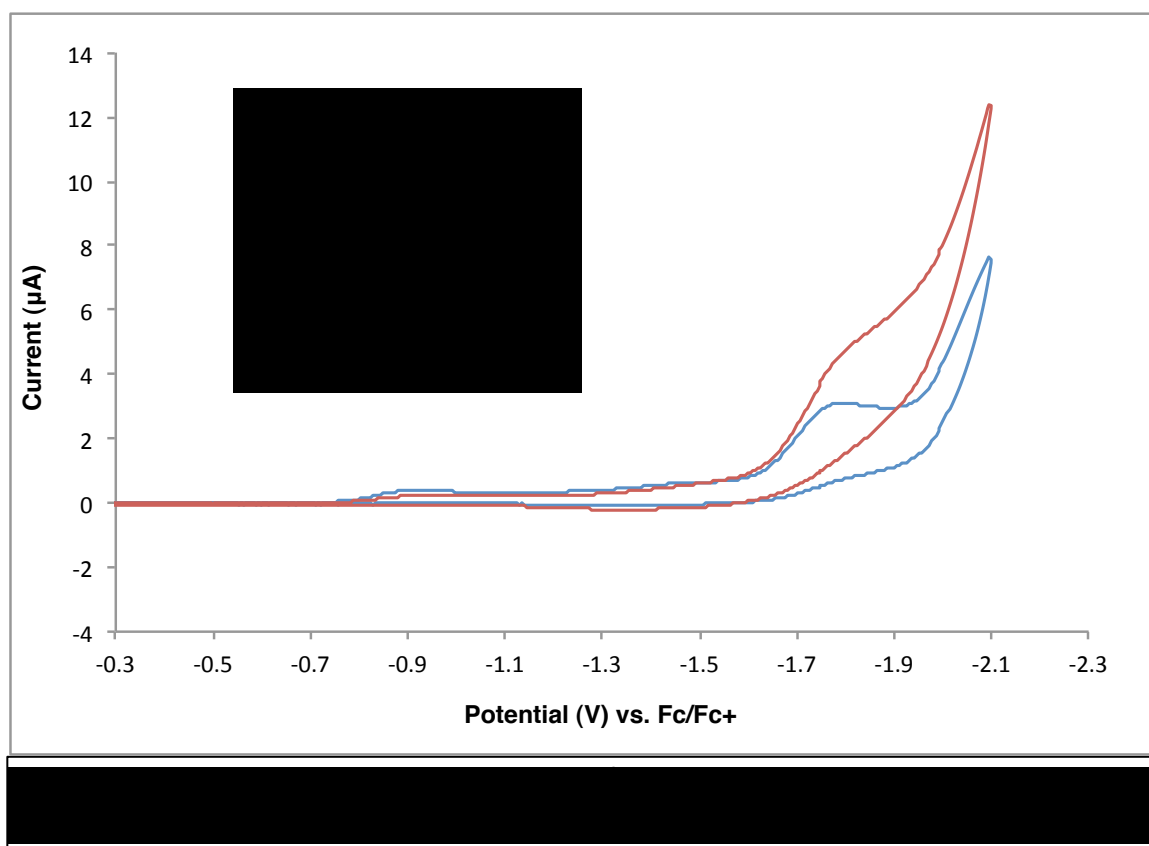
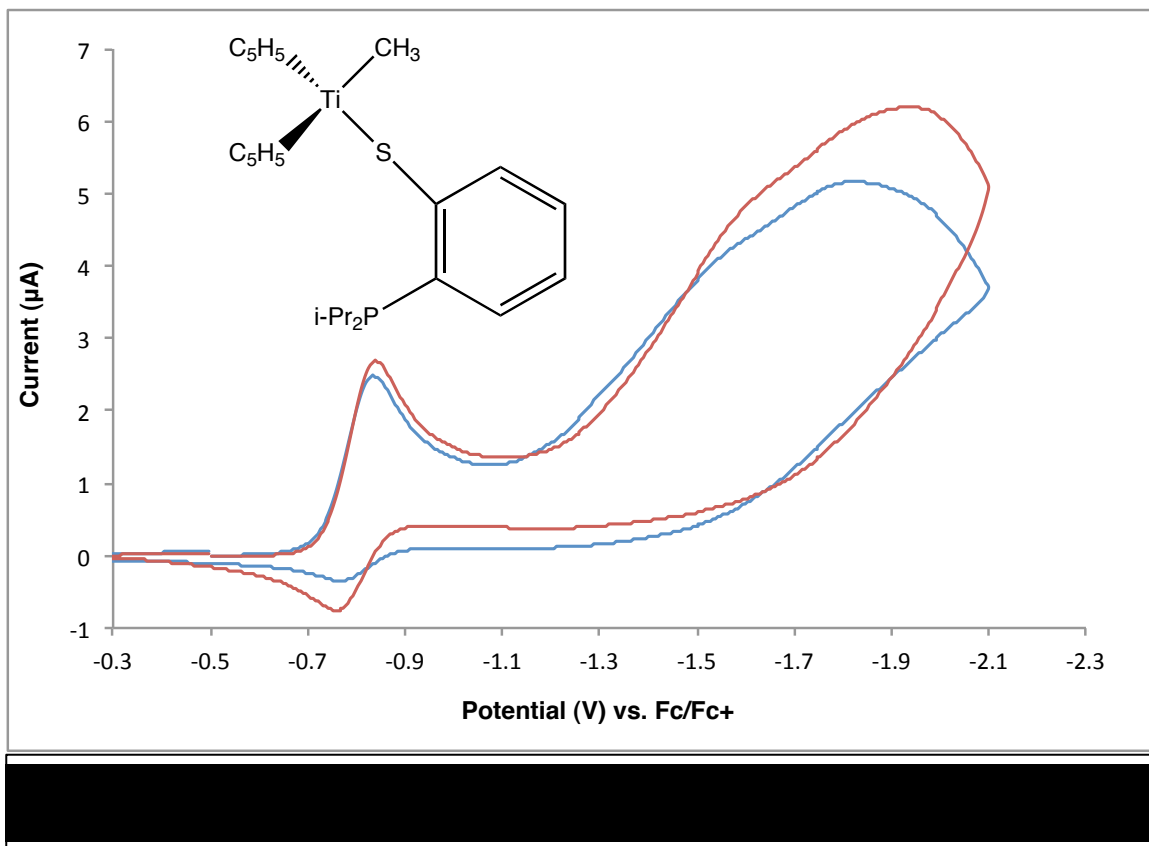


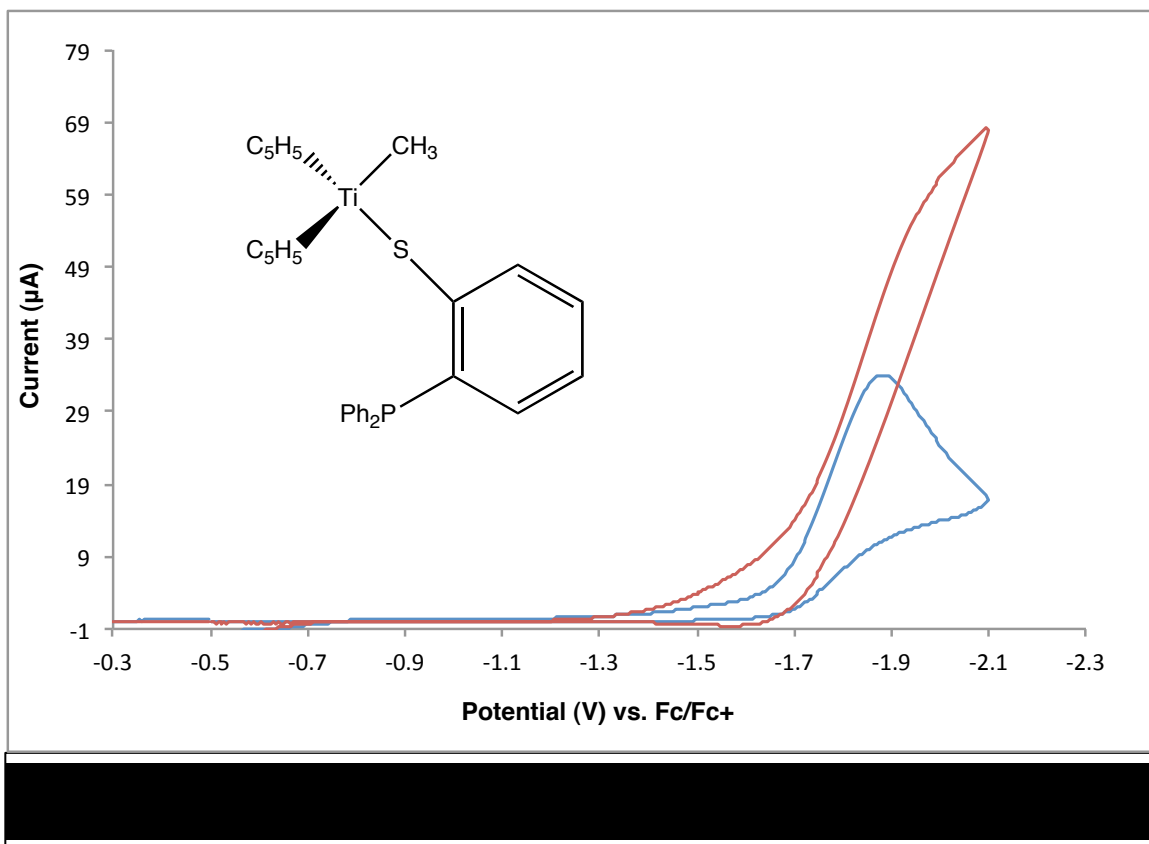
Figure 26 shows an irreversible adsorption of the reduced Ti³⁺ species in complex **9** (related to **8** with change of *i*-Pr to Ph groups on the phosphine), as the slope of the peak does not change as it approaches the end of the electrochemical window. These irreversible charge transfers are easy to identify because the layer it forms can be observed on the electrode without any

magnification. Again, CO₂ does foster an increase of current toward the metal center, forming the Ti³⁺ species at an increased rate.



The complete reversible redox reaction of Ti⁴⁺ to Ti³⁺ is observed in Figure 27 at -0.8 V. The unusual line shape cathodically located from this reversible redox is interesting in that it displays a large electron sink coupled with a slow mass transfer. The area under the curve indicates the amount of electrons transported into a complex, while the slope of the curve indicates the kinetic factor. In this circumstance using complex **11**, the area is quite large, and the

slope is small. This could be evidence of the reduced species forming a polymer, which would allow electron flow but would not diffuse through the electrolyte solution easily.

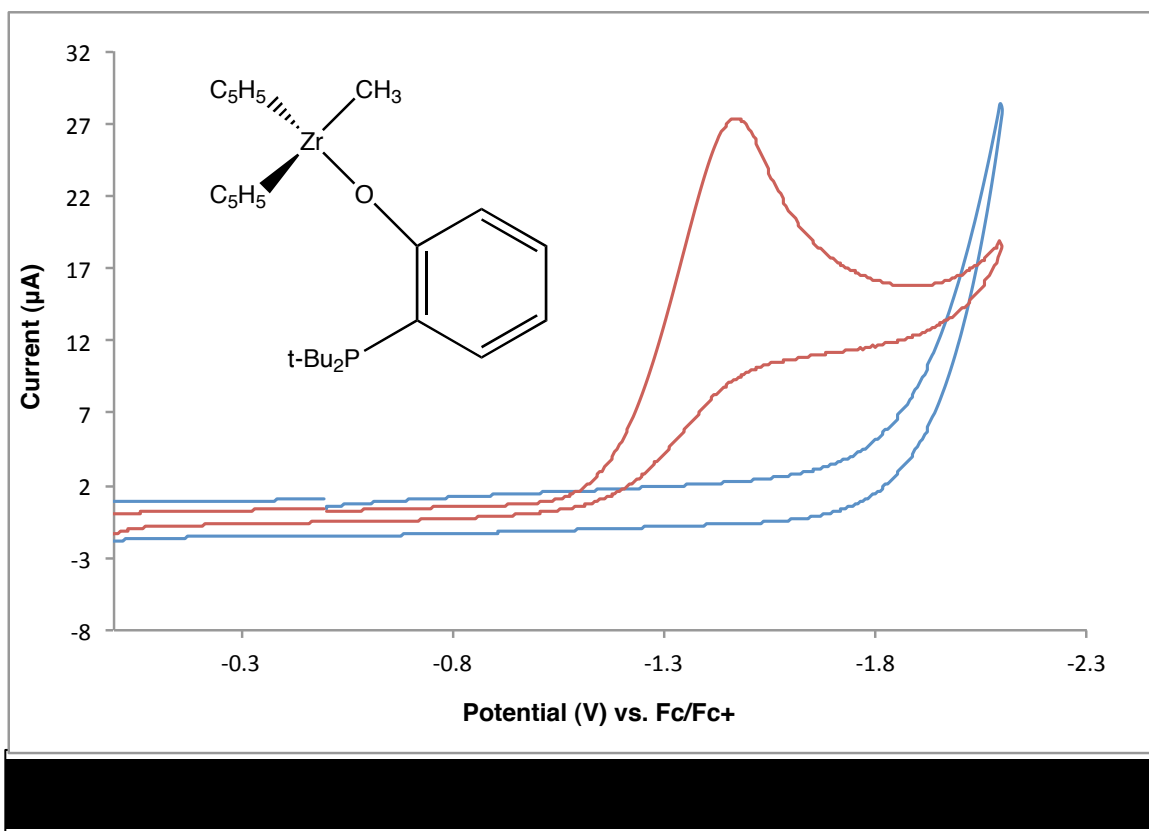


The reduction of complex **12** in Figure 28 displays an onset potential anodically shifted by approximately 0.25 V. The CO₂-saturated reduction peak does not get fully resolved in the electrochemical window, but it can be safely stated that the peak would be cathodically shifted than the Ar-saturated case. The CO₂ environment caused the migration of ions to occur sooner, but in this case, CO₂ increased the overpotential for reducing the metal center.

Initial IR studies of the titanocene products showed no persistent or stable interaction with CO₂. Applying upwards of 2.0 V to induce a charge transfer in the metal center also did not provide the chemical environment needed to bind CO₂ to the metal-ligand complex. In the next section, changing the metal complex to zirconocene derivatives was explored.

2.3.2 Zirconocene complexes

Of the three dimethylmetallocenes, the zirconium derivative is the easiest to manipulate and isolate. Each ligand behaved as predicted when reacted with a solution of the metal dichloride precursor, and as such, **13-18** were synthesized successfully in varying yields and were characterized by ¹H and ³¹P NMR

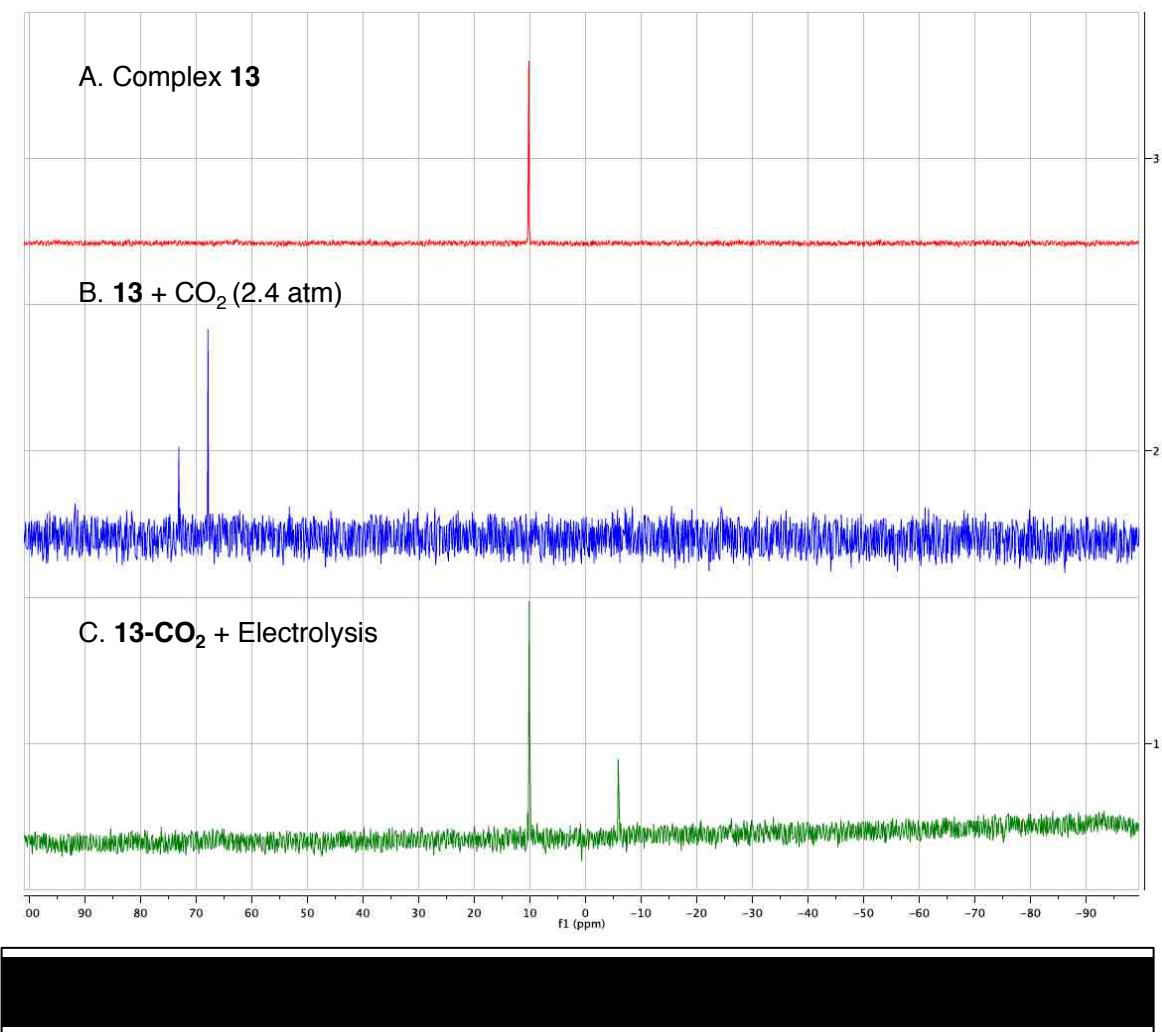


spectroscopies and later confirmed with elemental analysis. When CO₂ was bubbled through THF solutions of each compound, IR spectroscopy again confirmed that CO₂ did not form a stable adduct with the metal-ligand complex. Furthermore, only two compounds, **13** and **14**, showed any reactivity towards CO₂ during electrochemical experiments.

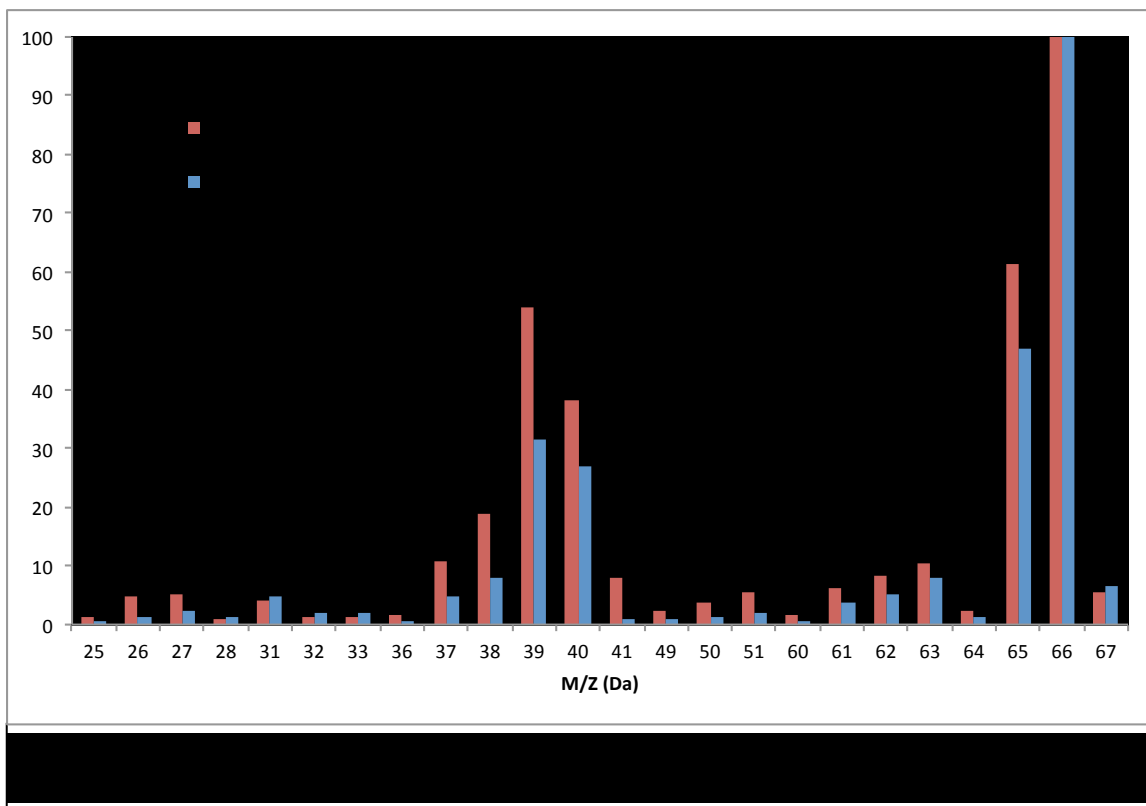
Figure 29 displays the electrochemical reduction of complex **13** in a CO₂-saturated environment. It is clear that CO₂ is being reduced electrochemically with a peak current at -1.44 V vs. Fc/Fc⁺. It is interesting to note that the cationic analog of this complex binds CO₂,⁶⁷ and yet we show that in a reductive environment, the neutral complex can also facilitate the reduction of CO₂. Attempts to crystallize complex **13-CO₂** for X-ray quality crystals were unsuccessful, both for an Ar(g) atmosphere and in a CO₂ environment.

Figure 30 displays the ³¹P NMR spectra comparing complex **13** in an Ar(g) atmosphere (red), a CO₂ atmosphere (blue), and the solution after electrolysis for four hours (green). ³¹P NMR spectra were obtained after 24 hours of CO₂ saturation, and nearly 100% of the complex signal is converted to two new signals at 68 ppm and 73 ppm. These new signals are evidence that CO₂ is interacting with the complex via the phosphorus bonding environment. The presence of the two peaks rather than one also indicates an equilibrium between two states—possibly a metal-bound CO₂ complex and a metal-unbound complex. Solid IR spectroscopy proved that the CO₂ adduct is not structurally stable, and the CO₂ escapes to the atmosphere. Solution IR spectroscopy was also

obtained (see Figure A7 in Appendix 3). A new stretching frequency does appear at 2338 cm^{-1} , but this is well outside the expected range of $1600\text{-}1700\text{ cm}^{-1}$. This new frequency is more than likely the result of dissolved CO_2 in the solution, which appears as a broad stretch from $2300\text{-}2375\text{ cm}^{-1}$.⁶⁵



Additionally, Figure 31 shows the mass spectrometry of the post-electrolysis products formed *in situ*. It was determined that this product is cyclopentadiene. This is an indication of the non-catalytic nature of this electrolysis, since ^{31}P NMR shows that ligand is released from the complex, and GC/MS shows the breaking apart of the metallocene.



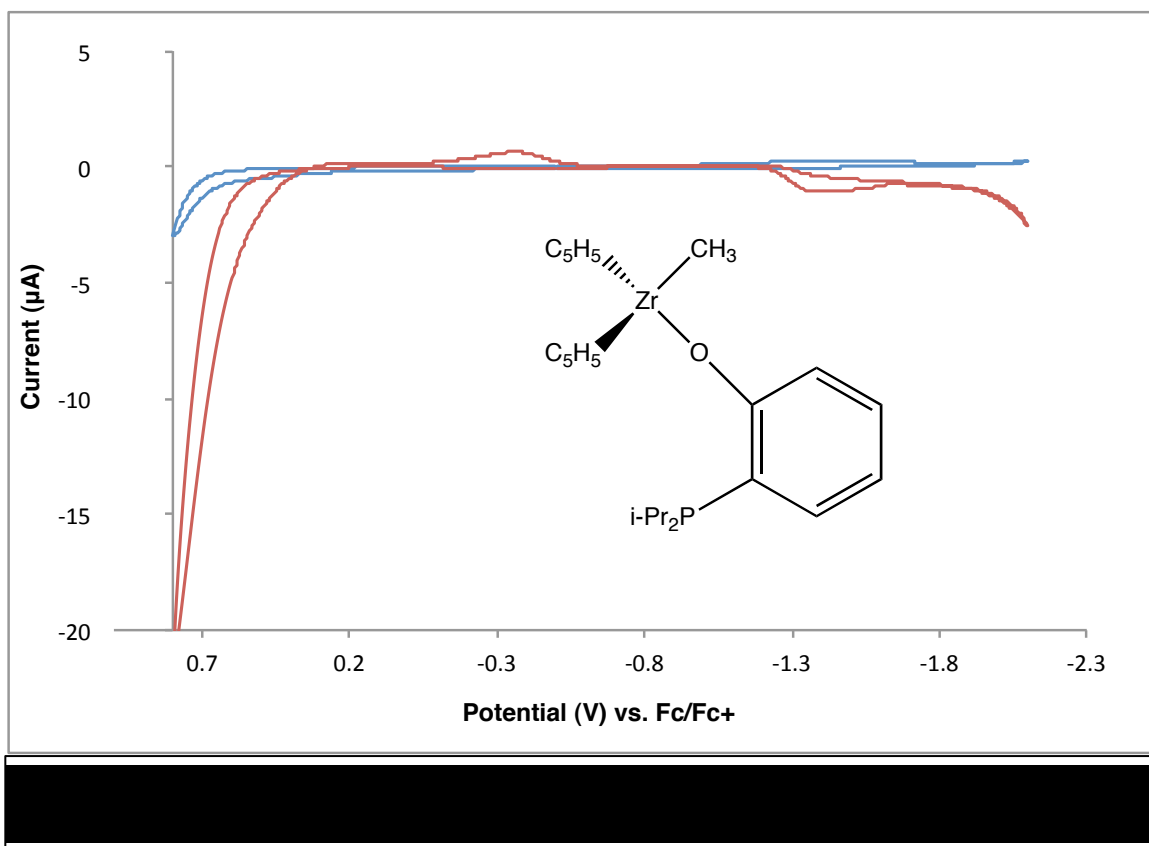
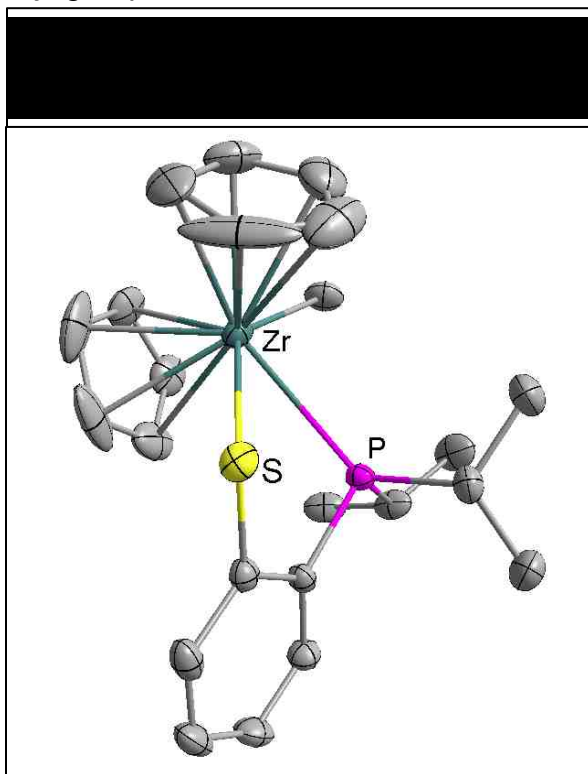


Figure 32 was included in this investigation because it is the only Group 4 metallocene complex in which its CV displays a prominent oxidation curve instead of a reduction curve. More than likely, the oxidation curve represents the oxidation of the ligand rather than the oxidation of Zr^{4+} or THF. The CVs of the free ligands in THF can be found in Appendix 1, Figures A1-A6.

Although complex **17** did not display a reduction peak in a CO_2 environment, the crystal structure was solved (see Figure 33). The Zr—S bond length is 2.6631(7) Å. The Zr—P bond length is 2.9174(8) Å. This was a surprising find since it was believed that the coordination sphere around the

zirconium ion was filled and that the methyl group needed to be removed in order for a Zr—P bond to form. Of all complexes with a Zr—P bond, the average bond length is 2.730 Å, while the maximum bond length is 3.033 Å (Cambridge Structural Database query was performed March 23, 2015). The Zr—P bond is within the top 10% when sorted by length, but this also provides the evidence that CO₂ can insert into the weak Zr—P bond as was hypothesized for the cationic complexes.



2.3.3 Hafnocene complexes

Dimethylhafnocene, a white powder when pure, was more time-consuming to utilize as a reagent because each new ligand-metal complex required a full 48-hour stirring period at room temperature. In an attempt to speed up reaction times, the hafnocene solutions were refluxed, but refluxing decreased the purity of the product significantly, as was evidenced by ³¹P NMR spectra. The long, two-day syntheses were enacted for each of the proposed hafnocene-ligand

complexes, **19-24**, and they were isolated and characterized by ^{31}P NMR and ^1H NMR spectra, as is shown in the experimental section.

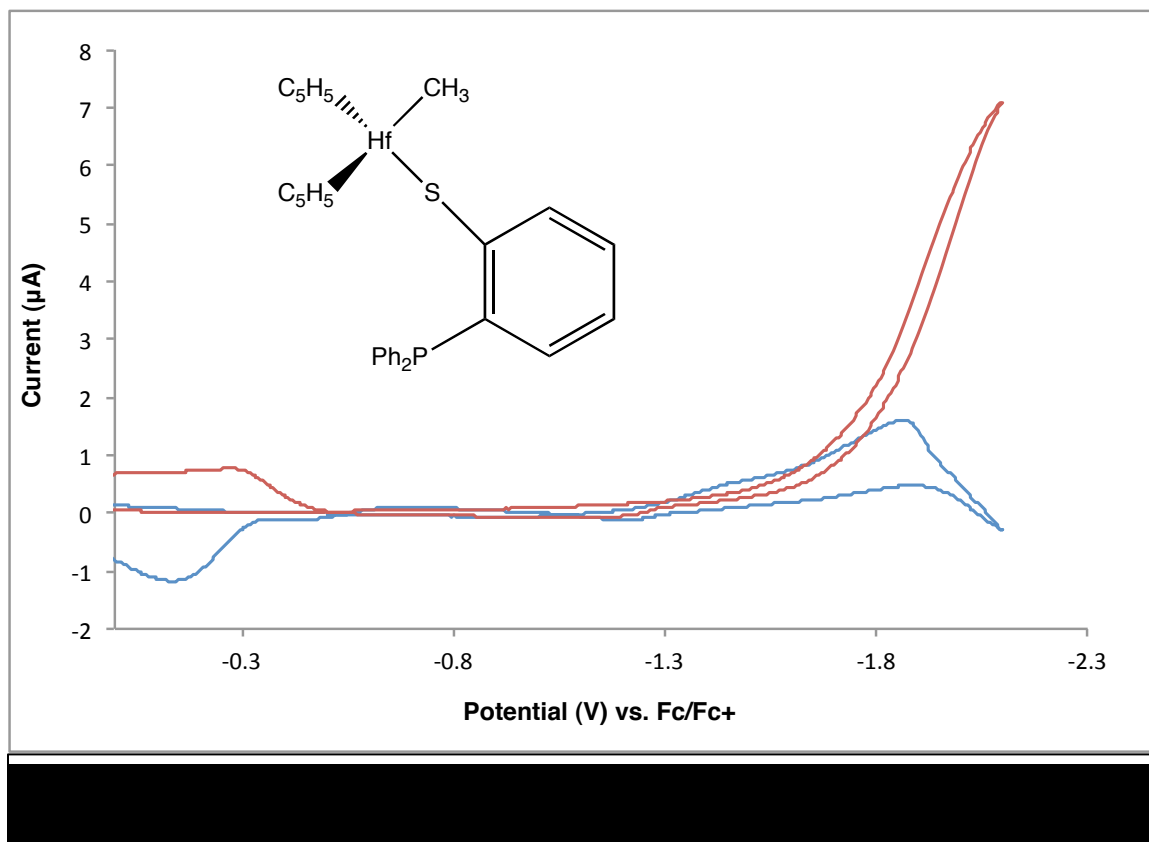
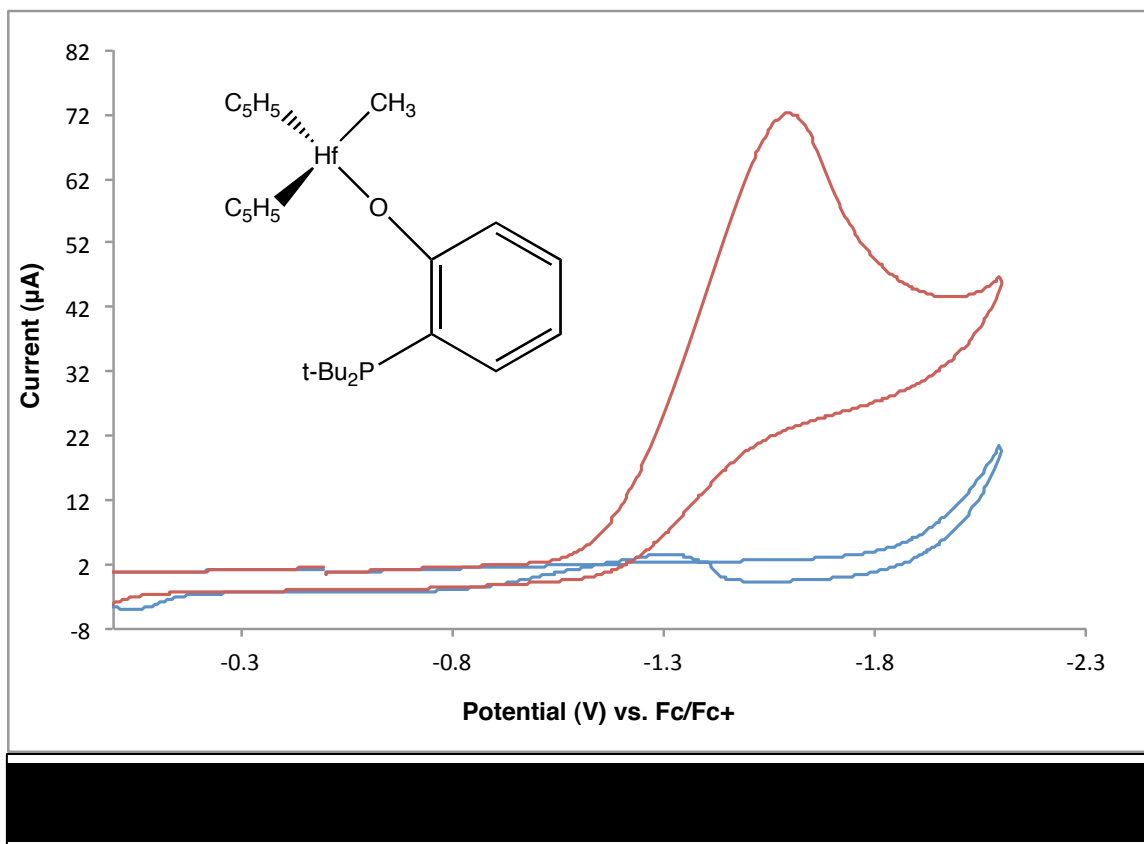


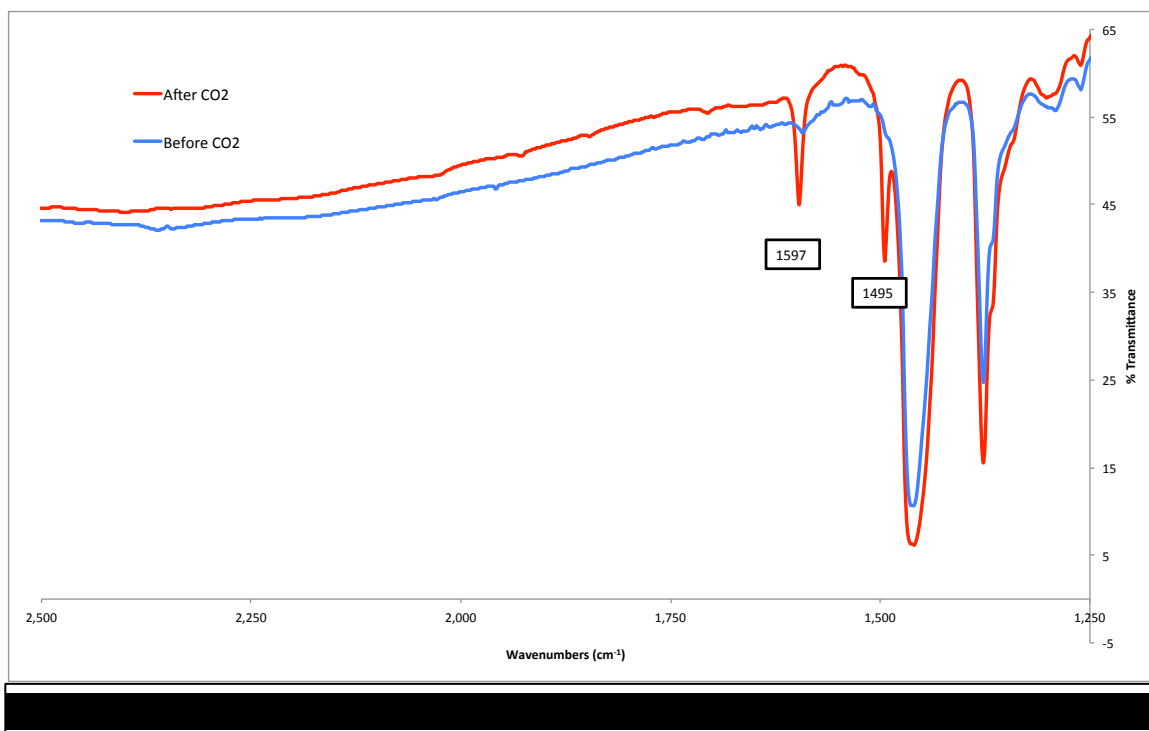
Figure 34, showing the Hf-complex of ligand **6**, displays a similar pattern observed in several other lighter Group 4 metallocene complexes discussed earlier. While IR spectroscopy did not show any stable attachment of CO_2 to the complex, it can be seen that the introduction of CO_2 to the system increased the current towards facilitating the reduction of the metal center.

Complex **19**, using the oxygen-ligated *ortho*-di-*tert*-butylphosphine, showed the most interesting behavior when reduced under a CO₂ atmosphere. As seen in Figure 35, it is very clear that CO₂ interacted with **19** in the electrochemical experiment, enabling a reversible reduction of the molecule. An oxidation was attempted through cyclic voltammetry, but there was no significant increase in anodic current within the electrochemical window. The symmetry of the peak indicates that the CO₂-bound complex does not adsorb onto the electrode. Rather, its electrochemical behavior is dependent only on its diffusion through the solvent.



IR spectra were obtained after bubbling CO₂ through a solution of **19** and CH₂Cl₂ for 30 minutes. The CO₂-saturated solution was evaporated in an argon-

filled drybox onto KBr plates. Two new frequencies appear when comparing the pre and post CO₂ saturation of the complex, namely at 1495 cm⁻¹ and 1597 cm⁻¹. This is indicative of CO₂ insertion into the Hf—P bond.



NMR spectra were procured for the CO₂-saturated solution as well. A J-Young NMR tube was filled with approximately 50 mg **19** and 1 mL C₆D₆. After proper evacuation with argon, the NMR tube was filled with ~35 psi (2.38 atm) of ultra-high purity (UHP) CO₂. The NMR tube was agitated and repeatedly inverted for 30 minutes, and then ¹H, ³¹P, and ¹³C NMR data were collected.

Figure 37 is the ³¹P NMR spectra obtained from the CO₂ experiments. Before CO₂ is added (red), it can be seen that complex **19** is pure. After the solution is purged with CO₂ (blue), two peaks form at 68 and 72 ppm, and we

also observe the original complex peak disappears. After four hours of electrolysis at -1.5 V vs. Fc/Fc⁺, the ³¹P NMR spectrum shows a 1:1 ratio of complex **19** and free ligand (green). It is important to note that complexes **13** and **19** behave very similarly; with the exception that more free ligand is present in the case of complex **19**. This could be because **19** is less stable than **13**, as is evidenced by the much longer reaction times to form **19** than **13**.

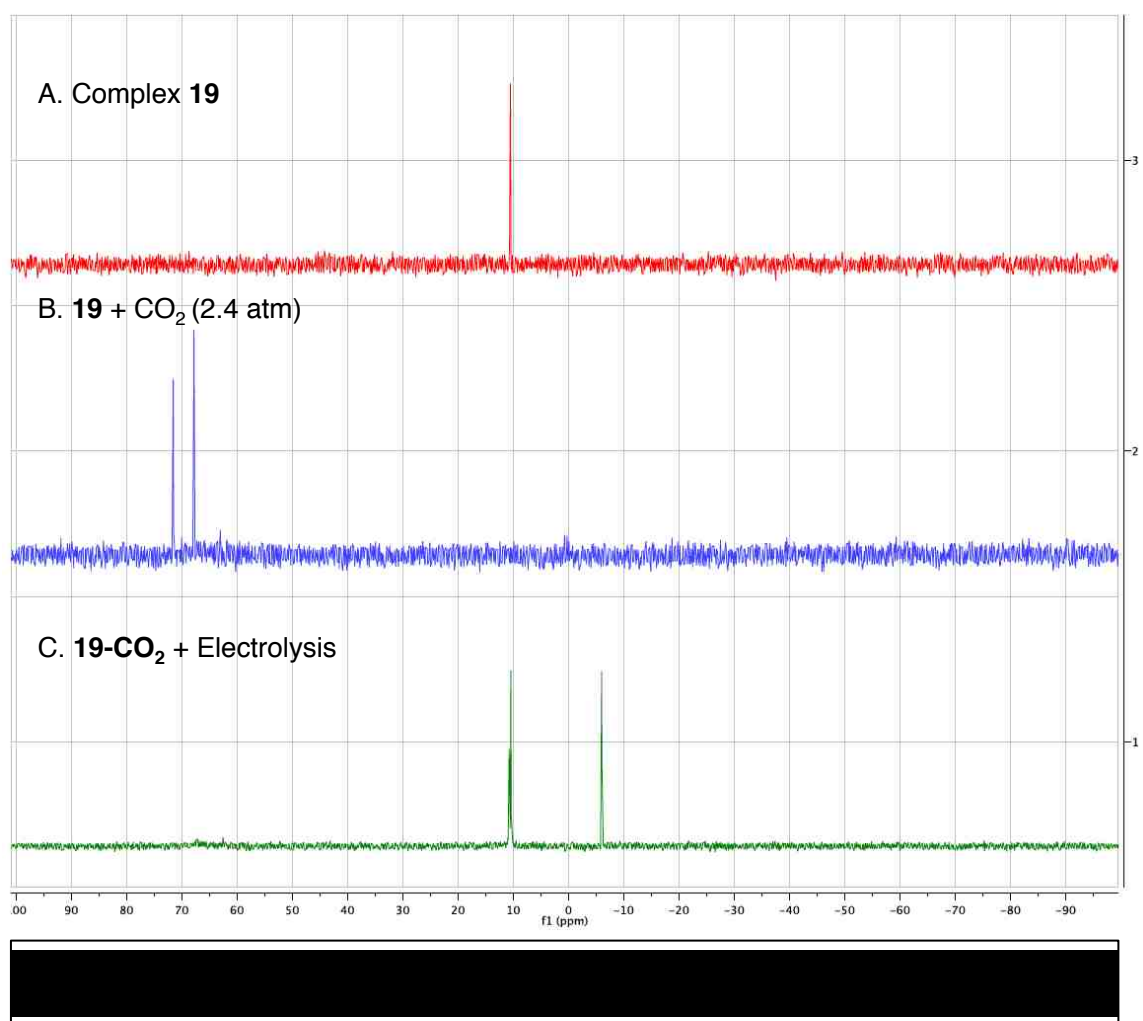
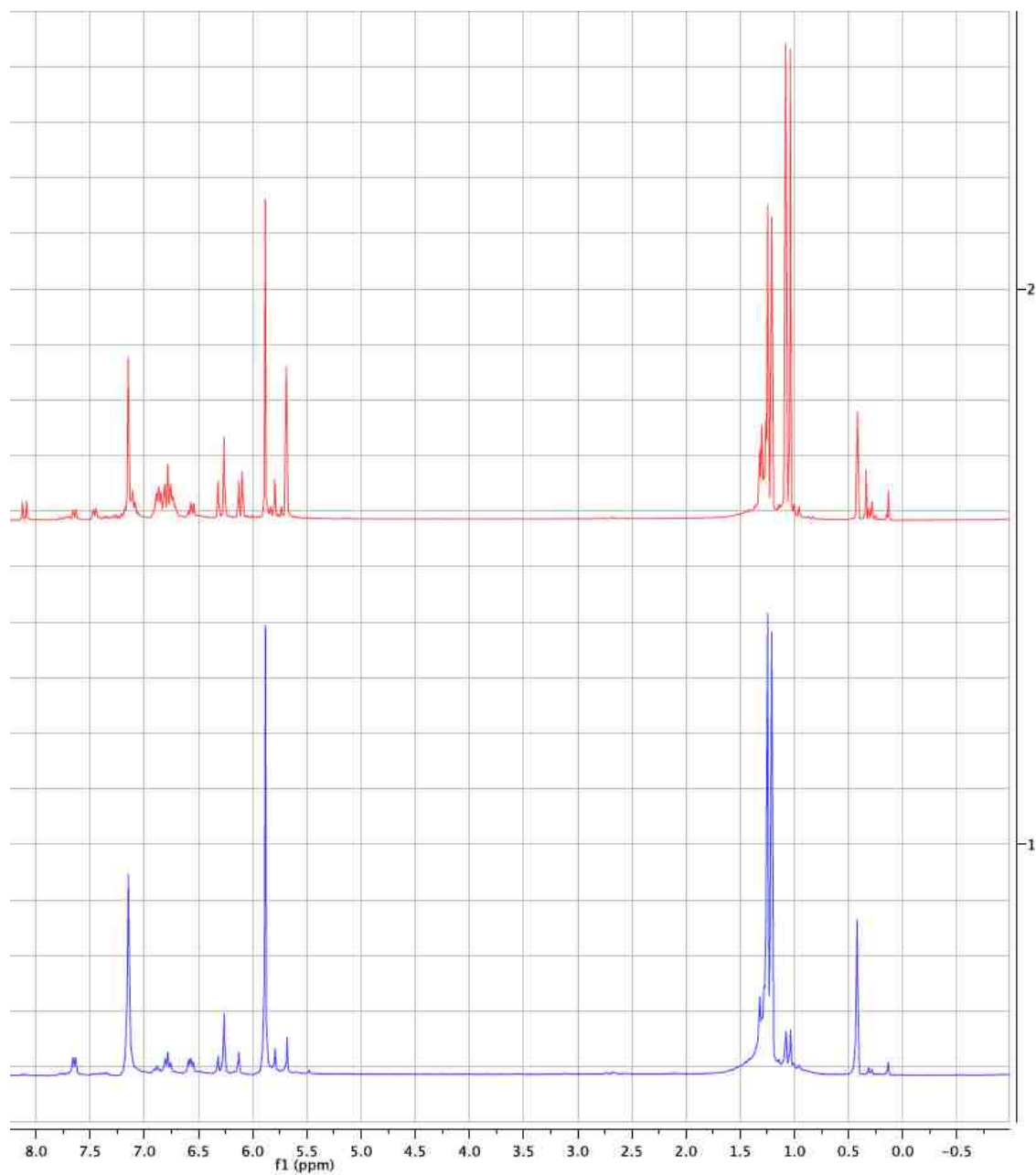
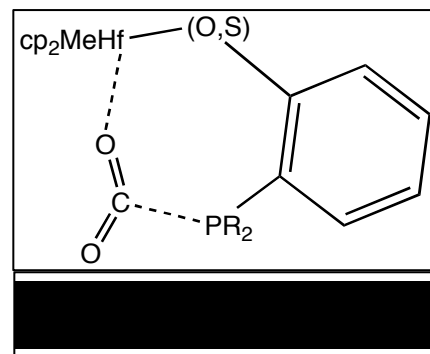


Figure 38 is the ^1H NMR spectrum of this same CO_2 reaction with **19**. The following signals of the blue spectrum (no added CO_2) will be identified for clarity. The singlet at 0.47 ppm represents the signal produced by the methyl group on the hafnium center. The large doublet at 1.24 ppm is accounted by the *tert*-butyl groups on the phosphorus atom, with a $J_{\text{P-H}}$ coupling of 11.5 Hz. The singlet at



5.86 ppm arises from the aromatic protons on the cyclopentadienyl rings. The large singlet at 7.15 ppm is simply the deuterated benzene in which the products were dissolved and is used as a reference peak. The remaining peaks in the aromatic region (6.66-7.61 ppm) are indicative of the various aromatic protons on the phenyl ring. When compared with the CO₂-saturated solution, several changes can be observed. First, the *tert*-butyl group is affected, showing that the phosphorus atom experiences a different environment when CO₂ is introduced. The appearance of two doublets indicates an equilibrium between two different complexes, as is also evidenced in the ³¹P spectrum. Second,

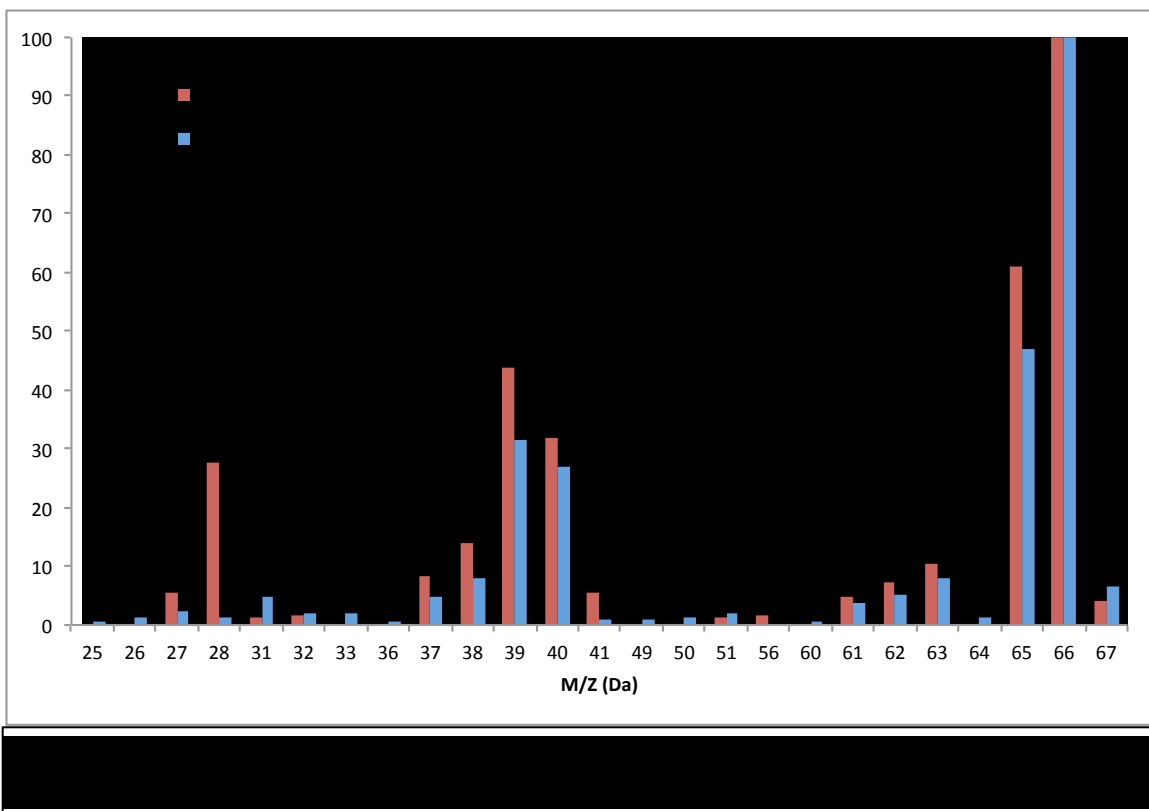


the cyclopentadienyl peak at 5.86 ppm shrinks considerably, and the peak at 5.72 ppm grows. If the hypothesis that the CO₂ environment is in equilibrium with two products, it can be imagined that the P-CO₂ interaction changes the environment surrounding the cyclopentadienyl ligands. Figure 39 is an illustrative example on how an adduct-mediated CO₂ molecule has a close proximity to the Cp rings, thus inducing a slight change in the proton environment around the cyclopentadienyl rings.

¹³C NMR experiments were conducted to identify the new peak in the metal CO₂ complex, but since the ¹³C isotope is only 1% abundant, we did not observe any new peak formation. We attempted purging the J-Young tube with isotopically labeled ¹³CO₂, but we again did not observe a new peak form. It is

hypothesized that since the maximum pressure output of the $^{13}\text{CO}_2$ lectern bottle is ~ 8 psi, it is quite possible that high pressures are required to bind CO_2 to the metal complexes.

Figure 40 displays the mass spectrum of a new product formed in the solution during the electrolysis of complex **19**. The spectrum has the same patterning as the electrolysis product found for complex **13** (see Figure 31, page 55), except for the new peak formed at $m/z = 28$, which indicates the formation of CO . It is shown that complex **19** does electrocatalytically reduce CO_2 to CO , however, the catalyst's half-life is determined to be approximately four hours, as is shown in the ^{31}P NMR spectra.



It is interesting to note that ligand **4** (2-di-*tert*-butylphosphinothiophenol) was the least reactive towards any of the three different metallocenes. The di-*tert*-butyl substituents on the phosphine group are the most sterically hindered, but the stability of the thiophenolic products might be better understood through HSAB theory. The sulfido group is more polarizable, and therefore, is softer than the oxo group. The ligand's role in complexation is the removal of a methyl group on the dichlorinated metallocene, and the methyl groups are hard. It is shown experimentally that the harder oxo group removes the methyl group much more easily than the softer sulfido group.

		Free Ligand	Metal Complex	Δ
Ti	O-tBu	-6.0	12.8	18.8
	O-iPr	-23.6	-8.8	14.8
	O-Ph	-26.8	-15.2	11.6
	S-tBu	18.9	22.1	3.2
	S-iPr	-2.4	-1.1	1.3
	S-Ph	-12.2	-11.5	0.7
Zr	O-tBu	-6.0	9.9	15.9
	O-iPr	-23.6	-7.4	16.2
	O-Ph	-26.8	-16.7	10.1
	S-tBu	18.9	23.3	4.4
	S-iPr	-2.4	11.6	14.0
	S-Ph	-12.2	16.5	28.7
Hf	O-tBu	-6.0	10.5	16.5
	O-iPr	-23.6	-8.1	15.5
	O-Ph	-26.8	-15.7	11.1
	S-tBu	18.9	23.5	4.6
	S-iPr	-2.4	0.1	2.5
	S-Ph	-12.2	-9.6	2.6

Table 3 is an overview of the ^{31}P NMR chemical shifts of all the neutral metal complexes in this research. For the titanium and hafnium complexes, the

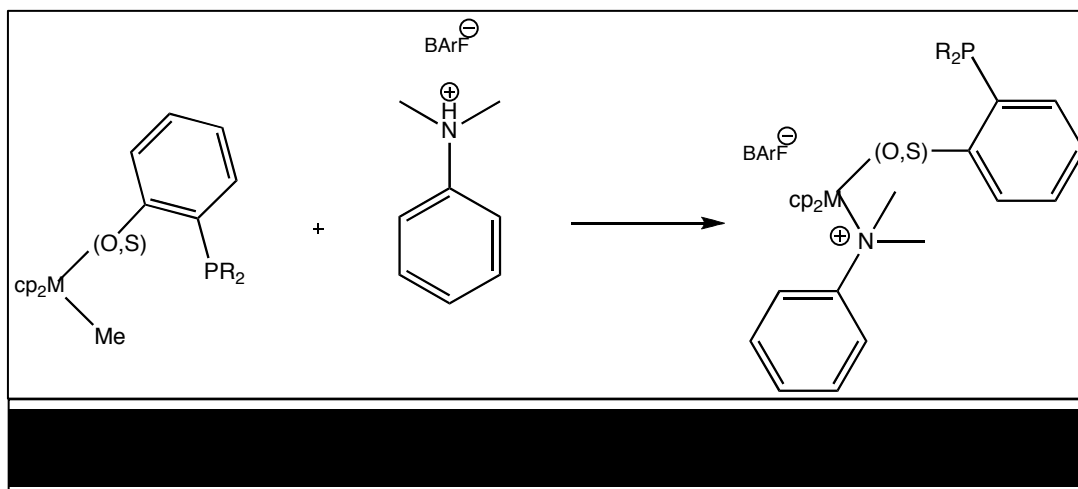
phosphorus environments were changed less in the thiophenolic complexes than in the phenolic complexes upon complexation to the metal. The opposite is true for the zirconium complexes. The positive changes in ^{31}P NMR chemical shifts is indicative of increased *s*-character for the lone pair on the phosphorus atom as it donates electron density to the central metal.

2.4 Analysis of Cationic Metal-Ligand Complexes

In order to enhance the chances to effectively form a dative bond to the metal center through the P atom-CO₂ molecular adduct as shown in Scheme 9 it was proposed that the final methyl group might need to be removed in order to reduce the strain on the coordination sphere around the metal and to increase the metal's acidity and acceptor ability. Simply, our goal was to create an environment in which the P atom could act as a "hinge" to allow CO₂ to bind between the P atom and the metal center. Removal of the added M-CH₃ group to form a cationic complex would clearly lead to a stronger metal-CO₂ binding mode via the lone pairs of electrons on the CO₂ oxygen atoms. Di-*tert*-butylpyridinium tetrakis(pentafluorophenyl)borane ([DTBP]⁺ [B(C₆F₅)₄]⁻) was used for this purpose because the di-*tert*-butylpyridinium cation is acidic enough to protonate the methyl group and as such the removal of the final methyl group could be actuated. Historically, dimethylanilinium tetrakis(pentafluorophenyl)borane [PhNMe₂H]⁺ [B(C₆F₅)₄]⁻ is considered highly

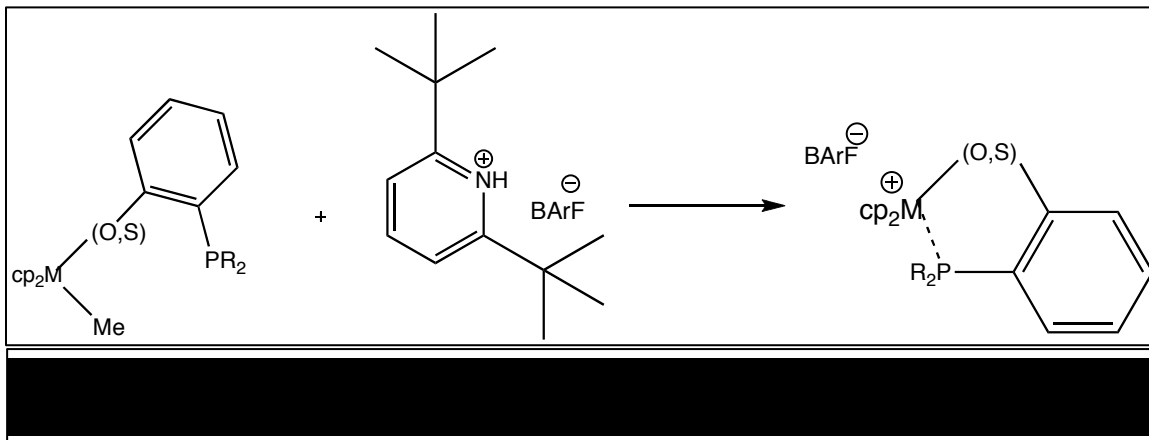
effective at removing the metal-bound methyl groups while also providing a large, non-coordinating anion to the newly developed metal cation. However, the resulting dimethylaniline can result in acid-base adducts of Group 4 metals which will form in the absence of other suitable bases (see Scheme 10).⁶⁶ Salts containing the $B(C_6F_5)_4^-$ anion are commonly given the sobriquet “Barf” salts, an anagram developed from “perFluorinated ARyl Borane”. Scheme 11 displays the removal of the final methyl group from the complex by protonation and forming another mole of methane gas.

2,6-di-*tert*-butylpyridinium $B(C_6F_5)_4^-$ was synthesized in two steps. First, $H^+[B(C_6F_5)_4]^-$ was produced by reacting four equivalents of lithium pentafluorobenzene with one equivalent of boron trichloride, and then acidification.⁶⁷ In the second step, the newly formed $H^+[B(C_6F_5)_4]^-$ compound was treated with 2,6-di-*tert*-butylpyridine to form the Barf salt.⁶⁸ The primary



reason for the large steric requirement (*tert*-butyls) on this reagent was to limit interactions of the free 2,6-di-*tert*-butylpyridine with the cationic metal complex

after generation. The *tert*-butyl groups limit the ability of the N lone pair to coordinate to the metal cations.

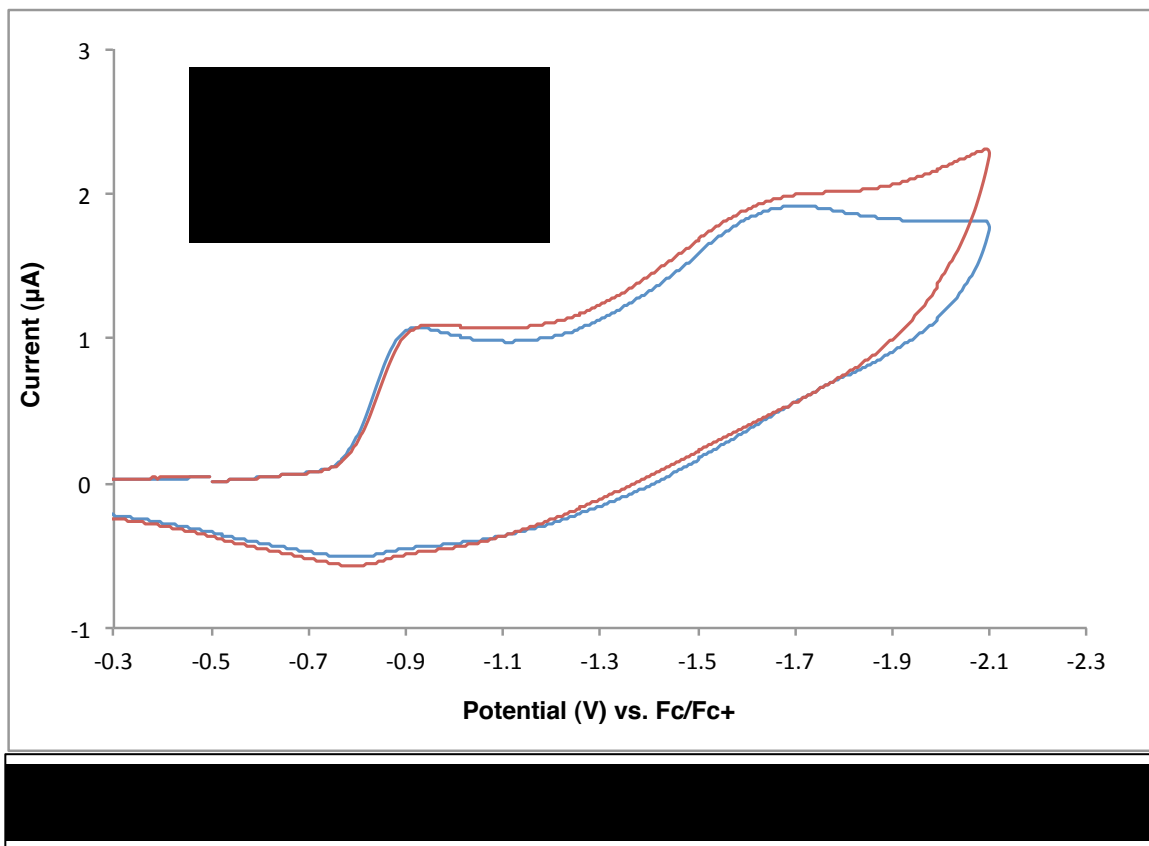


2.4.1 Titanocenium Complexes

After each of the neutral titanocene complexes, **7-12**, were reacted with molar equivalents of $[\text{DTBP}][\text{BArF}]$, cationic complexes **7⁺-12⁺** were successfully synthesized and isolated. When compared to the Zr and Hf analogs, the titanocenium products showed the largest array of color differences, ranging from bright orange to forest green to dark brown powders. Chapter 4 outlines the synthetic details, along with characterization data: ^1H NMR and ^{31}P NMR chemical shifts, % yields, and elemental analyses.

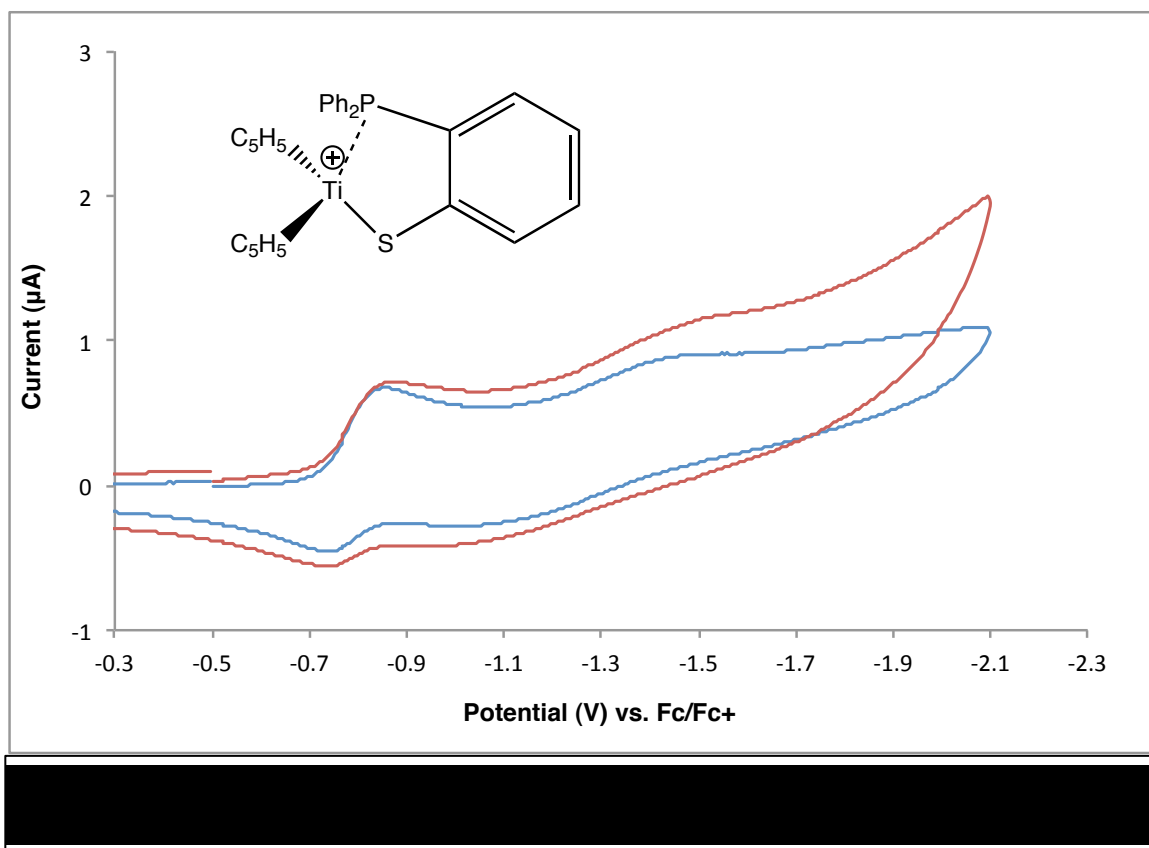
When CO_2 was bubbled through the CH_2Cl_2 solutions of each complex, again there was no evidence of stable CO_2 binding in IR spectroscopy experiments, as no metal-bound CO_2 complexes could be isolated. Similarly to

before, electrochemical data was procured for each complex and two titanocenium BARF salts showed slight increases in their reduction potentials when CO₂ was introduced.



First, Figure 41 displays the electrochemical reduction window of complex **9⁺**. It can be observed that there are two reduction peaks—one at -0.89 V, representing the reduction of Ti⁴⁺ to Ti³⁺, and another one at -1.68 V. The reduction of the metal center is never fully resolved, meaning that the current does not significantly drop after the peak current, indicating that electron movement is still facilitated beyond -0.9 V. In fact, the current steadily increases until the plateau of the second peak. The low slope of this increase is an

indication of the slow mass transfer of the reduced product, and the large amount of electron movement may indicate cross-linking or polymerization of the complex. The purging of the argon environment with CO₂ shows that neither of the two reduction peaks shows any difference in the current density. At the edge of the electrochemical window, CO₂ saturation did increase the current density, but this is probably due to the irreversible reduction of the solvent/CO₂/substrate system. If CO₂ were being reduced, a shift within the complex reduction peak would occur rather than the reduction of the metal center.



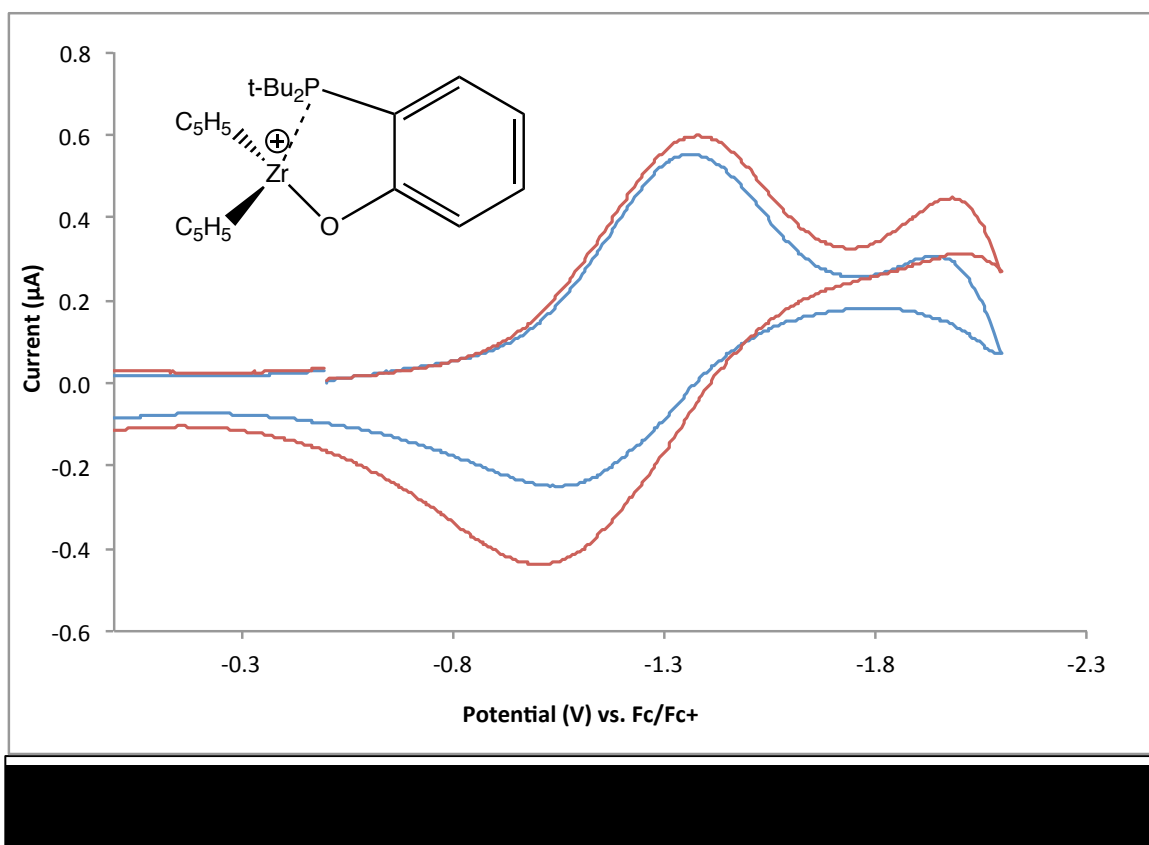
Next, **12⁺** showed very similar electrochemical behavior as **9⁺** (see Figure 42). There are two reduction peaks, the metal reduction appearing at -0.82 V, and the additional reduction at -1.5 V vs. Fc/Fc⁺. The difference between the

redox between **12⁺** and **9⁺** is that the thiol counterpart experiences a one-electron oxidation at -0.75 V. The large current density indicates that large overpotentials are being overcome to reduce the substrate. The newly formed Ti³⁺ substrate could be forming polymerization linkages—this would explain the large amounts of energy being deposited into the system, as large current densities are required to reorganize molecular geometries. The reversible oxidation peak at -0.75 V is intriguing in that it points to the fact that the oxidation curve from -2.1 V to -0.75 V is sufficient to oxidize the substrate before reversibly oxidizing the metal from Ti³⁺ back to Ti⁴⁺. CO₂ saturation does not aid in the reduction of Ti⁴⁺ in complex **12⁺**, but the saturation of CO₂ in the solvent increases the current density for the phase directly after reducing the metal. The CO₂ is not being reduced, but rather it is just increasing the overall current because it is within the solvent/substrate matrix, and it is being transported toward the electrode.

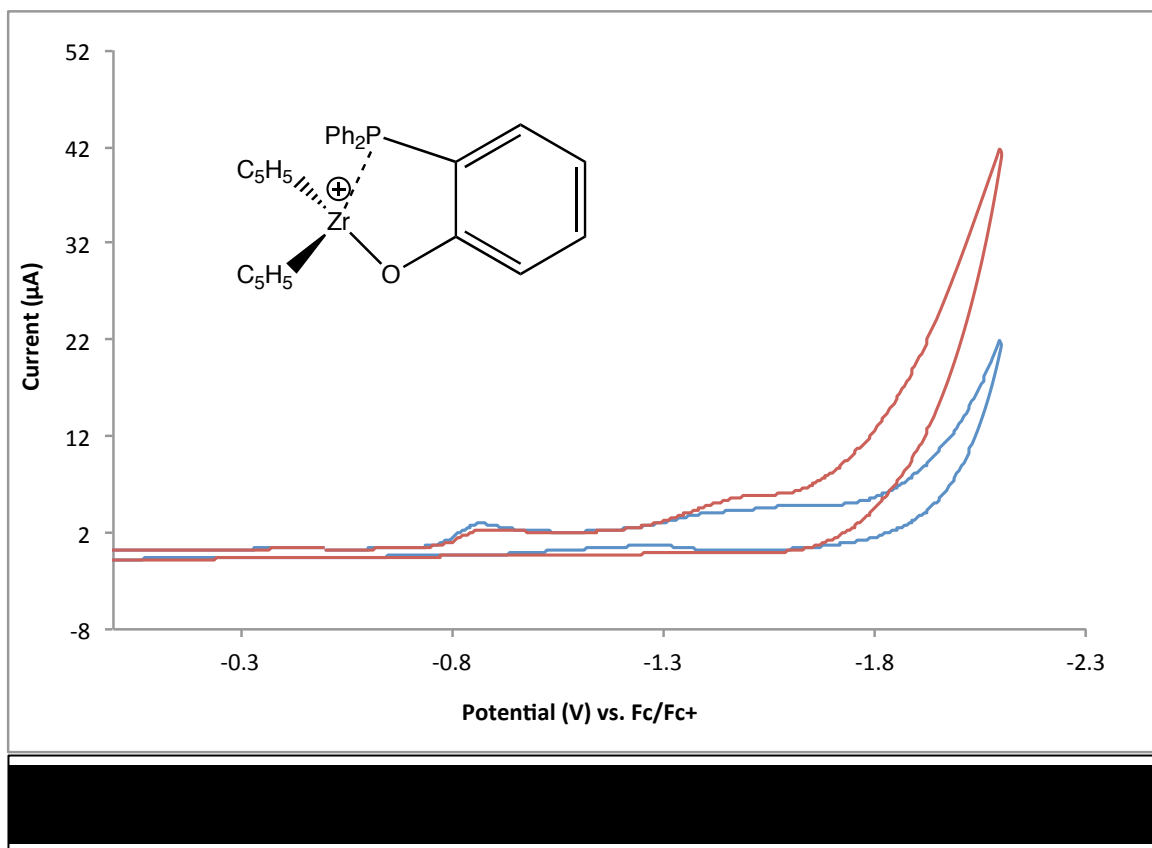
2.4.2 Zirconocenium Complexes

By adding [DTBP][BARF] to each zirconocene complex, **13-18**, only four of the six complexes formed a pure cationic metallocene. Attempted preparation of **14⁺** and **16⁺** yielded multiple peaks in ³¹P NMR experiments, thus indicating the formation of multiple products. Attempts to purify via crystallization yielded very little improvements in purity for these three compounds.

Figure 43 displays the CV data of complex **13**⁺ in the absence and presence of CO₂. Although **13**⁺ does not form a stable and isolable complex with CO₂, the electrochemical behavior is fully reversible in THF—a unique property among these types of complexes. Most of the complexes thus far either irreversibly adsorb onto the working electrode, or they form linkages after an initial reduction of the metal center. The calculated E_{1/2} of the Zr⁴⁺/Zr³⁺ redox is -1.21 V vs. Fc/Fc⁺ in 0.1 M Bu₄NPF₆ THF. An additional reduction peak occurs at -1.97 V, but due to the symmetric peak shape, the substrate is being reversibly reduced and is not part of an adsorbed or polymeric species. The increase of the



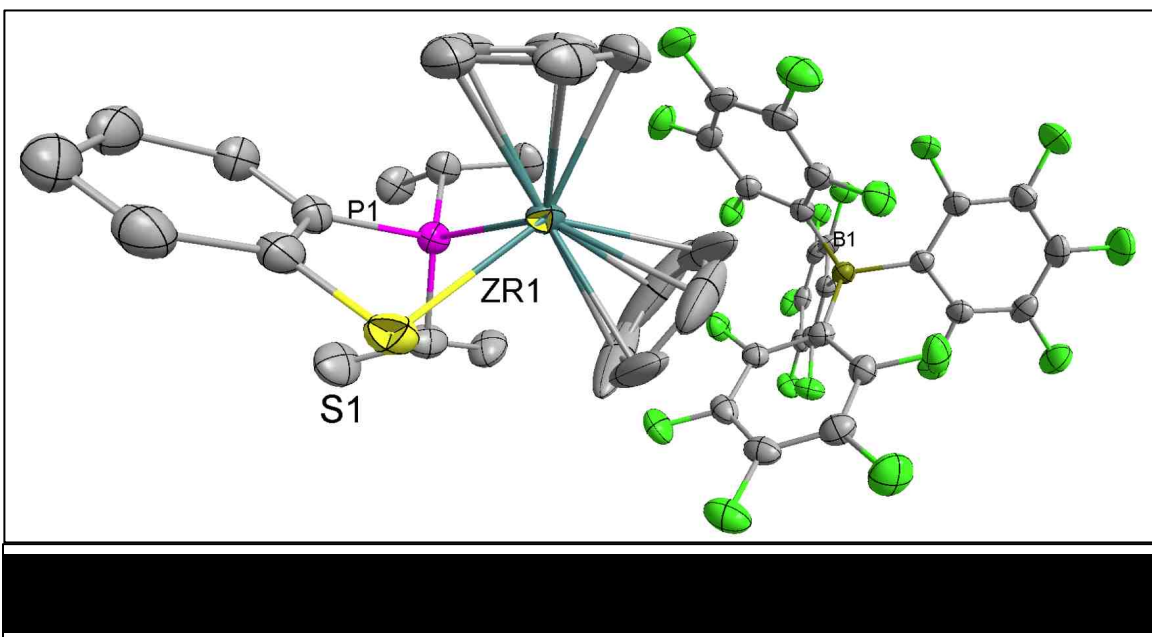
oxidation curve at -1.0 V vs. Fc/Fc⁺ indicates a fast 2 electron oxidation to bring the species back to Zr⁴⁺.



As was very common in the neutral metallocenes, the CV of 15^+ saw an increase in cathodic current, but the complex irreversibly adsorbed onto the working electrode. CO_2 did not necessarily strongly bind to 15^+ , as is evidenced by a lack of new stretches in the IR spectrum, but the CO_2 -saturated THF may have enabled an increase flow of electrons to the complex (see Figure 44).

The complex 17^+ was successfully synthesized as well, but it did not show any response to a CO_2 environment, electrochemically or otherwise. X-ray quality crystals were isolated, and the crystal structure provides fundamental information on the geometry of the cationic Group 4 species. It was hypothesized earlier that the removal of the second methyl group from the

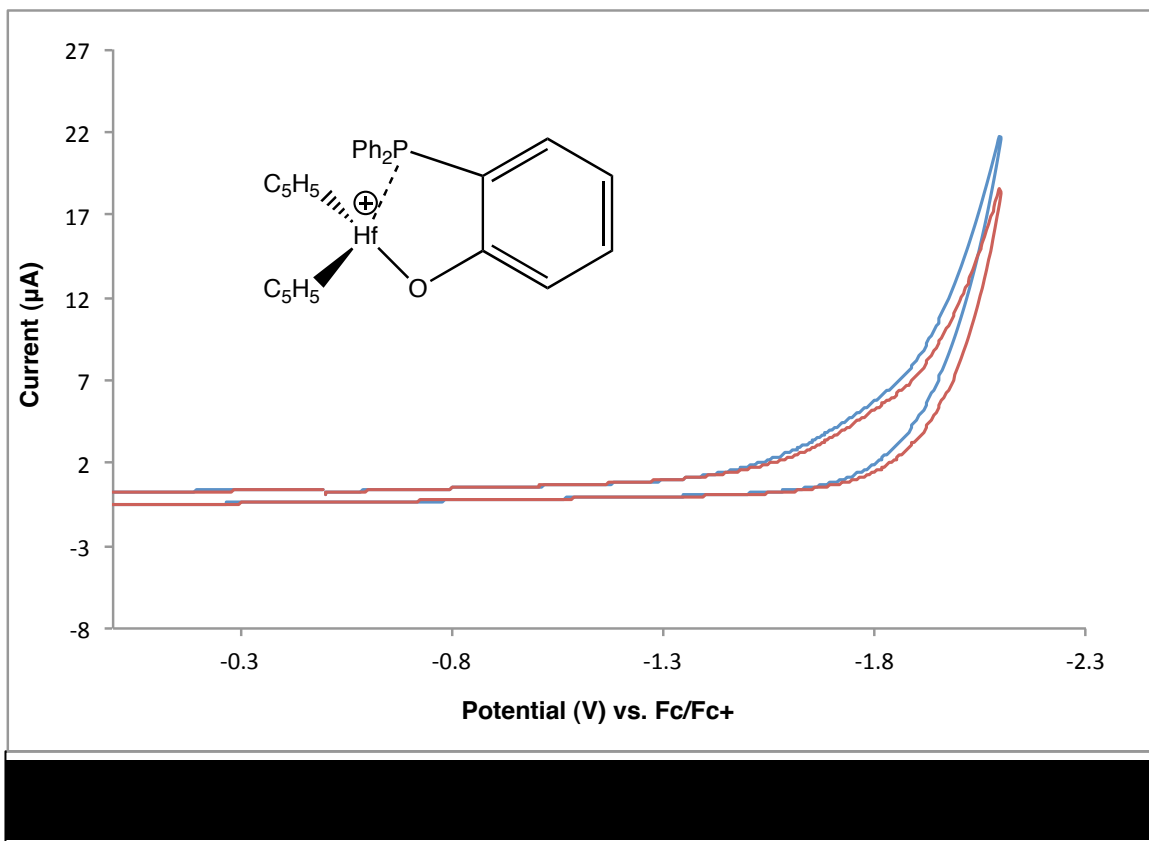
dimethylmetallocenes would open the coordination sphere around the central metal to allow dative bonding by the phosphorus atom. Figure 33 (the crystal structure for **17**) proved this hypothesis to be incorrect, in that the removal of just one methyl group opened the coordination sphere adequately to allow the formation of a M-P bond. When comparing the cationic Zr species with the neutral complex, it is observed that the Zr-S bond length shortens to 2.4841(6) Å from 2.6631(7) Å. The Zr-P bond length is 2.7217(6) Å, which is also shorter



than found in the neutral complex at 2.9174(8) Å. Comparing the crystal structures of these two products is very informative, in that CO₂ insertion is more likely with the neutral methylated metallocene complexes due to the lengthened Zr—P bond.

2.4.3 Hafnocenium Complexes

The cationic hafnocenium complexes took much longer to react than their titanocenium and zirconocenium counterparts. Instead of overnight stirring periods at room temperature, these required stirring at room temperature for 48 hours. Attempting to increase the rate of reaction by heating to reflux created several undesirable side products and less-pure products. All complexes were successfully synthesized and isolated as the only P-containing complexes (as per ^{31}P NMR spectroscopy), with the exception of **23**⁺. Crystallization attempts to further purify the complexes were unsuccessful. In the electrochemical



experiments, each product **19⁺**-**22⁺** and **24⁺** was subjected to a saturated CO₂ solution with no improvement of reduction or bonding of the CO₂.

Figure 46 shows a CV of **21⁺**, but it is also representative of the other cyclic voltammograms taken of the successfully synthesized hafnocenium complexes.

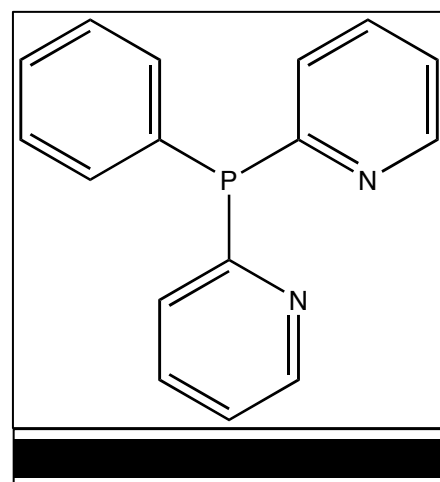
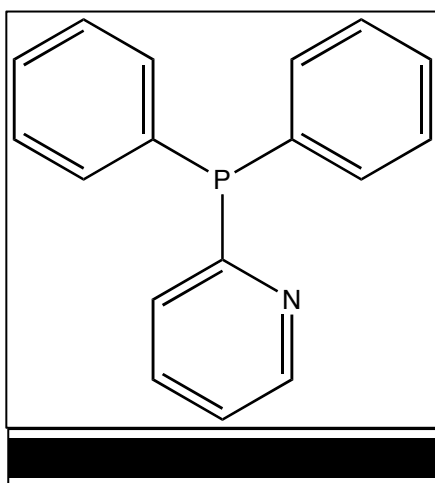
In each case, the compound adsorbs onto the working electrode as a more reductive potential is produced. CO₂ has no effect on these compounds, as is also evidenced by the lack of stable metal-CO₂ interactions as shown by IR spectroscopy.

Chapter 3: Zn(II) Complexes Used in CO₂ Reduction

3.1 Introduction

Although investigations into Group 4 electrocatalysis of CO₂ reduction is fundamentally interesting and important, it does not garner the same level of excitement as using earth abundant, non-precious metals in the same process. In fact, there have been recent advancements in earth abundant metals used in the catalysis of CO₂ into fuel precursors, *e.g.*, iron,⁶⁹ nickel,⁷⁰ and copper.⁷¹ Zinc was used as a starting point for this research based on its activating CO₂ as a Lewis acid.⁷² Also, it has been shown that the pyridinium ion electrocatalytically reduces CO₂ to methanol with palladium or platinum electrodes.⁷³ The objective for this research was to investigate novel pyridine-containing phosphine donor ligand attachments to zinc and determine their validity in electrocatalytically reducing CO₂.

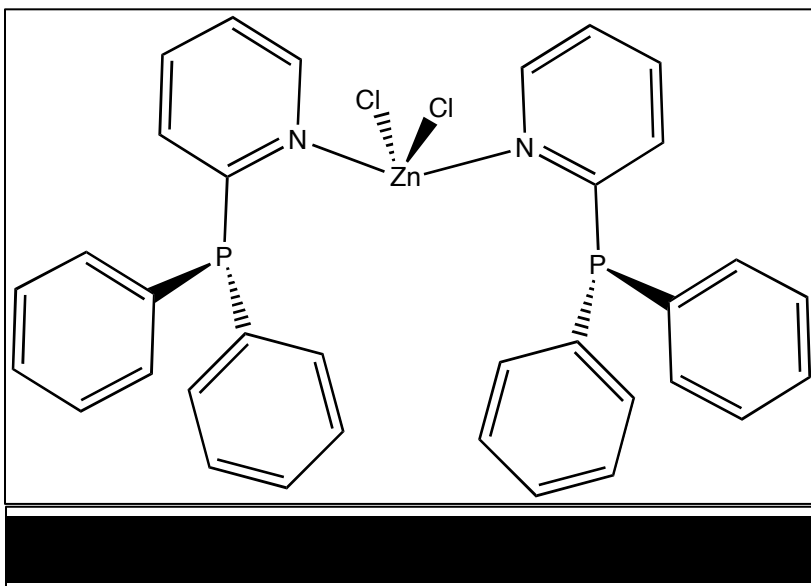
Primarily, two pyridylphosphine ligands were used in this research:



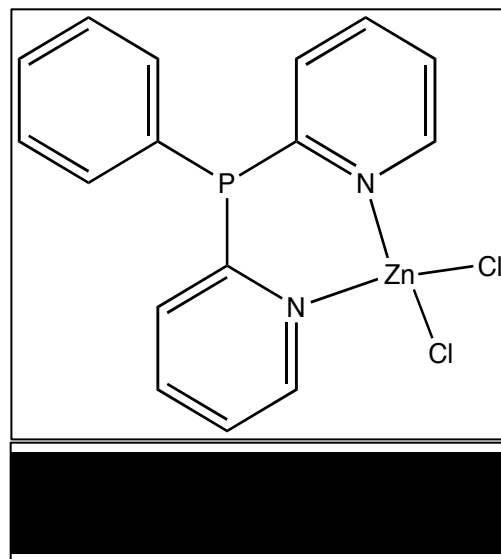
diphenyl-2-pyridylphosphine (Ph_2Ppy) and bis(2-pyridyl)phenylphosphine (PhPpy_2)—see Figures 47 and 48. HSAB concepts come into play with these ligands, as they have a hard binding donor via the N atom(s) and a soft binding core through the P atom. Zn^{2+} is an intermediate cation, meaning that it is known to bind to both hard and soft donors. There are several examples of Ph_2Ppy binding modes to transition metals. Ph_2Ppy binds through the P atom for Cu^{74} and Ru^{75} while bonding through the N bond is prevalent for Fe^{76} . The chelate effect for the PhPpy_2 ligand overpowers a soft-soft interaction through the P atom, as it preferentially bonds through the two N atoms to chelate to soft metals like Cu^{77} . It is important to note that the overall concept in this approach – to lower the reduction potential of CO_2 to other inorganic/organic compounds – resides on the same basic principle seen previously, that of lowering the overpotential required by creating Lewis acid-base adducts with CO_2 .

3.2 Ligand and Complex Preparation

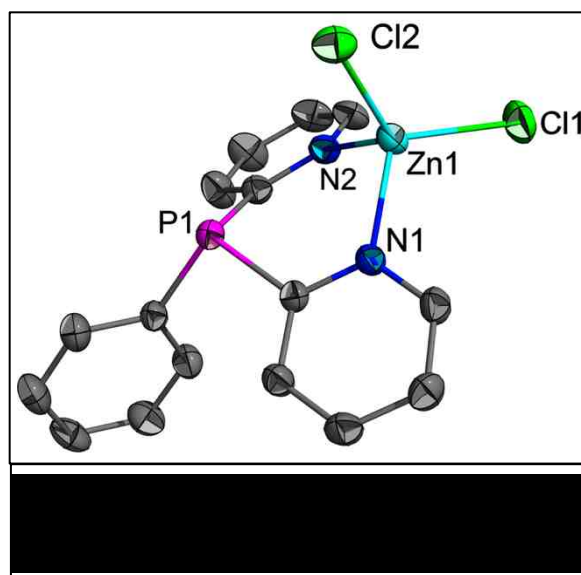
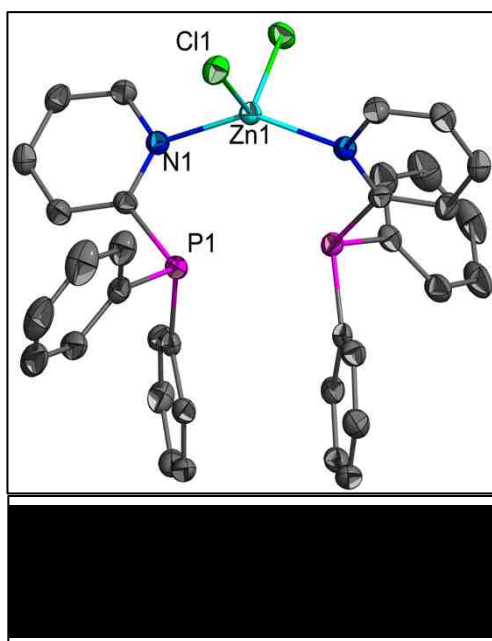
Ph_2Ppy is commercially available, and PhPpy_2 was synthesized in the lab. PhPpy_2 is



formed by lithiating 2-bromopyridine and combining the lithiated product with a solution of ether-bearing dichlorophenylphosphine. Complexes **25** (Figure 49) and **26** (Figure 50) were synthesized by combining stoichiometric amounts of each respective ligand with ZnCl_2 . Each compound was isolated, and



the purities were determined by ^1H and ^{31}P NMR spectroscopies. It was assumed that **26** would form by chelation through two N atoms, but since Zn^{2+} is intermediate between hard and soft acids, it was unknown whether the ligands of **25** would bind through the N or P atoms. Initial NMR results of **25** and **26** showed similar shielding around the protons and the phosphorus atoms, indicating that **25** probably complexed to Zn through the N atom. This binding



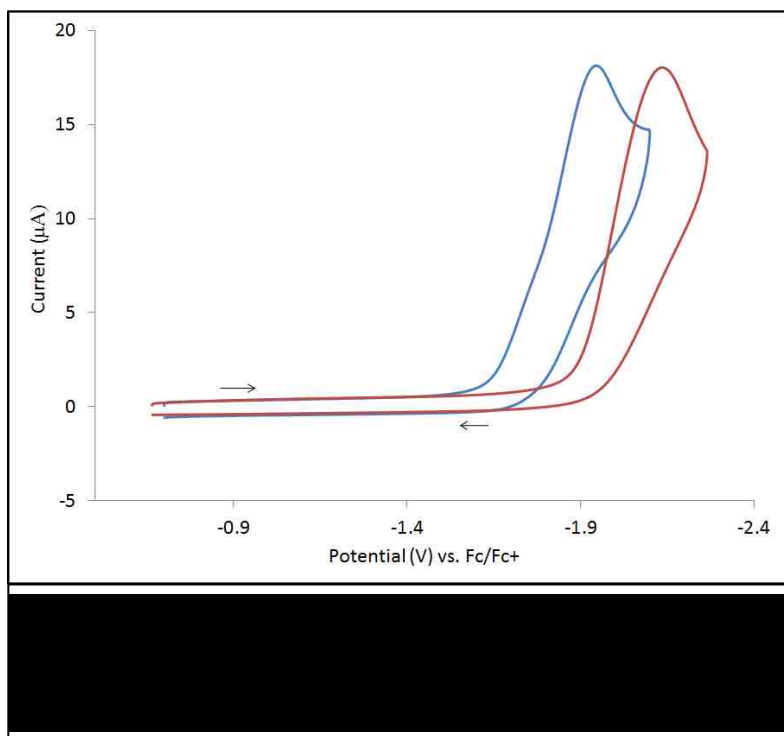
motif was confirmed by single-crystal X-ray diffraction (see Figures 51 and 52).

Both complexes exhibit a distorted tetrahedral geometry at the Zn center with similar Zn-N bond lengths (For **25**: Zn1—N1, 2.067(4) Å; Zn1—N2, 2.061(4) Å. For **26**: Zn1—N1, 2.092(2) Å; Zn1—N2, 2.092(2) Å). The most notable differences between the two compounds are the denticity of the ligand attachment and the N-Zn-N torsion angles. **25** has two monodentate ligands attached, while **26** has one bidentate ligand. The free rotation of the Zn—N bond in complex **25** could give greater access to the lone pair electrons on each P atom, opening the way for CO₂ insertion. The torsion angles around the Zn are very different as well, 145.58(10)° in **25** as opposed to 92.92(15)° in **26**. The typical dihedral angle for a tetrahedral geometry is 109.5°, and the deviation from this standard in both complexes is due to the particular ligand attachment. In complex **25**, the two P atoms have extended p orbitals that repel each other, giving way to a larger N—Zn—N angle. In complex **26**, the boat-like conformation of the six-membered ring formed by the double attachment through the N atoms indicates that the chelation effect causes this constrained dihedral to be thermodynamically stable.

3.3 Results and Discussion

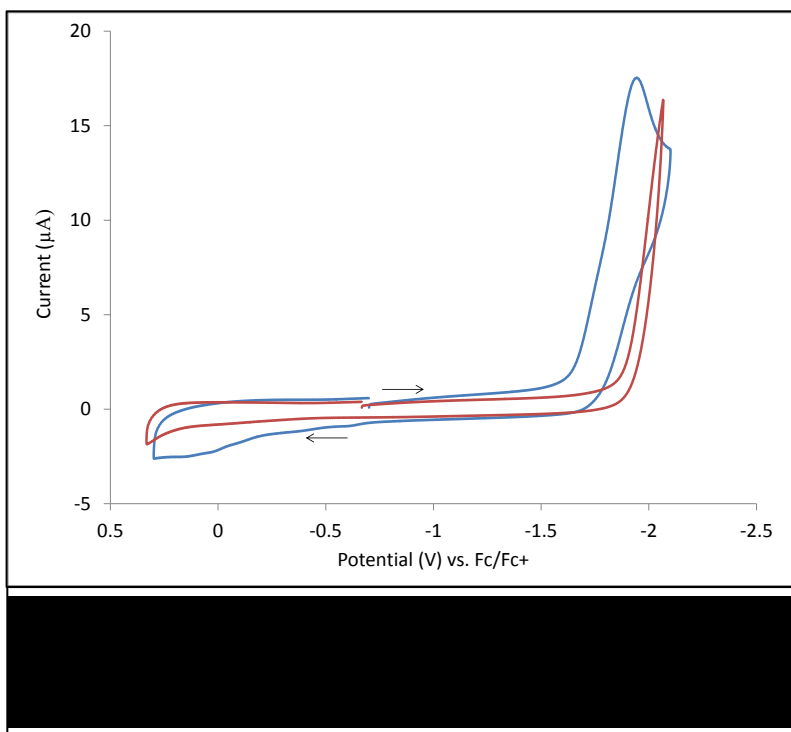
The first experiment to conduct with **25** and **26** was to determine their redox reversibility. At a glassy carbon working electrode interfaced in THF, both

25 and **26** undergo an irreversible 1-electron reduction at half-wave potentials of -2.03 V and -1.80 V vs. $\text{Fc}^{0/+}$, respectively. Figure 53 displays the cyclic voltammograms of each complex. By integrating each peak and comparing the



result with ferrocene *in situ* (ferrocene undergoes a reversible 1-electron reduction),^{78, 79} it was determined that complexes **25** and **26** are reduced by one electron—formally Zn^{2+} to Zn^{1+} . The appearance of the low valent Zn^{1+} species is rare,⁸⁰ and the negative potential required to reduce both species is indicative of an inner-sphere electron transfer to the 4s orbital, since the 3d orbital is already filled.

The increase of aromatic phenyl rings surrounding the Zn center in **25** gives rise to a more electron-rich Zn^{2+} ion, thus making it more difficult to reduce **25** than **26**. The entire electrochemical window was swept for reversibility (see Figure 54), but an oxidation curve was undetectable (as expected). Diffusion tests were also established for **25** and **26** (Figure 55), and it was determined that

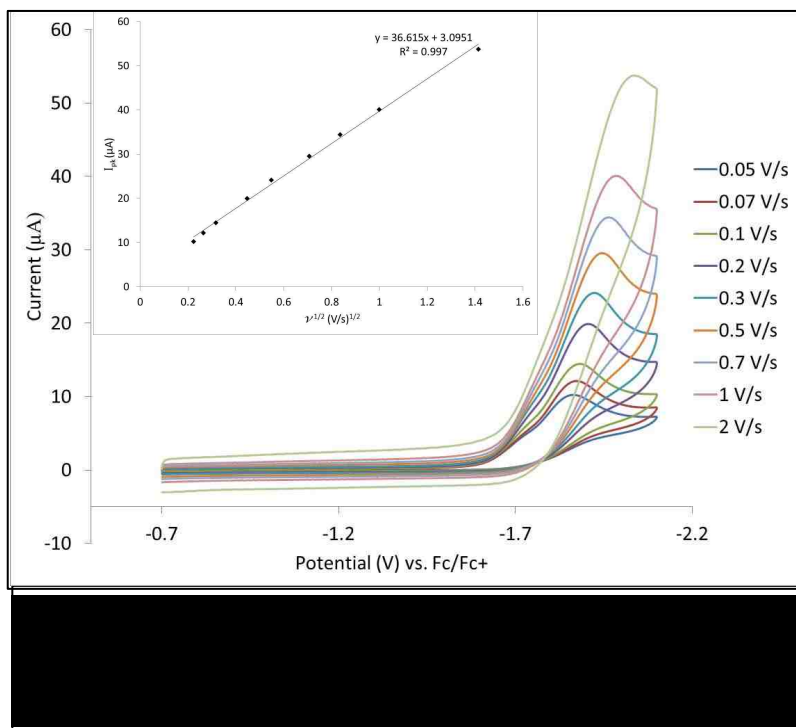


each compound demonstrates a diffusional reduction,⁸¹ and a structural change during reduction does not take place.⁸²

To determine whether CO₂ binds to the Zn-based

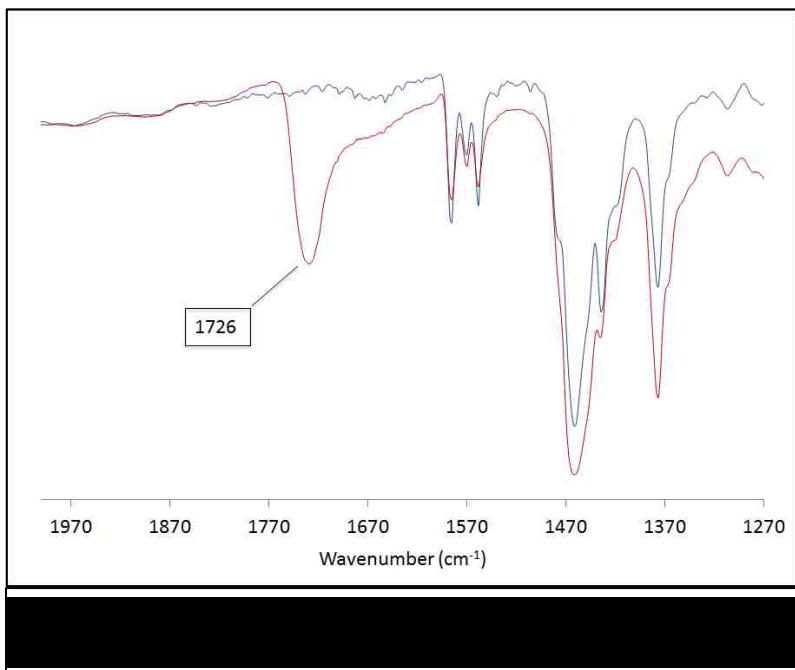
complexes, 0.2 M solutions of **25** and **26** in THF were subjected to bubbling CO₂.

The IR spectrum does not change for **26**, but a new stretch at 1726 cm⁻¹ does appear after 30 minutes of room temperature reaction time for **25**—see Figure



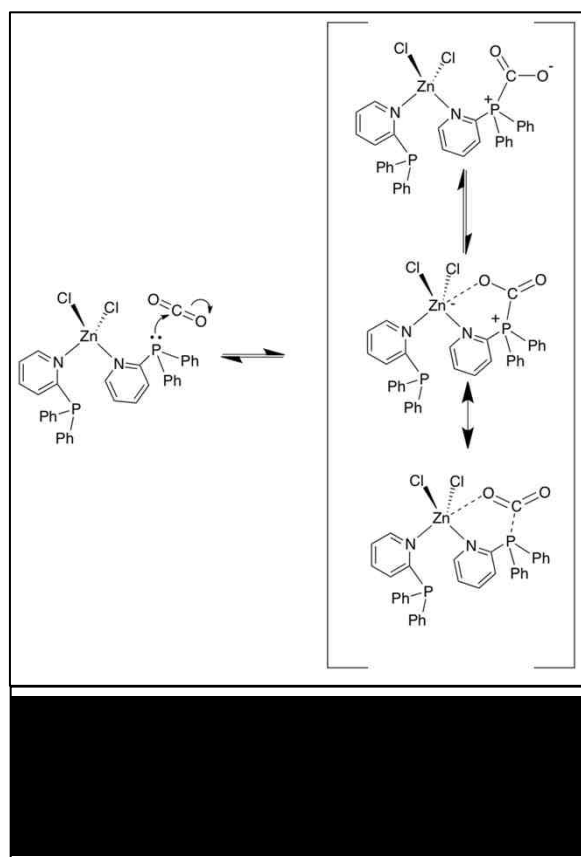
56. This is an important distinction between the Zn-based CO₂ complexes and the Group 4 metal-ligand complexes discussed in Chapter 2. The adduct-mediated CO₂

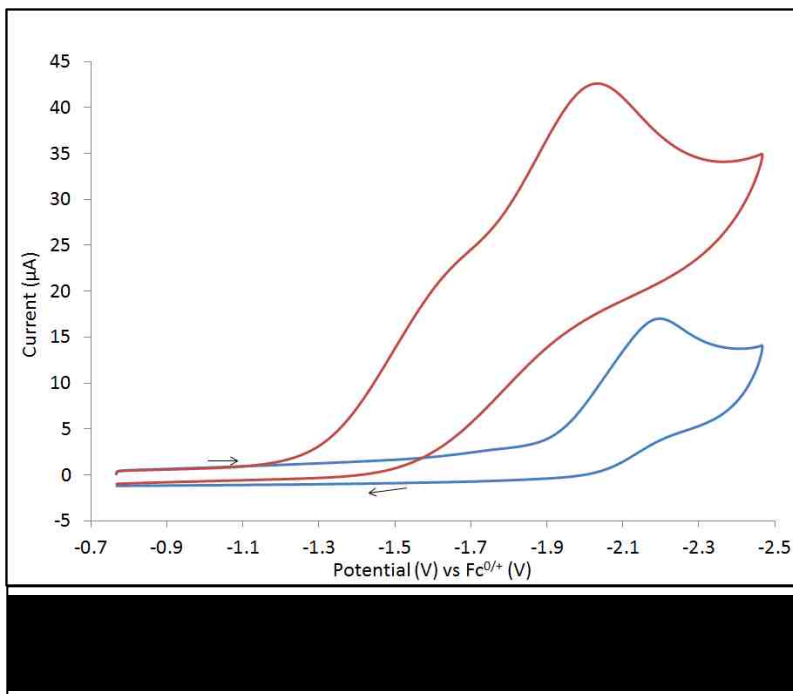
complexes were undetectable in IR due to the labile attachment and detachment of the gas molecule, but in **25**, the CO₂ persists through evaporation of the THF. Scheme 12



displays a variety of proposed resonance structures that can be described for **25-CO₂**.

Cyclic voltammetry was used to determine if **25** and **26** (despite the lack of observation of a CO₂ complex by IR spectroscopy) could appreciably decrease the overpotential for reducing CO₂. It can be observed from Figure 57 that **25** displays an anodic shift of about 0.6 V with the saturation of CO₂. Since it has already been shown that **25-CO₂** forms and is relatively stable, the

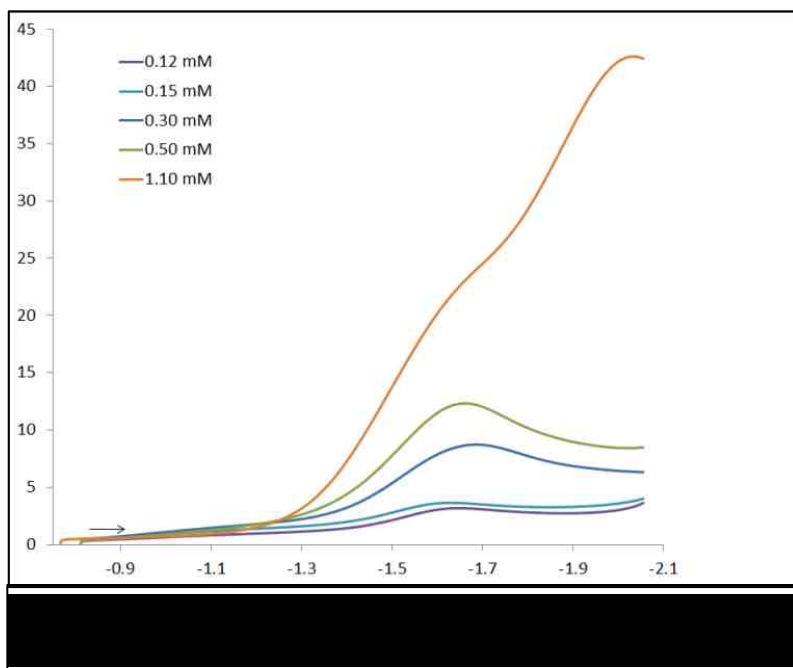




evidence shown here indicates that a common electrochemical reduction is occurring, *i.e.*, a charge transfer following a chemical reaction (CE mechanism – chemical first, electron transfer

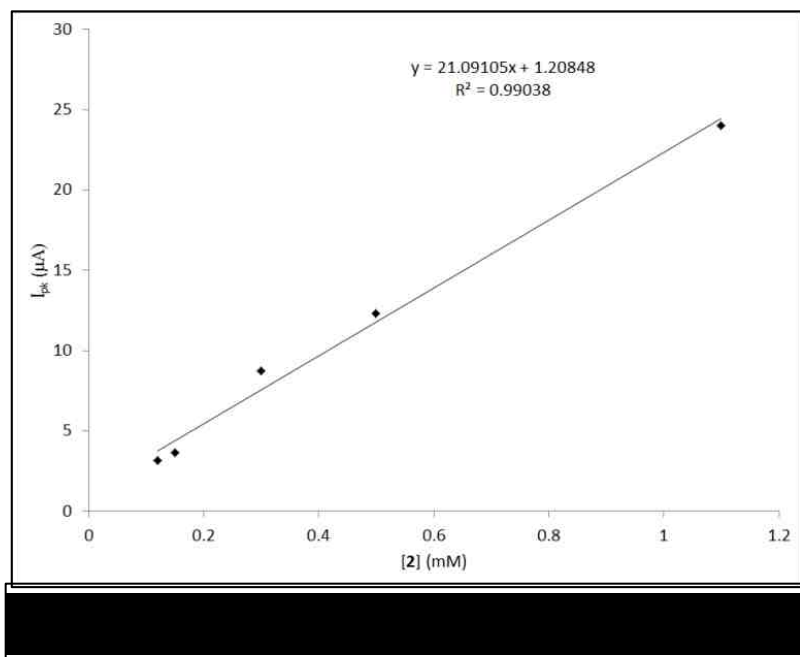
second). In this case, the reduction of CO₂ is proposed to yield CO as a product.

Since the peak current is directly correlated to reaction kinetics, different concentrations of **25** were tested in a CO₂-saturated environment using linear



sweep voltammetry (LSV). Even at very low concentrations of **25**, a reduction peak can still be observed (see Figure 58). At higher concentrations, the reduction peak

occurs only as a shoulder, suggesting that a competing electrochemical reaction may be occurring. This has not yet been investigated fully.

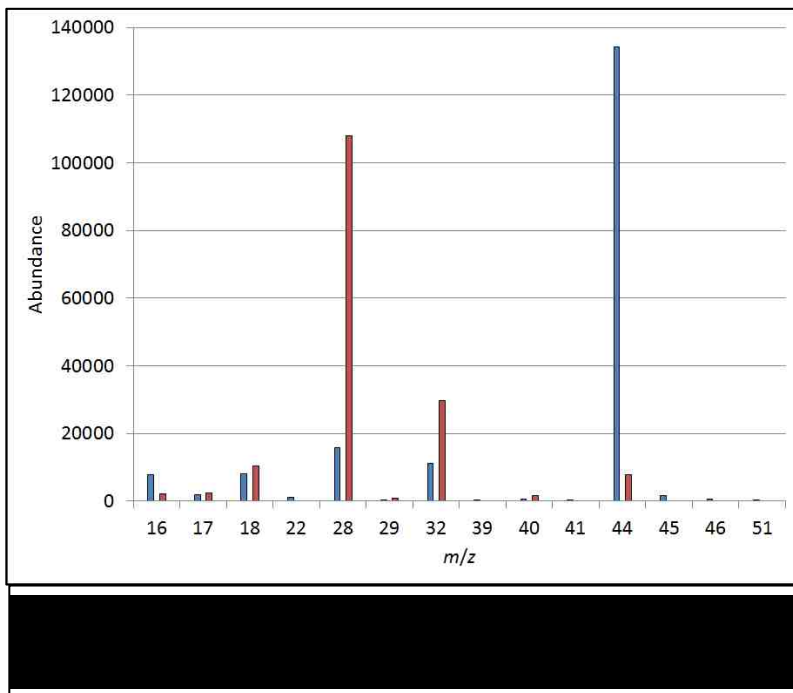


A plot of

concentration and peak height can also be taken into account to determine the order of the reaction. It can be observed from Figure 59 that the reduction of CO₂ is a first order reaction. The turnover frequency (TOF) was calculated⁸³ and was determined to be 96 s⁻¹ at 25°C and 1.0 atm CO₂.

Since it was proposed that **25** electrocatalytically reduces CO₂, controlled potential electrolysis (CPE) experiments were conducted. An approximately 1 mM solution of **25** was subjected to a CO₂-saturated environment at a potential of -1.80 V vs. Fc^{0/+} in 0.10 M Bu₄NPF₆ in THF. ³¹P NMR spectroscopy data were obtained before and after the electrolysis to ensure that **25** did not experience degradation during the reduction process. The identical spectra [³¹P NMR, THF, 121 MHz) δ 19.5 ppm] confirmed that **25** stayed intact throughout the entire experiment. Figure 60 displays the GC/MS data obtained from the headspace before and after the electrolysis. Before electrolysis, the dominant peak in the

headspace at 44 m/z is assigned to CO_2 , with 28 m/z assigned to the breakdown to CO as a result of ionization within the mass spectrometer. After the

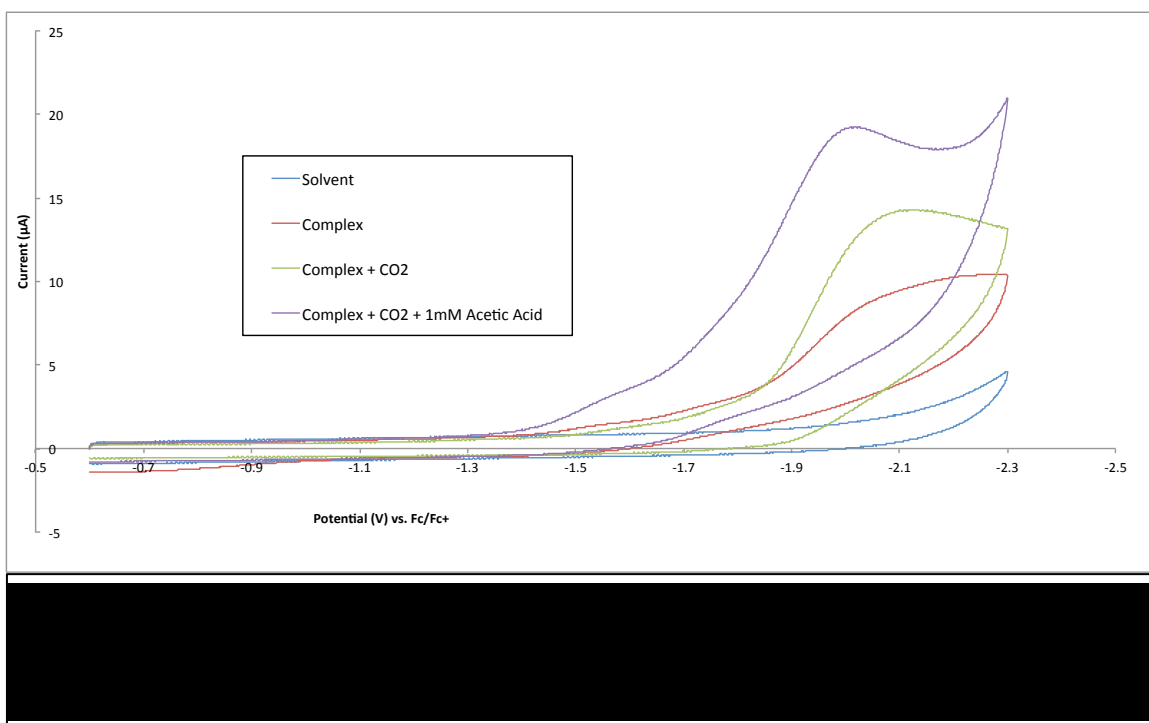


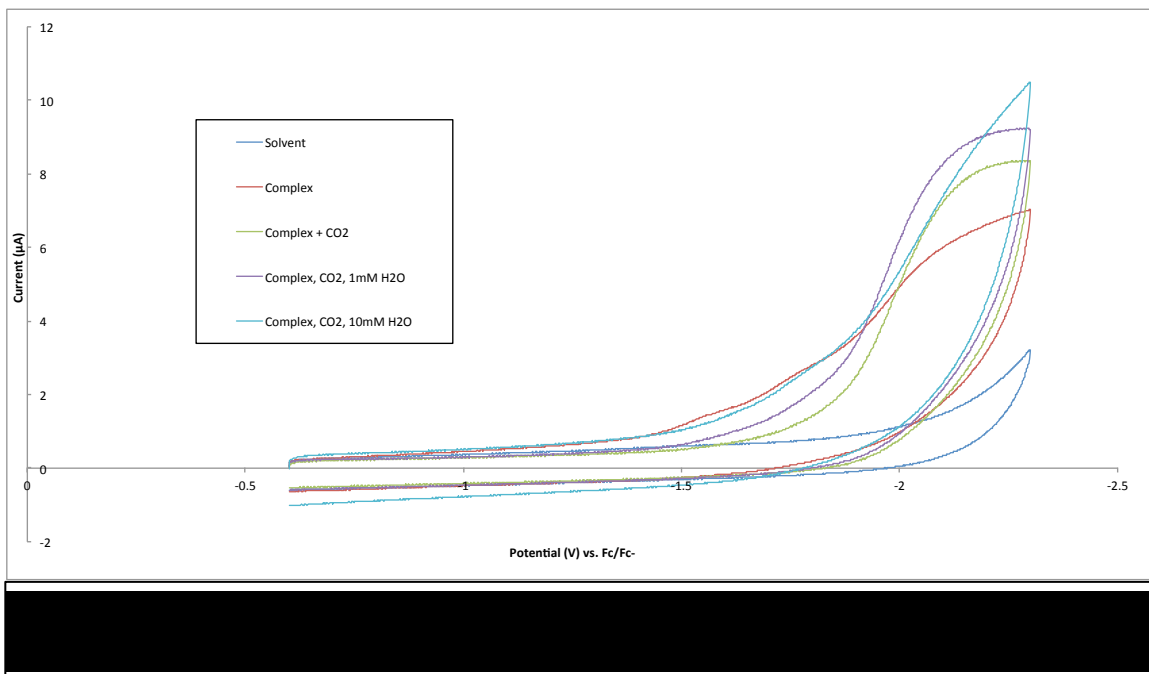
electrolysis, it can be clearly seen that the peak assigned at 44 m/z as CO_2 decreased significantly to near zero, while the peak at 28 m/z assigned as CO grew appreciably. N_2 contamination could be a source of

contamination in the sample, and since N_2 has the same atomic mass as CO, it needed to be ruled out as a possible contaminant. To ensure the peak at 28 m/z is in fact CO and not N_2 , the entire electrolysis experiment was performed in an Ar-filled glovebox, giving the identical result. This confirmed that the peak at 28 m/z is due to CO and not N_2 as there is no way for N_2 to contaminate the sample. The reduction of CO_2 to CO is a two-electron, two-proton process (see Table 1, pg. 5). There are no immediately available protons in the electrolysis cell, unless trace amounts of proton-containing compounds were present in the relatively hygroscopic THF. Acetic acid, a relatively weak acid, was used to determine if the presence of available free protons in solution increased the effectiveness of

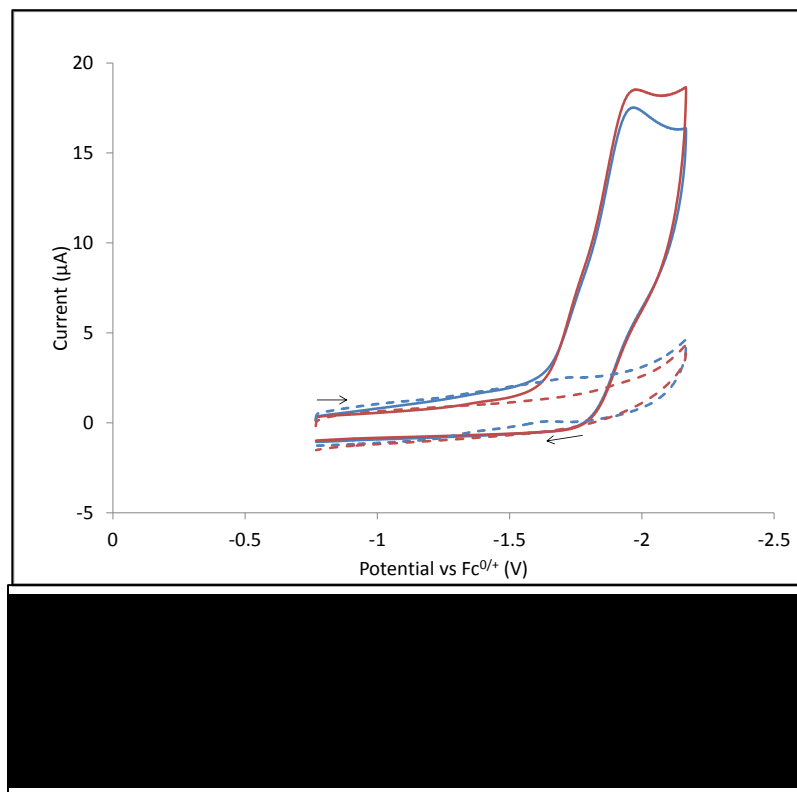
the catalyst—see Figure 61. It was found that the presence of acetic acid does increase the reduction of CO₂, indicating that an increased catalytic activity occurs with the introduction of protons. Serial additions of water were also tested to determine if catalytic activity would increase. Figure 62 displays the addition of 1 mM and 10 mM of water to the system. The addition of water did show a slight increase in reduction current, illustrating that even a weak proton source like water can enhance the catalytic activity of the complex. The reason water additions only increased the current slightly while the acetic acid increased more dramatically is because acetic acid is much more acidic, meaning its pK_a value is much lower than the pK_a of water.

Further investigations into the catalytic behavior of **25** will need to be initiated to determine the exact mechanism of the electrocatalysis. However, the electrocatalytic system developed here – one based on inexpensive earth-





abundant elements and acid-resistant ligands – can utilize available protons to drive the reduction of CO₂ to CO and presumably H₂O with a corresponding



decrease in overpotential of ~ 0.6 V using a glassy carbon electrode relative to the carbon electrode alone. As well, the onset of reduction of CO₂ has been shifted to a value essentially identical to a Pt electrode alone. This

is an extremely important finding as it validates our hypothesis that CO₂-adducts can facilitate the reduction of CO₂ to CO.

Compound **26** (see Figures 50 and 52) was also subjected to a saturated CO₂ environment under reductive conditions, as is illustrated in Figure 63. When CO₂ was added to complex **26**, a small increase toward the reduction of Zn²⁺ occurred. CO₂ did not reduce, and this was further evidenced by comparing the IR spectra before and after CO₂ introduction, with no new stretching frequencies.

3.4 Summary and Future Work

Initial findings show that **25** is the first organometallic Zn complex to facilitate the electrochemical reduction of CO₂ to CO. The overpotential was also shown to have been reduced by ~0.6 V, and this transformation occurred at the interface with a glassy carbon electrode rather than the more common Pt or Pd alternatives, which are more prevalent in electrocatalytic reductions of this type. Some questions remain unanswered, however, and future experiments will be required to explore the proton-donating sources for initial reduction of CO₂. More precise mass spectrometry instrumentation will be utilized to identify any other reduction products. However, this work is an important and critical proof of concept that the hypothesis stated earlier – that the “pre-bent” CO₂ adducts could be more easily reduced than CO₂ alone using main group complexes – is operative in this electrochemical system.

Chapter 4: Experimental

4.1 Ligand Syntheses:

All procedures were carried out in an Ar-filled dry box or by using standard Schlenk inert atmosphere techniques.⁸⁴ Solvents were dried using standard procedures prior to use. All reagents, including the ligand 2-diphenylphosphino-phenol (**3**), were purchased from commercial sources (Sigma Aldrich, Alfa Aesar, Acros Organics, or Gelest) and used without further purification. Multinuclear NMR spectral data were collected on a Bruker Avance III 300 MHz spectrometer. Infrared spectra were collected on a Bruker Vector 22 spectrometer using KBr plates. ALS Environmental in Tucson, Arizona, performed elemental analyses. All electrochemical analyses were conducted on a CH Instruments 660s Electrochemical Workstation.

2-^tBu₂P(C₆H₄)OH, 1

Step 1: This synthesis has been previously reported but only in small quantities using a Kugelrohr oven. 45 mL 1.6 M n-butyllithium (72 mmol) was added dropwise to a stirred solution of 13.41 g (72 mmol) 2-bromoanisole diluted to 75 mL with diethyl ether at 0°C. After two hours of stirring at 0°C, the solution turned orange. 12.94 g di-tert-butylchlorophosphine (72 mmol), diluted to 20 mL with diethyl ether, was then added dropwise to the cold, orange solution. As the

solution slowly warmed to room temperature, a precipitate formed. After three hours of stirring at room temperature, the orange, cloudy solution was filtered through Celite® filter aid, and the white filtrant was washed with 3x10 mL diethyl ether. Solvent was removed from the orange filtrate *in vacuo*, yielding an orange oil. The oil was distilled under dynamic vacuum at 110°C to yield a clear, colorless oil. This product is the phosphinoanisoole precursor to the final product. Yield: 16.30 g (64 mmol, 89%).

Step 2: 16.30 g (64 mmol) of the freshly-distilled phosphinoanisoole was diluted in 75 mL dichloromethane. Next, 140 mL 1.0 M BBr₃ (140 mmol, 2.3 eq.) was added dropwise to the colorless solution at -78°C. The solution turned dark red after stirring overnight at room temperature. The solvent was removed *in vacuo* to yield a dark red/brown viscous semisolid. Then, 30 mL methanol was added very slowly to eliminate any unreacted BBr₃—this is a highly exothermic reaction and great care and precaution should be taken. This brown solution stirred under reflux for five hours, eventually turning to a colorless slush-like solution. Then, 6.47 g triethylamine (NEt₃, 64 mmol) diluted in 50 mL diethyl ether was transferred via cannula, and the thick, white precipitate-containing solution stirred for an additional two hours at room temperature. All the volatiles were removed *in vacuo*, and the off-white solid was washed with benzene and filtered through Celite® filter aid. The colorless filtrate then had all volatiles removed again *in vacuo*, and the colorless oil was distilled at 95°C using a short column arm under

dynamic vacuum with hot water (~80°C) circulating through the cold arm. Yield: 12.50 g (53 mmol, 83%). ^1H (C_6D_6 , 300 MHz): δ 1.06 (d, $^3\text{J}_{\text{P-H}} = 12$ Hz, 18H, $\text{C}(\text{CH}_3)_3$), 4.25 (s, 1H, OH), 6.73 (t, $^3\text{J}_{\text{H-H}} = 7$ Hz, 1H, 5- C_6H_4), 7.11 (t, $^3\text{J}_{\text{H-H}} = 12$ Hz, 1H, 4- C_6D_6), 7.46 (d, $^3\text{J}_{\text{H-H}} = 8$ Hz, 1H, 3- C_6H_4), 8.11 (d, $^3\text{J}_{\text{H-H}} = 12$ Hz, 1H, 6- C_6H_4). $^{13}\text{C}\{^1\text{H}\}$ (C_6D_6 , 75 MHz) δ 30.3 (d, $^2\text{J}_{\text{P-C}} = 13$ Hz, $\text{C}(\text{CH}_3)_3$), 32.4 (d, $^1\text{J}_{\text{P-C}} = 14$ Hz, $\text{C}(\text{CH}_3)_3$), 115.5 (s, C_6H_4), 119.3 (s, C_6H_4), 131.8 (s, C_6H_4), 134.5 (s, C_6H_4). $^{31}\text{P}\{^1\text{H}\}$ (C_6D_6 , 121 MHz): δ -6.0 ppm. Anal. Calcd for $\text{C}_{14}\text{H}_{23}\text{OP}$: C, 70.56; H, 9.61. Found: C, 70.31; H, 9.61.

2-iPr₂P(C₆H₄)OH, 2

This compound was prepared in an analogous manner to **1** instead using chlorodiisopropylphosphine as the di-substituted chlorophosphine. At the conclusion of collecting the diisopropylphosphinoanisole (end of step 1), the clear, colorless oil distilled at 140°C with a yield of 84%. The clear, colorless oil was distilled under dynamic vacuum at 100°C with a cold arm temperature of 85°C. After the BBr_3 addition, the solution immediately turned colorless to bright red, and during two hours of stirring at room temperature, the color transitioned to yellow, eventually resulting in a viscous liquid after removing the volatiles. The dark yellow solution, after adding methanol, mimicked **4** in that it turned colorless after a five-hour reflux. The final distillation occurred at 130°C with a cold arm temperature of 85°C. Yield: 5.50 g (26 mmol, 72%). ^1H (C_6D_6 , 300 MHz): δ 0.87

(dq, $^2J_{\text{H-H}} = 29$ Hz, $^3J_{\text{H-H}} = 9.0$ Hz, 12H, CH₃), 1.86 (sept of d, $^2J_{\text{P-H}} = 3.6$ Hz, $^3J_{\text{H-H}} = 7.0$ Hz, 2H, CH(CH₃)₂), 3.28 (s, 1H, OH), 6.74-7.07 (m, 4H, C₆H₄). ¹³C{¹H} (C₆D₆, 75 MHz) δ 18.8 (d, $^2J_{\text{C-P}} = 8$ Hz, CH(CH₃)₂), 20.1 (d, $^1J_{\text{C-P}} = 18$ Hz, CH(CH₂)₃), 115.6 (s, C₆H₄), 118.6 (s, C₆H₄), 120.1 (s, C₆H₄), 131.4 (s, C₆H₄), 132.9 (s, C₆H₄), 162.1 (s, C₆H₄). ³¹P{¹H} (C₆D₆, 121 MHz): δ -23.6 ppm. Anal. Calcd for C₁₂H₁₉OP: C, 68.54; H, 9.59. Found: C, 67.76; H, 10.39.

2-^tBu₂P(C₆H₄)SH, **4**

This synthesis was performed with few variations to Barry *et al.*⁸⁵ 8.67 g thiophenol (79 mmol), diluted to 10 mL with cyclohexane, was added dropwise to a 0°C solution of 110 mL 1.6 M n-butyllithium (176 mmol, 2.25 eq.) and 20.57 g TMEDA (177 mmol, 2.25 eq.) in 25 mL cyclohexane. The solution stirred overnight, warming slowly to room temperature. The white precipitant was then filtered through Celite® filter aid and washed using three portions of 5 mL pentane and air-dried in an inert atmosphere for one hour. The white filtrant was dissolved in 50 mL THF, forming an orange solution. 11.37 g di-*tert*-butylchlorophosphine (63 mmol, 80 mol%) diluted in 5 mL THF was added to the orange solution dropwise at -78°C. The solution was allowed to warm to room temperature and stirred overnight, resulting in a red solution. This solution was acidified by the addition of 1.0 M H₂SO₄ to a pH of 6.5 at 0°C, forming a biphasic, yellow solution. THF was removed *in vacuo*, and the resulting aqueous solution

was washed three times with 30 mL diethyl ether. The yellow, ethereal layer was filtered through 5 g activated carbon and 5 g MgSO₄. All volatiles were removed *in vacuo* to yield a yellow sludge. The product was distilled from the crude oil under dynamic vacuum (ca. 20 mTorr, 100°C) and collected as a yellow oil.

Yield: 10.93 g (43 mmol, 68%). ¹H (CDCl₃, 300 MHz): δ 1.37 (d, ³J_{P-H} = 12 Hz, 18H, C(CH₃)₃), 5.70 (s, 1H, SH), 6.80-7.11 (m, 4H, C₆H₄). ¹³C{¹H} (C₆D₆, 75 MHz) δ 30.2 (d, ²J_{C-P} = 14.5 Hz, C(CH₃)₃), 32.6 (d, ¹J_{C-P} = 22 Hz, C(CH₃)₃), 123.6 (s, C₆H₄), 129.6 (s, C₆H₄), 135.4 (s, C₆H₄), 146.1 (s, C₆H₄), 146.8 (s, C₆H₄). ³¹P{¹H} (CDCl₃, 121 MHz): δ 18.9 ppm. Anal. Calcd for C₁₄H₂₃PS: C, 66.14; H, 9.12. Found: C, 65.88; H, 9.23.

2-iPr₂P(C₆H₄)SH, 5

This compound was prepared in an analogous manner to **1**.

Chlorodiisopropylphosphine was used as the disubstituted chlorophosphine, and there were no other changes to color or appearance. The final yellow oil was distilled under dynamic vacuum at 95°C. Yield: 6.22 g (27 mmol, 71%). ¹H (C₆D₆, 300 MHz): δ 0.94 (dquart, ²J_{H-H} = 43 Hz, ³J_{H-H} = 7.2 Hz, 12H, CH₃), 1.88 (sept of d, ²J_{P-H} = 2.4 Hz, ³J_{H-H} = 4.5 Hz, 2H, CH(CH₃)₂), 5.10 (s, 1H, SH), 6.84-7.11 (m, 4H, C₆H₄). ¹³C{¹H} (C₆D₆, 75 MHz) δ 19.3 (d, ²J_{C-P} = 10 Hz, CH(CH₃)₂), 24.4 (d, ¹J_{C-P} = 13 Hz, CH(CH₂)₃), 124.4 (s, C₆H₄), 129.2 (s, C₆H₄), 129.7 (s, C₆H₄), 132.7

(s, C₆H₄), 143.3 (s, C₆H₄), 143.7 (s, C₆H₄). ³¹P{¹H} (C₆D₆, 121 MHz): δ -2.4 ppm.
Anal. Calcd for C₁₂H₁₉PS: C, 63.69; H, 8.46. Found: C, 63.08; H, 8.69.

2-Ph₂P(C₆H₄)SH, 6

6 was synthesized using the same procedure as **4** and **5** with only a small variation at the product collection. Chlorodiphenylphosphine was used as the disubstituted chlorophosphine, and there were no other changes to color or appearance. After acidifying with 1.0 M H₂SO₄ and filtering through activated carbon and MgSO₄, all volatiles were removed *in vacuo* to yield an amber-colored crude solid mass. The yellow mass was dissolved in 50 mL ether, and as 150 mL of hexanes was added, a white precipitant fell out of solution. The off-white product was filtered over a glass frit and washed using 3x10 mL hexanes and then dried *in vacuo* overnight with a yield of 73%. ¹H (CDCl₃, 300 MHz): δ 4.18 (s, 1H, SH) 6.85-7.40 (m, aromatic). ¹³C{¹H} (C₆D₆, 75 MHz) δ 125.9-136.6 (s, aromatic region). ³¹P{¹H} (C₆D₆, 121 MHz): δ -12.2 ppm. Anal. Calcd for C₁₈H₁₅PS: C, 73.45; H, 5.14. Found: C, 72.81; H, 5.98.

4.2 Neutral Group 4 Metallocene Complexes

4.2.1 Titanocene Complexes

Cp₂TiMe₂

This complex was synthesized using the literature preparation.⁸⁶ 10.3 mL 1.6 M methyllithium (16.5 mmol) was added dropwise to a stirring slurry of 2.059 g dichlorotitanocene (8.25 mmol) at 0°C. The brown solution stirred at 0°C for 3 hrs, after which the solution was filtered through Celite® filter aid to yield an orange filtrate. All volatiles were removed from the orange solution to yield a dark orange solid. Immediately, 25.0 mL THF was added, due to the fact that unbound Cp₂Ti(CH₃)₂ decomposes readily. The red solution was stored in a freezer and was used before its suggested 30-day expiration. The purity was checked by ¹H NMR spectroscopy. Yield: 1.147 g (66%). ¹H (C₆D₆, 300 MHz): δ 0.06 (s, 6H, TiCH₃), 5.67 (s, 10H, C₅H₅).

Cp₂TiMe-O-C₆H₄P^tBu₂, 7

645 mg di-*tert*-butylphosphinophenol (2.9 mmol) was added to 2.9 mmol dimethyltitanocene in hexanes. The orange solution stirred overnight at room temperature, and an orange oil was obtained after removal of all volatiles *in vacuo*. The orange oil was redissolved in THF and then added to rapidly stirring

pentane. The solution was decanted, and the volatiles were removed *in vacuo*, leaving an orange emulsion. Yield: 40 mg (32%). ^1H (C_6D_6 , 300 MHz): δ 0.70 (s, 3H, TiCH_3), 1.32 (d, $^3\text{J}_{\text{P-H}} = 10$ Hz, 18H, $\text{C}(\text{CH}_3)_3$), 5.96 (s, 10H, C_5H_5), 6.53-7.47 (m, C_6H_4). $^{13}\text{C}\{^1\text{H}\}$ (C_6D_6 , 75 MHz) δ 30.2 (d, $\text{J}_{\text{C-P}} = 13$ Hz, TiCH_3), 31.0 (d, $^2\text{J}_{\text{C-P}} = 16$ Hz, $\text{C}(\text{CH}_3)_3$), 32.2 (d, $^1\text{J}_{\text{C-P}} = 14$ Hz, $\text{C}(\text{CH}_3)_3$), 113.2 (s, C_5H_5), 115.5 (s, C_6H_4), 116.4 (s, C_6H_4), 119.3 (s, C_6H_4), 131.8 (s, C_6H_4), 134.5 (s, C_6H_4), 162.3 (s, C_6H_4). $^{31}\text{P}\{^1\text{H}\}$ (C_6D_6 , 121 MHz): δ 12.8 ppm. Anal. Calcd for $\text{C}_{25}\text{H}_{35}\text{OPTi}$: C, 69.60; H, 8.17. Found: C, 69.61; H, 8.19.

*Cp*₂TiMe-O-C₆H₄Pi-Pr₂, **8**

242 mg diisopropylphosphinophenol (1.2 mmol) was added to 1.2 mmol dimethyltitanocene in 10 mL THF. After stirring overnight at room temperature, all volatiles were removed *in vacuo*, yielding an orange oil. Yield: 426 mg (88%). ^1H (C_6D_6 , 300 MHz): δ 0.64 (s, 3H, TiCH_3), 1.09 (dq, $^2\text{J}_{\text{H-H}} = 7$ Hz, $^3\text{J}_{\text{H-H}} = 11.5$ Hz, 12H, $\text{CH}(\text{CH}_3)_2$), 2.01 (sep., $^3\text{J}_{\text{H-H}} = 7$ Hz, 2H, $\text{CH}(\text{CH}_3)_2$), 5.96 (s, 10H, C_5H_5), 6.65-7.38 (m, 4H, C_6H_4). $^{13}\text{C}\{^1\text{H}\}$ (C_6D_6 , 75 MHz) δ 18.7 (d, $^2\text{J}_{\text{C-P}} = 7.5$ Hz, $\text{CH}(\text{CH}_3)_2$), 20.0 (d, $^1\text{J}_{\text{C-P}} = 13$ Hz, $\text{CH}(\text{CH}_3)_2$), 38.2 (s, TiCH_3), 113.4 (s, C_5H_5), 118.9 (s, C_6H_4), 120.0 (s, C_6H_4), 122.1 (s, C_6H_4), 130.0 (s, C_6H_4), 132.9 (s, C_6H_4), 173.7 (s, C_6H_4). $^{31}\text{P}\{^1\text{H}\}$ (C_6D_6 , 121 MHz): δ -8.8 ppm. Anal. Calcd for $\text{C}_{23}\text{H}_{31}\text{OPTi}$: C, 68.66; H, 7.77. Found: C, 67.91; H, 8.22.

Cp₂TiMe-O-C₆H₄PPh₂, **9**

321 mg 2-(hydroxyphenyl)-diphenylphosphine (1.2 mmol) was added piecewise to a 1.2 mmol dimethyltitanocene solution in THF. After stirring overnight, all volatiles were removed *in vacuo* yielding a dark orange solid. The orange solid was washed with cold hexane, and the supernatant was decanted. Yield: 330 mg (61%). ¹H (C₆D₆, 300 MHz): δ 0.85 (s, 3H, TiCH₃), 5.64 (s, 10H, C₅H₅), 6.5-7.8 (m, aromatic). ¹³C{¹H} (C₆D₆, 75 MHz) δ 38.5 (s, TiCH₃), 113.6 (s, C₅H₅), 115.6-138.3 (s, aromatic region). ³¹P{¹H} (C₆D₆, 121 MHz): δ -15.2 ppm. Anal. Calcd for C₂₉H₂₇OPTi: C, 71.05; H, 5.78. Found: C, 71.19; H, 6.37.

Cp₂TiMe-S-C₆H₄P^tBu₂, **10**

2.2 mmol dimethyltitanocene in THF was added to 553 mg of di-*tert*-butylphosphinothiophenol in 10 mL hexanes. The dark red solution stirred overnight, and then all volatiles were removed *in vacuo*, yielding a red oil. The red oil was subsequently redissolved in 10 mL THF and then added slowly to rapidly stirring pentane. The solution was decanted, and all volatiles were removed *in vacuo*, leaving a red emulsion. Yield: 105 mg (11%). ¹H (C₆D₆, 300 MHz): δ 0.21 (s, 3H, TiCH₃), 1.19 (d, ³J_{P-H} = 2.5 Hz, 18H, C(CH₃)₃), 5.78 (s, 10H, C₅H₅), 6.8-7.3 (m, 4H, C₆H₄). ¹³C{¹H} (C₆D₆, 75 MHz) δ 29.6 (s, TiCH₃), 30.3 (d, ²J_{C-P} = 14.5 Hz, C(CH₃)₃), 31.2 (d, ¹J_{C-P} = 15 Hz, C(CH₃)₃), 112.3 (s, C₅H₅), 113.2

(s, C₆H₄), 123.6 (s, C₆H₄), 125.9 (s, C₆H₄), 129.6 (s, C₆H₄), 135.4 (s, C₆H₄).

³¹P{¹H} (C₆D₆, 121 MHz): δ 22.1 ppm. Anal. Calcd for C₂₅H₃₅SPTi: C, 67.26; H, 7.90. Found: C, 67.74; H, 7.86.

*Cp*₂TiMe-S-C₆H₄Pi-Pr₂, **11**

1.2 mmol dimethyltitanocene was added to a solution of 261 mg 2-diisopropylphosphinothiophenol (1.2 mmol) in 5 mL THF. The red solution stirred at room temperature overnight. All volatiles were removed *in vacuo*, yielding a violet solid. Yield: 411 mg (82%). ¹H (C₆D₆, 300 MHz): δ 0.41 (s, 3H, TiCH₃), 1.11 (dd, ²J_{H-H} = 7 Hz, ³J_{H-H} = 4 Hz, 12H, CH(CH₃)₂), 2.07 (sep., ³J_{H-H} = 4 Hz, 2H, CH(CH₃)₂), 5.67 (s, 10H, C₅H₅), 6.97-7.31 (m, 4H, C₆H₄). ¹³C{¹H} (C₆D₆, 75 MHz) δ 19.6 (d, ²J_{P-C} = 8 Hz, CH(CH₃)₂), 20.7 (d, ¹J_{P-C} = 11 Hz, CH(CH₃)₂), 26.1 (s, TiCH₃), 112.4 (s, C₅H₅), 123.3 (s, C₆H₄), 128.5 (s, C₆H₄), 130.3 (s, C₆H₄), 133.2 (s, C₆H₄), 137.6 (s, C₆H₄). ³¹P{¹H} (C₆D₆, 121 MHz): δ -1.1 ppm. Anal. Calcd for C₂₃H₃₁PSTi: C, 66.02; H, 7.47. Found: C, 66.22; H, 8.03.

*Cp*₂TiMe-S-C₆H₄PPh₂, **12**

396 mg 2-(thiophenol)-diphenylphosphine (1.4 mmol) was added to a stirring solution of 1.4 mmol dimethyltitanocene in 10 mL THF. After stirring overnight at room temperature, all volatiles were removed *in vacuo*, yielding a red solid. The

red solid was washed with cold hexanes, and the supernatant was decanted.

Yield: 300 mg (46%). ^1H (Tol_{d8} , 300 MHz): δ 0.48 (s, 3H, TiCH_3), 5.67 (s, 10H, C_5H_5), 6.8-7.5 (m, aromatic). $^{13}\text{C}\{^1\text{H}\}$ (Tol_{d8} , 75 MHz) δ 41.0 (s, TiCH_3), 112.7 (s, C_5H_5), 115.7-139.3 (s, aromatic region). $^{31}\text{P}\{^1\text{H}\}$ (Tol_{d8} , 121 MHz): δ -11.5 ppm.
Anal. Calcd for $\text{C}_{29}\text{H}_{27}\text{PSTi}$: C, 71.61; H, 5.59. Found: C, 71.01; H, 6.00.

4.2.2 Zirconocene Species

Cp_2ZrMe_2

This complex was synthesized using the literature procedure.⁸⁷ 92.5 mL 1.6 M methylolithium (148 mmol) was added dropwise to 14.43 g dichlorozirconocene (49.4 mmol) in 150 mL ether at -78°C . During a three-hour stirring period, the colorless solution slowly warmed to room temperature. 5.37 g trimethylsilyl chloride (49.4 mmol), diluted in 25 mL ether, was added to the solution via cannula and stirred at room temperature for 1 hr. The solvent was removed *in vacuo*, and the product was then redissolved in 50 mL toluene. After filtering through Celite[®] filter aid, all the volatiles of the filtrate were removed *in vacuo*, yielding a white powder. Yield: 10.90 g (88%). ^1H (C_6D_6 , 300 MHz): 0.13 (s, 6H, ZrCH_3), 5.71 (s, 10H, C_5H_5).

Cp₂ZrMe-O-C₆H₄P^tBu₂, **13**

407 mg of 2-di-*tert*-butylphosphinophenol (1.7 mmol) was dissolved in 3 mL diethyl ether in a Schlenk flask. 431 mg dimethylzirconocene (1.7 mmol) was dissolved in 3 mL diethyl ether in a separate vial and then transferred to the clear, colorless ligand solution dropwise via pipette. Immediately, gas bubbles formed, and the solution stirred overnight at room temperature. The brown solid was washed with hexanes, and the supernatant was decanted. This process was repeated three times, eventually yielding a white powder after drying *in vacuo*. Yield: 562 mg (70%). ¹H (C₆D₆, 300 MHz): δ 0.57 (s, 3H, ZrCH₃), 1.23 (d, ³J_{P-H} = 11.5 Hz, 18H, C(CH₃)₃), 5.92 (s, 10H, C₅H₅), 6.56-7.62 (m, C₆H₄). ¹³C{¹H} (C₆D₆, 75 MHz) δ 30.1 (d, J_{C-P} = 9 Hz, ZrCH₃), 32.6 (d, ²J_{C-P} = 16.5 Hz, C(CH₃)₃), 40.0 (d, ¹J_{C-P} = 26 Hz, C(CH₃)₃), 111.6 (s, C₅H₅), 117.9 (s, C₆H₄), 119.7 (s, C₆H₄), 125.5 (s, C₆H₄), 130.3 (s, C₆H₄), 136.1 (s, C₆H₄), 169.9 (s, C₆H₄). ³¹P{¹H} (C₆D₆, 121 MHz): δ 9.9 ppm. Anal. Calcd for C₂₅H₃₅OPZr: C, 63.38; H, 7.45. Found: C, 62.70; H, 7.94.

Cp₂ZrMe-O-C₆H₄Pi-Pr₂, **14**

289 mg dimethylzirconocene (1.2 mmol) was dissolved in 5 mL hexanes in a Schlenk flask. In a separate weighing vial, 232 mg 2-diisopropylphosphinophenol (1.2 mmol) was dissolved in 1 mL hexanes and then transferred to the clear,

colorless zirconocene solution. After stirring overnight at room temperature, the yellow oil was collected after all volatiles were removed *in vacuo*. The yellow oil was washed with hexanes, and the supernatant was decanted. Yield: 317 mg (62%). ^1H (C_6D_6 , 300 MHz): δ 0.55 (s, 3H, ZrCH_3), 1.06 (dq, $^2\text{J}_{\text{H-H}} = 7$ Hz, $^3\text{J}_{\text{H-H}} = 11.5$ Hz, 12H, $\text{CH}(\text{CH}_3)_2$), 1.97 (sep., $^3\text{J}_{\text{H-H}} = 7$ Hz, 2H, $\text{CH}(\text{CH}_3)_2$), 5.89 (s, 10H, C_5H_5), 6.53-7.31 (m, 4H, C_6H_4). $^{13}\text{C}\{^1\text{H}\}$ (C_6D_6 , 75 MHz) δ 20.2 (d, $^2\text{J}_{\text{C-P}} = 9$ Hz, $\text{CH}(\text{CH}_3)_2$), 23.4 (d, $^1\text{J}_{\text{C-P}} = 13.7$ Hz, $\text{CH}(\text{CH}_2)_3$), 24.3 (s, ZrCH_3), 111.4 (s, C_5H_5), 113.8 (s, C_6H_4), 120.2 (s, C_6H_4), 123.1 (s, C_6H_4), 130.2 (s, C_6H_4), 133.2 (s, C_6H_4), 170.2 (s, C_6H_4). $^{31}\text{P}\{^1\text{H}\}$ (C_6D_6 , 121 MHz): δ -7.4 ppm. Anal. Calcd for $\text{C}_{23}\text{H}_{31}\text{OPZr}$: C, 61.98; H, 7.01. Found: C, 62.03; H, 7.36.

*Cp*₂ZrMe-O-C₆H₄PPh₂, **15**

76 mg dimethylzirconocene (0.3 mmol) was dissolved in 5 mL hexanes in a Schlenk flask. 84 mg 2-(hydroxyphenyl)-diphenylphosphine (0.3 mmol) was added piecewise to the clear, colorless solution due to its insolubility in hexanes. After stirring at room temperature overnight, the white slurry was filtered through Celite[®] filter aid. The solid was air-dried in an argon-filled glovebox for one hour. Yield: 73 mg (47%). ^1H (C_6D_6 , 300 MHz): δ -0.01 (s, 3H, ZrCH_3), 5.74 (s, 10H, C_5H_5), 6.1-7.8 (m, aromatic). $^{13}\text{C}\{^1\text{H}\}$ (C_6D_6 , 75 MHz) δ 40.1 (s, ZrCH_3), 115.2 (s, C_5H_5), 118.5-140.3 (s, aromatic region). $^{31}\text{P}\{^1\text{H}\}$ (C_6D_6 , 121 MHz): δ -16.7 ppm. Anal. Calcd for $\text{C}_{29}\text{H}_{27}\text{OPZr}$: C, 67.80; H, 6.03. Found: C, 66.32; H, 6.91.

Cp₂ZrMe-S-C₆H₄P^tBu₂, **16**

289 mg dimethylzirconocene (1.2 mmol) was dissolved in 3 mL toluene in a Schlenk flask. 292 mg 2-di-*tert*-butylphosphinothiophenol (1.2 mmol) was dissolved in 2 mL toluene in a separate weighing flask. The thiophosphine solution was transferred to the clear, colorless zirconocene solution via pipet. The solution stirred overnight at room temperature, and then all volatiles were removed *in vacuo* to yield a yellow wax. Yield: 502 mg (89%). ¹H (C₆D₆, 300 MHz): δ 0.10 (s, 3H, ZrCH₃), 1.13 (d, ³J_{P-H} = 2 Hz, 18H, C(CH₃)₃), 5.66 (s, 10H, C₅H₅), 6.9-7.4 (m, 4H, C₆H₄). ¹³C{¹H} (C₆D₆, 75 MHz) δ 28.1 (s, ZrCH₃), 31.1 (d, ²J_{C-P} = 15.5 Hz, C(CH₃)₃), 33.4 (d, ¹J_{C-P} = 28 Hz, C(CH₃)₃), 110.7 (s, C₅H₅), 112.6 (s, C₆H₄), 124.3 (s, C₆H₄), 125.6 (s, C₆H₄), 129.3 (s, C₆H₄), 138.6 (s, C₆H₄). ³¹P{¹H} (C₆D₆, 121 MHz): δ 23.3 ppm. Anal. Calcd for C₂₅H₃₅PSZr: C, 61.30; H, 7.20. Found: C, 61.21; H, 7.12.

Cp₂ZrMe-S-C₆H₄Pi-Pr₂, **17**

232 mg of 2-diisopropylphosphinothiophenol (1.0 mmol) was dissolved in 3 mL diethyl ether to form a clear, yellow solution. 258 mg dimethylzirconocene (1.0 mmol) was dissolved in 3 mL diethyl ether and transferred to the yellow solution. After stirring overnight, the yellow slurry was decanted, and the remaining yellow semi-solid was dried *in vacuo*. Yield: 322 mg (70%). ¹H (C₆D₆, 300 MHz): δ 0.16

(s, 3H, ZrCH₃), 1.12 (dd, ²J_{H-H} = 7 Hz, ³J_{H-H} = 5 Hz, 12H, CH(CH₃)₂), 2.36 (sep., ³J_{H-H} = 5 Hz, 2H, CH(CH₃)₂), 5.70 (s, 10H, C₅H₅), 6.86-7.51 (m, 4H, C₆H₄). ¹³C{¹H} (C₆D₆, 75 MHz) δ 18.6 (d, ²J_{P-C} = 8 Hz, CH(CH₃)₂), 19.6 (d, ¹J_{P-C} = 11 Hz, CH(CH₃)₂), 24.8 (s, CH₃), 109.8 (s, C₅H₅), 123.1 (s, C₆H₄), 128.4 (s, C₆H₄), 130.3 (s, C₆H₄), 133.2 (s, C₆H₄), 137.5 (s, C₆H₄). ³¹P{¹H} (C₆D₆, 121 MHz): δ 11.6 ppm. Anal. Calcd for C₂₃H₃₁PSZr: C, 59.83; H, 6.77. Found: C, 59.99; H, 6.87.

Cp₂ZrMe-S-C₆H₄PPh₂, **18**

289 mg dimethylzirconocene (1.2 mmol) was dissolved in 5 mL hexanes in a Schlenk flask. Then, 339 mg 2-(thiophenol)-diphenylphosphine (1.2 mmol) was added piecewise to the clear, colorless solution due to its insolubility in hexanes. The yellow solution stirred overnight at room temperature and then filtered through Celite® filter aid. The yellow solid was air-dried in an argon-filled glovebox and redissolved in toluene. Then, all volatiles were removed *in vacuo* to yield a yellow powder. Yield: 256 mg (42%). ¹H (C₆D₆, 300 MHz): δ 0.01 (s, 3H, ZrCH₃), 5.63 (s, 10H, C₅H₅), 6.7-7.2 (m, aromatic). ¹³C{¹H} (C₆D₆, 75 MHz) δ 1.3 (s, ZrCH₃), 110.0 (s, C₅H₅), 123.2-133.7 (s, aromatic region). ³¹P{¹H} (C₆D₆, 121 MHz): δ 16.5 ppm. Anal. Calcd for C₂₉H₂₇PSZr: C, 65.70; H, 5.14. Found: C, 65.97; H, 5.29.

4.2.3 Hafnocene Species

Cp_2HfMe_2

This complex was synthesized using an established synthesis from the literature.⁸⁸ 12 mL 3.0 M methylmagnesium chloride (36 mmol, 2.5 eq.) was added dropwise to a stirring suspension of 5.32 g dichlorohafnocene (14.1 mmol) and 125 mL ether at -78°C. The resulting brown solution stirred for one hour at room temperature. The grey slush was then treated with 7.46 g 1,4-dioxane (84.6 mmol) and stirred for an additional hour, eventually turning white. All volatiles were removed *in vacuo*, and the off-white solid was redissolved in toluene and filtered through Celite® filter aid. The solvent was removed from the yellow filtrate *in vacuo*, and the light yellow solid was triturated with 2 mL -35°C pentane. The resulting white solid was collected and dried *in vacuo* for 20 minutes. Yield: 4.10 g (86%). ¹H (C₆D₆, 300 MHz): 0.33 (s, 6H, HfCH₃), 5.62 (s, 10H, C₅H₅).

$Cp_2HfMe-O-C_6H_4P^tBu_2$, **19**

390 mg dimethylhafnocene (1.2 mmol) was deposited in 3 mL hexanes. 275 mg 2-di-*tert*-butylphosphenol (1.2 mmol) was dissolved in 2 mL hexanes in a separate vial and then transferred to the clear, colorless solution via pipet. The

solution stirred at room temperature for 48 hrs. All volatiles were then removed *in vacuo*, yielding a white powder. The white solid was washed with cold pentane, and the supernatant was decanted. Yield: 506 mg (78%). ^1H (C_6D_6 , 300 MHz): δ 0.47 (s, 3H, HfCH₃), 1.24 (d, $^3\text{J}_{\text{P-H}} = 11.5$ Hz, 18H, C(CH₃)₃), 5.86 (s, 10H, C₅H₅), 6.66-7.61 (m, C₆H₄). $^{13}\text{C}\{^1\text{H}\}$ (C_6D_6 , 75 MHz) δ 25.9 (d, $\text{J}_{\text{C-P}} = 6$ Hz, HfCH₃), 30.9 (d, $^2\text{J}_{\text{C-P}} = 16$ Hz, C(CH₃)₃), 32.4 (d, $^1\text{J}_{\text{C-P}} = 28$ Hz, C(CH₃)₃), 110.6 (s, C₅H₅), 112.0 (s, C₆H₄), 118.6 (s, C₆H₄), 120.2 (s, C₆H₄), 130.5 (s, C₆H₄), 136.0 (s, C₆H₄), 170.1 (s, C₆H₄). $^{31}\text{P}\{^1\text{H}\}$ (C_6D_6 , 121 MHz): δ 10.5 ppm. Anal. Calcd for C₂₅H₃₅HfOP: C, 53.52; H, 6.29. Found: C, 54.88; H, 6.93.

Cp₂HfMe-O-C₆H₄Pi-Pr₂, **20**

247 mg dimethylhafnocene (0.7 mmol) was deposited in 3 mL hexanes to form a white slurry. 151 mg 2-diisopropylphosphinophenol (0.7 mmol) was diluted in 1 mL hexanes in a separate weighing vial and then added to the white slurry via pipet. The solution stirred at room temperature for 48 hrs. The yellow slurry had all its volatiles removed *in vacuo*, yielding a yellow powder. The yellow solid was washed with cold pentane, and the supernatant was decanted. Yield: 238 mg (62%). ^1H (C_6D_6 , 300 MHz): δ 0.41 (s, 3H, HfCH₃), 1.07 (dq, $^2\text{J}_{\text{H-H}} = 7$ Hz, $^3\text{J}_{\text{H-H}} = 11.5$ Hz, 12H, CH(CH₃)₂), 1.97 (sep., $^3\text{J}_{\text{H-H}} = 7$ Hz, 2H, CH(CH₃)₂), 5.86 (s, 10H, C₅H₅), 6.52-7.26 (m, C₆H₄). $^{13}\text{C}\{^1\text{H}\}$ (C_6D_6 , 75 MHz) δ 20.0 (d, $^2\text{J}_{\text{C-P}} = 10$ Hz, CH(CH₃)₂), 23.4 (d, $^1\text{J}_{\text{C-P}} = 14$ Hz, CH(CH₃)₂), 25.7 (s, HfCH₃), 110.4 (s,

C₅H₅), 115.4 (s, C₆H₄), 119.3 (s, C₆H₄), 124.0 (s, C₆H₄), 130.1 (s, C₆H₄), 133.3 (s, C₆H₄), 169.7 (s, C₆H₄). ³¹P{¹H} (C₆D₆, 121 MHz): δ -8.1 ppm. Anal. Calcd for C₂₃H₃₁HfOP: C, 51.83; H, 5.86. Found: C, 52.33; H, 6.06.

Cp₂HfMe-O-C₆H₄PPh₂, 21

82 mg 2-(hydroxyphenyl)-diphenylphosphine (0.3 mmol) was transferred directly to a Schlenk flask, while 5 mL was added to create a white slurry. 100 mg dimethylhafnocene (0.3 mmol) was added to the flask directly, with no immediate change. 5 mL hexanes was added to dilute the slurry, and this solution stirred at room temperature for 48 hrs. All volatiles were removed *in vacuo*, yielding a white powder. The white powder was washed with cold pentane, and the supernatant was decanted. Yield: 117 mg (67%). ¹H (C₆D₆, 300 MHz): δ 0.01 (s, 3H, HfCH₃), 5.68 (s, 10H, C₅H₅), 6.4-7.5 (m, aromatic). ¹³C{¹H} (C₆D₆, 75 MHz) δ 41.2 (s, HfCH₃), 113.8 (s, C₅H₅), 117.9-141.2 (s, aromatic region). ³¹P{¹H} (C₆D₆, 121 MHz): δ -15.7 ppm. Anal. Calcd for C₂₉H₂₇HfOP: C, 57.96; H, 5.15. Found: C, 57.91; H, 4.98.

Cp₂HfMe-S-C₆H₄P^tBu₂, 22

390 mg dimethylhafnocene (1.2 mmol) was dissolved in 3 mL toluene to form a clear, yellow solution. 292 mg 2-di-*tert*-butylphosphinothiophenol (1.2 mmol) was

dissolved in 2 mL toluene and transferred to the yellow solution. After stirring at room temperature for 48 hrs., all volatiles were removed *in vacuo*, yielding a yellow wax. The wax was washed with cold pentane, and the supernatant was decanted. Yield: 374 (54%). ^1H (C_6D_6 , 300 MHz): δ 0.06 (s, 3H, HfCH₃), 1.04 (d, $^3\text{J}_{\text{P-H}} = 2$ Hz, 18H, C(CH₃)₃), 5.80 (s, 10H, C₅H₅), 6.9-7.6 (m, 4H, C₆H₄). $^{13}\text{C}\{^1\text{H}\}$ (C_6D_6 , 75 MHz) δ 25.0 (s, HfCH₃), 29.7 (d, $^2\text{J}_{\text{C-P}} = 13$ Hz, C(CH₃)₃), 32.1 (d, $^1\text{J}_{\text{C-P}} = 26$ Hz, C(CH₃)₃), 111.0 (s, C₅H₅), 112.1 (s, C₆H₄), 124.6 (s, C₆H₄), 125.7 (s, C₆H₄), 130.1 (s, C₆H₄), 138.9 (s, C₆H₄). $^{31}\text{P}\{^1\text{H}\}$ (C_6D_6 , 121 MHz): δ 23.5 ppm. Anal. Calcd for C₂₅H₃₅HfPS: C, 52.03; H, 6.11. Found: C, 51.49; H, 6.75.

Cp₂HfMe-S-C₆H₄Pi-Pr₂, **23**

390 mg dimethylhafnocene (1.2 mmol) was dissolved in 2 mL toluene in a Schlenk flask. 260 mg 2-di-isopropylphosphinothiophenol (1.2 mmol) was transferred to the flask, with several 1-mL toluene washes of the weighing vial. The clear, yellow solution stirred for three days. All volatiles were removed *in vacuo*, yielding a yellow oil that solidifies within a week. Yield: 645 mg (99%). ^1H (C_6D_6 , 300 MHz): δ 0.10 (s, 3H, HfCH₃), 1.00 (dd, $^2\text{J}_{\text{H-H}} = 7$ Hz, $^3\text{J}_{\text{H-H}} = 1$ Hz, 12H, CH(CH₃)₂), 2.10 (sept of d, $^2\text{J}_{\text{P-H}} = 4.2$ Hz, $^3\text{J}_{\text{H-H}} = 7$ Hz, 2H, CH(CH₃)₂), 5.66 (s, 10H, C₅H₅), 6.98-7.35 (m, 4H, C₆H₄). $^{13}\text{C}\{^1\text{H}\}$ (C_6D_6 , 75 MHz) δ 20.3 (d, $^2\text{J}_{\text{P-C}} = 14$ Hz, CH(CH₃)₂), 23.7 (d, $^1\text{J}_{\text{P-C}} = 16$ Hz, CH(CH₃)₂), 32.0 (s, CH₃), 110.0 (s, C₅H₅), 125.2 (s, C₆H₄), 131.9 (s, C₆H₄), 135.8 (s, C₆H₄), 140.1 (s, C₆H₄). $^{31}\text{P}\{^1\text{H}\}$

(C₆D₆, 121 MHz): δ 0.1 ppm. Anal. Calcd for C₂₃H₃₁HfPS: C, 50.32; H, 5.69.

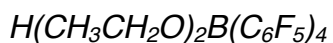
Found: C, 50.58; H, 5.89.

Cp₂HfMe-S-C₆H₄PPh₂, **24**

249 mg dimethylhafnocene (0.7 mmol) was dissolved in 2 mL hexanes. 213 mg 2-diisopropylphosphinothiophenol (0.7 mmol) was added directly to the white slurry. The yellow slurry was then diluted with an additional 2 mL hexanes, and it stirred at room temperature for 48 hrs. The solvent was removed *in vacuo*, yielding a yellow powder. Yield: 376 mg (82%). ¹H (C₆D₆, 300 MHz): δ -0.27 (s, 3H, HfCH₃), 5.86 (s, 10H, C₅H₅), 6.0-7.5 (m, aromatic). ¹³C{¹H} (C₆D₆, 75 MHz) δ 32.3 (s, HfCH₃), 110.0 (s, C₅H₅), 125.9-138.3 (s, aromatic region). ³¹P{¹H} (C₆D₆, 121 MHz): δ -9.6 ppm. Anal. Calcd for C₂₉H₂₇HfPS: C, 56.45; H, 4.41. Found: C, 55.98; H, 4.66.

4.3 Group 4 Metallocenium Complexes

NMR Spectral Data for [B(C₆F₅)₄]⁻, BArF Anion: ¹³C{¹H} (C₆D₆, 75 MHz): δ 130.1 (d, ¹J_{C-F} = 240 Hz, *m*-B(C₆F₅)₄), 133.3 (d, ¹J_{C-F} = 243 Hz, *p*-B(C₆F₅)₄), 169.8 (d, ¹J_{C-F} = 247 Hz, *o*-B(C₆F₅)₄). ¹¹B{H} (C₆D₆, 96 Hz): δ -13.9 (s). ¹⁹F (C₆D₆, 282 Hz): δ -131.7 (s, *o*-B(C₆F₅)₄), -162.5 (s, *p*-B(C₆F₅)₄), -166.1 (s, *m*-B(C₆F₅)₄).



16.375 g iodopentafluorobenzene (55.7 mmol) was dissolved in 150 mL diethyl ether and cooled in an iPrOH/N₂ bath. 61.3 mmol n-butyllithium (10% excess) was added dropwise to the clear, colorless solution, resulting in a light orange solution. The solution stirred cold for another 20 minutes, until the solution turns dark violet. 14 mmol BCl₃ (0.25 mol eq.) was then added dropwise to the cold solution, with no physical change. After stirring cold for 30 minutes, the violet solution was warmed to 0°C, resulting in the formation of a brown precipitant. 24 mmol HCl in diethyl ether was transferred via cannula to the brown solution, turning the solution to a lavender color. After stirring at room temperature overnight, the solution was beige-colored and was filtered over Celite® filter aid. The tangerine filtrate was reduced *in vacuo* until a solid began precipitating out of solution. The orange slush was filtered over Celite® filter aid and then washed 2 x 5 mL pentane. After air-drying, the white solid was washed with ether, forming an orange filtrate. The now-orange solution had all its volatiles removed *in vacuo*, leaving a light yellow powder. Yield: 10.158 g (87%). ¹H (CDCl₃, 300 MHz): δ 1.33 (t, ³J_{H-H} = 7.5 Hz), 6H, O-(CH₂CH₃)₂, 2.98 (q, ³J_{H-H} = 7.5 Hz, 4H, O-(CH₂CH₃)₂), 3.45 (s, 1H, H⁺).

2,6-di-tert-butylpyridinium(B(C₆F₅)₄)

213 mg di-*tert*-butylpyridine (DTBP, 1.1 mmol) and 837 mg H(CH₃CH₂O)₂B(C₆F₅)₄ (1.0 mmol) were combined with in 15 mL CH₂Cl₂ in a 50 mL Schlenk flask, stirring for two hours. The solution was transferred slowly to a flask with rapidly stirring hexanes, inducing precipitation of white microcrystals. The solution stirred vigorously for 15 minutes. The supernatant was decanted, and the solid was dried overnight *in vacuo*. Yield: 563 mg (59%). ¹H (C₆H₆, 300 MHz): δ 1.55 (s, 18H, CH₃), 7.85 (dd, 2H, ³J_{H-H} = 8 Hz, ³J_{H-H} = 2 Hz, *m*-H), 8.46 (t, 1H, ³J_{H-H} = 8 Hz, *p*-H), 11.01 (s, 1H, NH).

4.3.1 Titanocenium Complexes

Cp₂Ti-O-C₆H₄P^tBu₂⁺, 7⁺

732 mg DTBP BARF (0.84 mmol) was dissolved in 3 mL chlorobenzene and added dropwise to a solution of 362 mg **7** (0.84 mmol) in 3 mL chlorobenzene. The red solution quickly turned to a dark green color immediately after adding the BARF salt. After stirring overnight, all volatiles were removed *in vacuo*, yielding a dark green solid. The green solid was washed with pentane, and the supernatant was decanted. Yield: 651 mg (71%). ¹H (C₆D₆, 300 MHz): δ 1.34 (d, ³J_{P-H} = 11 Hz, 18H, C(CH₃)₃), 6.04 (s, 10H, C₅H₅), 6.66-7.31 (m, C₆H₄). ¹³C{¹H} (C₆D₆, 75

MHz) δ 32.3 (d, $^2J_{C-P} = 14$ Hz, $C(CH_3)_3$), 35.7 (d, $^1J_{C-P} = 11$ Hz, $C(CH_3)_3$), 113.6 (s, C_5H_5), 115.5 (s, C_6H_4), 116.1 (s, C_6H_4), 119.4 (s, C_6H_4), 132.0 (s, C_6H_4), 134.8 (s, C_6H_4), 161.9 (s, C_6H_4). $^{31}P\{^1H\}$ (C_6D_6 , 121 MHz): δ 38.1 ppm. Anal. Calcd for $C_{48}H_{32}BF_{20}OPTi$: C, 52.68; H, 2.95. Found: C, 52.49; H, 2.99.

Cp₂Ti-O-C₆H₄Pi-Pr₂⁺, 8⁺

1.037 g DTBP BARF (1.19 mmol) was dissolved in 5 mL fluorobenzene and added slowly to **8** in 5 mL fluorobenzene. After stirring overnight, all volatiles were removed, yielding an orange emulsion. The orange solid was washed with pentane, and the supernatant was decanted. Yield: 775 mg (61%). 1H (C_6D_6 , 300 MHz): δ 0.70 (dquart, $^2J_{H-H} = 5$ Hz, $^3J_{H-H} = 13$ Hz, 12H, $CH(CH_3)_2$), 1.81 (sep., $^3J_{H-H} = 5$ Hz, 2H, $CH(CH_3)_2$), 5.68 (s, 10H, C_5H_5), 6.28-7.44 (m, 4H, C_6H_4). $^{13}C\{^1H\}$ (C_6D_6 , 75 MHz) δ 19.3 (d, $^2J_{C-P} = 9$ Hz, $CH(CH_3)_2$), 21.0 (d, $^1J_{C-P} = 15$ Hz, $CH(CH_3)_2$), 113.5 (s, C_5H_5), 118.9 (s, C_6H_4), 120.2 (s, C_6H_4), 121.8 (s, C_6H_4), 130.4 (s, C_6H_4), 132.4 (s, C_6H_4), 174.1 (s, C_6H_4). $^{31}P\{^1H\}$ (C_6D_6 , 121 MHz): δ 74.3 ppm. Anal. Calcd for $C_{46}H_{28}BF_{20}OPTi$: C, 51.81; H, 2.65. Found: C, 53.12; H, 3.71.

$Cp_2Ti-O-C_6H_4PPh_2^+$, **9**⁺

131 mg DTBP BArF (0.15 mmol) was dissolved in 2 mL fluorobenzene and transferred dropwise to a solution of 71 mg **9** (0.15 mmol) in 1 mL fluorobenzene. The orange solution immediately turned to a dark brown color and stirred overnight at room temperature. The brown solution was added dropwise to 15 mL rapidly stirring hexanes. The supernatant turned amber-yellow, while a light brown solid precipitated out of solution. The solution was decanted, and the brown powder was dried *in vacuo*. Yield: 115 g (68%). ¹H (C₆D₆, 300 MHz): δ 5.56 (s, 10H, C₅H₅), 6.4-7.4 (m, aromatic). ¹³C{¹H} (C₆D₆, 75 MHz) δ 115.2 (s, C₅H₅), 118.5-137.9 (s, aromatic region). ³¹P{¹H} (C₆D₆, 121 MHz): δ 30.9 ppm. Anal. Calcd for C₅₂H₂₄BF₂₀OPTi: C, 55.06; H, 2.13. Found: C, 55.08; H, 2.12.

$Cp_2Ti-S-C_6H_4P^tBu_2^+$, **10**⁺

871 mg DTBP BArF (1.0 mmol) was dissolved in 3 mL chlorobenzene and transferred dropwise to a solution of 445 mg **10** in 1 mL chlorobenzene. Gas evolved immediately as the DTBP BArF solution was added to the dark yellow solution. After stirring overnight, the color of the solution changed to dark green. 10 mL hexanes was added slowly, until a green oil separates from the solution. The hexanes layer was decanted, and the green oil was dried *in vacuo* for one hour. Yield: 378 mg (34%). ¹H (CD₂Cl₂, 300 MHz): δ 1.22 (d, ³J_{P-H} = 4 Hz, 18H,

$C(CH_3)_3$, 6.26 (s, 10H, C_5H_5), 7.29-7.88 (m, 4H, C_6H_4). $^{13}C\{^1H\}$ (C_6D_6 , 75 MHz) δ 30.8 (d, $^2J_{C-P} = 16$ Hz, $C(CH_3)_3$), 32.0 (d, $^1J_{C-P} = 18$ Hz, $C(CH_3)_3$), 112.7 (s, C_5H_5), 113.2 (s, C_6H_4), 123.4 (s, C_6H_4), 126.1 (s, C_6H_4), 130.2 (s, C_6H_4), 136.0 (s, C_6H_4). $^{31}P\{^1H\}$ (C_6D_6 , 121 MHz): δ 84.4 ppm. Anal. Calcd for $C_{48}H_{32}BF_{20}PSTi$: C, 51.92; H, 2.90. Found: C, 51.02; H, 3.26.

Cp₂Ti-S-C₆H₄Pi-Pr₂⁺, **11⁺**

732 mg DTBP BArF (0.84 mmol) was slowly added to 363 mg **11** (0.84 mmol) in 3 mL chlorobenzene. The red solution quickly turned to a dark brown after immediately adding the BArF salt, but after stirring overnight at room temperature, the solution was olive green. Solvent was removed *in vacuo*, yielding a dark green solid. The green solid was washed with pentane, and the supernatant was decanted. Yield: 718 mg (79%). 1H (CD_2Cl_2 , 300 MHz): δ 1.14 (dd, $^2J_{H-H} = 6$ Hz, $^3J_{H-H} = 4$ Hz, 12H, $CH(CH_3)_2$), 2.34 (sep., $^3J_{H-H} = 4$ Hz, 2H, $CH(CH_3)_2$), 6.10 (s, 10H, C_5H_5), 7.31-7.47 (m, 4H, C_6H_4). $^{13}C\{^1H\}$ (C_6D_6 , 75 MHz) δ 18.9 (d, $^2J_{P-C} = 6$ Hz, $CH(CH_3)_2$), 20.8 (d, $^1J_{P-C} = 10$ Hz, $CH(CH_3)_2$), 26.1, 112.0 (s, C_5H_5), 124.1 (s, C_6H_4), 128.5 (s, C_6H_4), 130.2 (s, C_6H_4), 133.6 (s, C_6H_4), 137.5 (s, C_6H_4). $^{31}P\{^1H\}$ (CD_2Cl_2 , 121 MHz): δ 8.8 ppm. Anal. Calcd for $C_{46}H_{28}BF_{20}PSTi$: C, 51.04; H, 2.61. Found: C, 52.10; H, 2.08.

Cp₂Ti-S-C₆H₄PPh₂⁺, 12⁺

131 mg DTBP BArF (0.15 mmol) was dissolved in 5 mL chlorobenzene and transferred slowly to a solution of 75 mg **12** in 1 mL chlorobenzene. The dark red solution quickly changed to a forest green, and the solution stirred at room temperature overnight. All volatiles were removed *in vacuo*, yielding a dark green powder. The green powder was washed with pentane, and the supernatant was decanted. Yield: 126 mg (73%). ¹H (C₆D₆, 300 MHz): δ 5.48 (s, 10H, C₅H₅), 6.8-7.5 (m, aromatic). ¹³C{¹H} (C₆D₆, 75 MHz) δ 113.4 (s, C₅H₅), 115.6-139.1 (s, aromatic region). ³¹P{¹H} (C₆D₆, 121 MHz): δ 41.7 ppm. Anal. Calcd for C₅₂H₂₄BF₂₀PSTi: C, 54.29; H, 2.10. Found: C, 54.29; H, 2.12.

4.3.2 Zirconocenium Complexes

Cp₂Zr-O-C₆H₄P^tBu₂⁺, 13⁺

131 mg DTBP BArF (0.15 mmol) was slowly added to 71 mg **13** (0.15 mmol) in 5 mL fluorobenzene. The yellow solution stirred overnight at room temperature. Solvent was removed *in vacuo*, yielding a light brown solid. The brown solid was washed with hexanes, and the supernatant was decanted. The solid became light beige after drying *in vacuo*. Yield: 90 mg (53%). ¹H (C₆D₆, 300 MHz): δ 1.40 (d, ³J_{P-H} = 12 Hz, 18H, C(CH₃)₃), 6.13 (s, 10H, C₅H₅), 6.75-7.20 (m, C₆H₄).

$^{13}\text{C}\{^1\text{H}\}$ (C_6D_6 , 75 MHz) δ 33.8 (d, $^2J_{\text{C-P}} = 5$ Hz, $\text{C}(\text{CH}_3)_3$), 44.9 (d, $^1J_{\text{C-P}} = 11$ Hz, $\text{C}(\text{CH}_3)_3$), 121.1 (s, C_5H_5), 123.4 (s, C_6H_4), 130.0 (s, C_6H_4), 132.6 (s, C_6H_4), 133.8 (s, C_6H_4), 140.1 (s, C_6H_4), 166.7 (s, C_6H_4). $^{31}\text{P}\{^1\text{H}\}$ (C_6D_6 , 121 MHz): δ 23.5 ppm.
Anal. Calcd for $\text{C}_{48}\text{H}_{32}\text{BF}_{20}\text{OPZr}$: C, 50.67; H, 2.83. Found: C, 49.90; H, 3.09.

*Attempted preparation of $\text{Cp}_2\text{Zr-O-C}_6\text{H}_4\text{Pi-Pr}_2^+$, **14**⁺*

131 mg DTBP BArF (0.15 mmol) was added slowly to a solution of 67 mg **14** (0.15 mmol) and 5 mL fluorobenzene. The yellow solution stirred overnight. A yellow emulsion was left after removing all solvent *in vacuo*, but this desired product did not form cleanly as there were multiple ^{31}P peaks. Chlorobenzene was also used as a solvent, with no improvement in product conversion.

*$\text{Cp}_2\text{Zr-O-C}_6\text{H}_4\text{PPh}_2^+$, **15**⁺*

260 mg DTBP BArF (0.3 mmol) was solvated in 1 mL chlorobenzene before being added dropwise to a solution of 154 mg **15** (0.3 mmol) in 2 mL chlorobenzene. The clear, colorless solution immediately turned yellow. After stirring overnight, the yellow solution was added to 30 mL rapidly stirring hexanes, causing an immediate separation of a yellow oil. The solution was decanted and then dried *in vacuo*. Yield: 76 mg (21%). ^1H (C_6D_6 , 300 MHz): δ 5.90 (s, 10H, C_5H_5), 6.1-7.8 (m, aromatic). $^{13}\text{C}\{^1\text{H}\}$ (C_6D_6 , 75 MHz) δ 115.3 (s,

C₅H₅), 124.1-130.2 (s, aromatic region). ³¹P{¹H} (C₆D₆, 121 MHz): δ -23.54 ppm.

Anal. Calcd for C₅₂H₂₄BF₂₀OPZr: C, 53.03; H, 2.05. Found: C, 53.11; H, 2.00.

Attempted preparation of Cp₂Zr-S-C₆H₄P^tBu₂⁺, 16⁺

261 mg DTBP BARF (0.30 mmol) was added slowly to a solution of 147 mg **16** (0.30 mmol) in 5 mL fluorobenzene. After stirring overnight, the solvent was removed *in vacuo*, leaving a yellow emulsion. A variety of peaks appeared in the ³¹P NMR spectrum. Chlorobenzene was also used as a solvent, with no improvement in purity.

Cp₂Zr-S-C₆H₄Pi-Pr₂⁺, 17⁺

198 mg DTBP BARF (0.23 mmol) was dissolved in 3 mL chlorobenzene and added dropwise to a solution of 107 mg **17** in 3 mL chlorobenzene. The solution immediately turned from light yellow to orange/red. After stirring overnight, 25 mL hexanes was added slowly to the solution. A precipitous yellow layer formed on top of a transparent red layer. Once the two layers formed, the biphasic solution was stirred rigorously for several seconds. The solution formed a miscible, clear red solution. Red crystals form readily at the bottom and sides of the flask. Yield: 174 mg (67%). ¹H (C₆D₅Cl, 300 MHz): δ 1.11 (dd, ²J_{H-H} = 9 Hz, ³J_{H-H} = 4 Hz, 12H, CH(CH₃)₂), 2.34 (sep., ³J_{H-H} = 8 Hz, 2H, CH(CH₃)₂), 6.00 (s,

10H, C₅H₅), 6.14-7.42 (m, 4H, C₆H₄). ¹³C{¹H} (C₆D₅Cl, 75 MHz) δ 43.1 (d, ²J_{P-C} = 9 Hz, CH(CH₃)₂), 44.1 (d, ¹J_{P-C} = 13 Hz, CH(CH₃)₂), 103.3 (s, C₅H₅), 117.0 (s, C₆H₄), 118.7 (s, C₆H₄), 120.0 (s, C₆H₄), 121.0 (s, C₆H₄), 124.7 (s, C₆H₄). ³¹P{¹H} (C₆D₅Cl, 121 MHz): δ 39.9w ppm. Anal. Calcd for C₄₆H₂₈BF₂₀PSZr: C, 49.08; H, 2.51. Found: C, 49.40; H, 3.09.

Cp₂Zr-S-C₆H₄PPh₂⁺, 18⁺

131 mg DTBP BARF (0.15 mmol) was dissolved in 2 mL fluorobenzene and added dropwise to a solution of 79 mg **18** (0.15 mmol) in 2 mL fluorobenzene. The yellow solution stirred overnight without any physical change. All volatiles were removed *in vacuo*, yielding a yellow powder. The yellow powder was washed with hexanes, and the supernatant was decanted. Yield: 136 mg (76%). ¹H (C₆D₆, 300 MHz): δ 5.91 (s, 10H, C₅H₅), 6.6-7.2 (m, aromatic). ¹³C{¹H} (C₆D₆, 75 MHz) δ 109.8 (s, C₅H₅), 125.7-134.2 (s, aromatic region). ³¹P{¹H} (C₆D₆, 121 MHz): δ -12.0 ppm. Anal. Calcd for C₅₂H₂₄BF₂₀PSZr: C, 52.32; H, 2.03. Found: C, 51.09; H, 3.10.

4.3.3 Hafnocenium Complexes

$Cp_2Hf-O-C_6H_4P^tBu_2^+$, **19⁺**

65 mg DTBP BARF (0.075 mmol) was added slowly to 42 mg **19** (0.075 mmol) in 5 mL fluorobenzene, forming a yellow solution. After stirring for 48 hours, solvent was removed *in vacuo*, yielding a yellow semisolid. Yield: 81 mg (88%). 1H (C_6D_6 , 300 MHz): δ 1.39 (d, $^3J_{P-H} = 14$ Hz, 18H, $C(CH_3)_3$), 5.69 (s, 10H, C_5H_5), 6.74-6.91 (m, C_6H_4). $^{13}C\{^1H\}$ (C_6D_6 , 75 MHz) δ 30.3 (d, $^2J_{C-P} = 17$ Hz, $C(CH_3)_3$), 38.6 (d, $^1J_{C-P} = 26$ Hz, $C(CH_3)_3$), 110.3 (s, C_5H_5), 115.3 (s, C_6H_4), 118.6 (s, C_6H_4), 124.0 (s, C_6H_4), 130.2 (s, C_6H_4), 136.1 (s, C_6H_4), 168.8 (s, C_6H_4). $^{31}P\{^1H\}$ (C_6D_6 , 121 MHz): δ 23.4 ppm. Anal. Calcd for $C_{48}H_{32}BF_{20}HfOP$: C, 47.06; H, 2.63. Found: C, 47.43; H, 2.71.

$Cp_2Hf-O-C_6H_4Pi-Pr_2^+$, **20⁺**

This compound was prepared in an analogous manner to **19⁺**. Yield: 57 mg (64%). 1H (C_6D_6 , 300 MHz): δ 1.13 (dquart, $^2J_{H-H} = 6$ Hz, $^3J_{H-H} = 14$ Hz, 12H, $CH(CH_3)_2$), 1.97 (sep., $^3J_{H-H} = 6$ Hz, 2H, $CH(CH_3)_2$), 5.85 (s, 10H, C_5H_5), 6.74-7.15 (m, C_6H_4). $^{13}C\{^1H\}$ (C_6D_6 , 75 MHz) δ 19.9 (d, $^2J_{C-P} = 10$ Hz, $CH(CH_3)_2$), 23.6 (d, $^1J_{C-P} = 13$ Hz, $CH(CH_3)_2$), 110.4 (s, C_5H_5), 115.3 (s, C_6H_4), 119.5 (s, C_6H_4), 123.3 (s, C_6H_4), 131.0 (s, C_6H_4), 134.7 (s, C_6H_4), 169.8 (s, C_6H_4). $^{31}P\{^1H\}$ (C_6D_6 ,

121 MHz): δ 17.2 ppm. Anal. Calcd for $C_{46}H_{28}BF_{20}HfOP$: C, 46.16; H, 2.36.

Found: C, 46.88; H, 2.51.

Cp₂Hf-O-C₆H₄PPh₂⁺, 21⁺

65 mg DTBP BARF (0.075 mmol) was dissolved in 1 mL fluorobenzene and was added slowly to a solution of 45 mg **21** in 2 mL fluorobenzene. After stirring at room temperature for 48 hours, all the solvent was removed *in vacuo*, leaving a white powder. The white powder was washed with cold pentane and decanted.

Yield: 53 mg (56%). ¹H (C₆D₆, 300 MHz): δ 5.70 (s, 10H, C₅H₅), 6.3-7.5 (m, aromatic). ¹³C{¹H} (C₆D₆, 75 MHz) δ 113.9 (s, C₅H₅), 117.7-140.6 (s, aromatic region). ³¹P{¹H} (C₆D₆, 121 MHz): δ 9.4 ppm. Anal. Calcd for $C_{52}H_{24}BF_{20}HfOP$: C, 49.37; H, 1.91. Found: C, 49.10; H, 2.17.

Cp₂Hf-S-C₆H₄P^tBu₂⁺, 22⁺

65 mg DTBP BARF (0.075 mmol) was dissolved in 1 mL fluorobenzene and added dropwise to 43 mg **22** in 1 mL fluorobenzene. The yellow solution stirred for 48 hours at room temperature. Volatiles were removed *in vacuo*, yielding a yellow oil. Yield: 75 mg (81%). ¹H (C₆D₆, 300 MHz): δ 1.39 (d, ³J_{P-H} = 3 Hz, 18H, C(CH₃)₃), 5.82 (s, 10H, C₅H₅), 6.6-7.7 (m, 4H, C₆H₄). ¹³C{¹H} (C₆D₆, 75 MHz) δ 29.6 (d, ²J_{C-P} = 12 Hz, C(CH₃)₃), 36.4 (d, ¹J_{C-P} = 21 Hz, C(CH₃)₃), 119.8 (s, C₅H₅),

115.2 (s, C₆H₄), 124.0 (s, C₆H₄), 126.1 (s, C₆H₄), 130.1 (s, C₆H₄), 132.7 (s, C₆H₄).
³¹P{¹H} (C₆D₆, 121 MHz): δ 51.8 ppm. Anal. Calcd for C₄₈H₃₂BF₂₀HfPS: C, 46.45;
H, 2.60. Found: C, 48.17; H, 3.33.

Attempted preparation of Cp₂Hf-S-C₆H₄Pi-Pr₂⁺, 23⁺

65 mg DTBP BARF (0.075 mmol) was dissolved in 2 mL fluorobenzene and added dropwise to a solution of 42 mg **23** in 1 mL fluorobenzene. The yellow solution stirred for 48 hours. When the solvent was removed *in vacuo*, a yellow emulsion remained in the flask. ³¹P NMR proved that the product did not form as expected. Chlorobenzene was also attempted, but there was no improvement in purity.

Cp₂Hf-S-C₆H₄PPh₂⁺, 24⁺

131 mg DTBP BARF (0.15 mmol) was added slowly to 93 mg **24** in 5 mL fluorobenzene. After stirring at room temperature for 48 hours, solvent was removed *in vacuo*, yielding a yellow solid. The yellow solid was washed with cold pentane, and the supernatant was decanted. Yield: 147 mg (76%). ¹H (C₆D₆, 300 MHz): δ 6.01 (s, 10H, C₅H₅), 6.5-7.4 (m, aromatic). ¹³C{¹H} (C₆D₆, 75 MHz) δ 111.6 (s, C₅H₅), 130.3-137.8 (s, aromatic region). ³¹P{¹H} (C₆D₆, 121 MHz): δ -

12.0 ppm. Anal. Calcd for $C_{52}H_{24}BF_{20}HfPS$: C, 48.75; H, 1.89. Found: C, 50.30; H, 2.76.

4.4 Zn Complexes

Reactions were performed using an Ar (g) atmosphere glove box and standard Schlenk techniques. Solvents were purchased from Sigma Aldrich and dried using standard procedures prior to use. Reagents were purchased from Sigma Aldrich without further purification. Bis(2-pyridyl)phenylphosphine was prepared according to the method reported by Saucedo, *et. al.*⁸⁹ Multinuclear NMR spectral data were collected on a Bruker Avance III 300 MHz spectrometer. Infrared spectra were collected on a Bruker Vector 22 spectrometer using KBr plates. All electrochemical analyses were conducted on a CH Instruments 660s Electrochemical Workstation. GC/MS measurements were obtained using a Hewlett Packard 5890 Series II Plus Gas Chromatograph using He carrier gas on an Agilent J&W 20 m x 0.180 mm x 1.00 μ m DB-624 column observing the mass spectra of the eluent at 1.76 minutes with a Hewlett Packard 5972 Series Mass Selective Detector.

Dichloro[diphenyl-(2-pyridyl)phosphine-κ¹-N]zinc(II), **25**

259 mg ZnCl₂ (1.9 mmol) was dissolved in 10 mL THF and added dropwise to a colorless solution of diphenyl-2-pyridylphosphine (1.00 g, 3.8 mmol) in ca. 50 mL THF. The solution stirred for 45 minutes at room temperature, followed by removal of solvent *in vacuo* permitting collection of a white powder. Yield = 509 mg (40%). Colorless crystals suitable for single-crystal x-ray diffraction were grown from slow evaporation of CH₂Cl₂. ¹H NMR (CD₂Cl₂, 300 MHz): δ 7.19 (m, 8H, *m*-C₆H₅), 7.24-7.40 (overlapping multiplets, 14H, *o,p*-C₆H₅ and 6-C₆H₄N), 7.45 (m, 2H, 4-C₆H₄N), 7.77 (m, 2H, 5-C₆H₄N), 9.19(d, ³J_{H-H} = 5.0 Hz, 2H, 3-C₆H₄N). ¹³C{¹H} (CD₂Cl₂, 75 MHz): δ all aromatic C: 124.8 (s), 129.1 (d, J_{P-C} = 7.3 Hz), 129.8 (s), 131.2 (d, J_{P-C} = 7.8 Hz), 134.1 (d, J_{P-C} = 19 Hz), 134.8 (d, J_{P-C} = 5.2 Hz), 138.5 (s), 151.7 (d, J_{P-C} = 13 Hz), 163.2 (s). ³¹P{¹H} (CD₂Cl₂, 121 MHz) δ -5.8 ppm. Mp 176-178 °C.

Dichloro[phenyldi(2-pyridyl)phosphine-κ²-N,N']zinc(II)·0.5THF, **26**

89 mg ZnCl₂ (0.65 mmol) was dissolved in 5 mL THF and transferred dropwise to a gold, translucent solution of phenyldi(2-pyridyl)phosphine (162 mg, 0.65 mmol) in ca. 20 mL THF. After five minutes of rigorous stirring, a white precipitate formed in the yellow supernatant. After an additional 2 hrs. stirring at room temperature, the resulting white powder was then isolated by filtration and

washed with fresh THF (3 × 3 mL), and dried under vacuum for 1 hr. Yield = 191 mg (77%). Colorless single crystals were grown from a CH₂Cl₂/pentane mixture. ¹H NMR (CD₂Cl₂, 300 MHz): δ 1.82 (m, 2H, THF), 3.68 (m, 2H, THF), 7.19 (d, ³J_{H-H} = 8.2 Hz, 2H, 6-C₆H₄N), 7.52 (m, 2H, 5-C₆H₄N), 7.67 (m, 2H, 4-C₆H₄N), 7.72-7.87 (overlapping multiplets, 5H, C₆H₅), 9.00 (d, ³J_{H-H} = 5.3 Hz, 2H, 3-C₆H₄N). ¹³C{¹H} (CD₂Cl₂, 75 MHz): δ 25.9 (s, THF), 68.2 (s, THF), all aromatic C: 124.5 (d, J_{P-C} = 1.6 Hz), 128.7 (d, J_{P-C} = 11 Hz), 129.9 (d, J_{P-C} = 4.7 Hz), 130.8 (d, J_{P-C} = 9.9 Hz), 133.2 (d, J_{P-C} = 1.6 Hz), 138.6 (d, J_{P-C} = 25 Hz), 139.7, 150.7 (d, J_{P-C} = 4.6 Hz), 162.0 (d, J_{P-C} = 18 Hz). ³¹P{¹H} (CD₂Cl₂, 121 MHz) δ -5.2 ppm. Mp 269-271 °C.

4.4.1 Electrochemical Conditions and Analytical Methods.

A 3-electrode cell was used for all CV measurements with a 3 mm diameter glassy carbon working electrode. The auxiliary electrode was a coiled Pt wire and the reference electrode was a silver wire in 10 mM AgNO₃ in electrolyte solution contained in a fritted half-cell obtained from CH Instruments. Reported potentials are referenced to the ferrocene/ferrocenium redox couple that was measured at the conclusion of each experiment. Electrolyte solution was 0.10 M tetrabutylammonium hexafluorophosphate (Bu₄NPF₆) in 99.9% anhydrous inhibitor-free THF using electrochemical grade Bu₄NPF₆ from Sigma-Aldrich without further purification. The cell was purged of O₂ prior to each

experiment with the gas noted in the figures (CO₂ or Ar). The CO₂ (g) used in experiments was of research purity at 99.999% purchased from Matheson Trigas and passed through anhydrous CaSO₄ Drierite prior to use in all experiments.

The CPE experiments were conducted under pseudo-airtight conditions saturated with CO₂ (g) with vigorous stirring using a reticulated vitreous carbon working electrode, a coiled Pt wire contained in a fritted chamber (obtained from BAS Inc.), and the same reference electrode as used for CV measurements. An airtight syringe was used to measure the composition of the CPE headspace *via* mass spectrometry before applying a potential and after holding a potential of -1.80 V for 4 hours that lead to a plateau of residual current, indicating 99% completion of electrolysis.

4.4.2 Calculation of Turnover Frequency

The following equation was employed to report the TOF of 96 s⁻¹ for **25**.⁸³ Since the peak potential for the catalyst (i_p) is not equal to the peak potential for catalytic current (i_c), this TOF value should be interpreted as a gross approximation. Here, n is the number of electrons involved in each catalytic turnover, R is the universal gas constant, T is temperature, F is the Faraday constant, v is the scan rate, and k_{obs} is the observed rate constant reported as the turnover frequency, TOF.

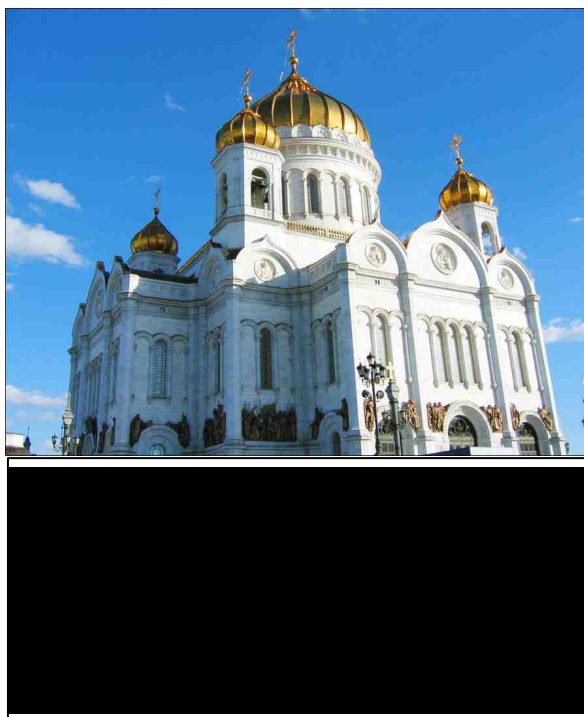
$$\frac{i_c}{i_p} = \frac{n}{0.4463} \sqrt{\frac{RTk_{obs}}{Fv}}$$

**PART II: Investigation of Organic-Based Reversible
Electrochemical Mirrors**

Chapter 1: Introduction

1.1 Electroplating: Societal and Industrial Role

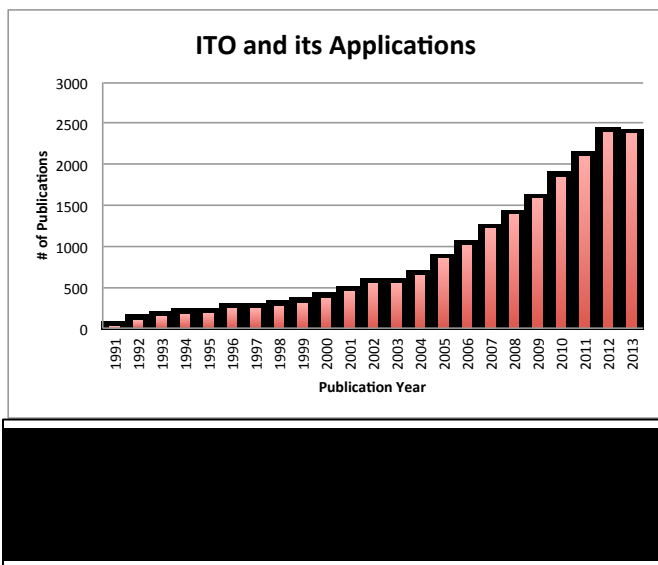
Electroplating, or the process of forming a coherent metal layer onto an electrode via an electric current, has been an active area of science since the early 1800s.⁹⁰ Historically, electroplating is the simple process of reducing metal cations under an electric field within an electrolyte solution. The metal cations are reduced at the working electrode—a conductive object connected to an electron source—and plating occurs uniformly on the object's conductive surfaces. Typically, the anode is made of the same material to be plated, *e.g.*, in copper plating, a copper rod would be submersed in the electrolyte solution, while the cathode is the object to be plated upon. This is known as a sacrificial electrode because the material will be consumed during reduction. One of the reasons why electroplating received scientific successes was due to the fact that there were many lucrative commercial avenues to pursue, so



funding became very easy to procure. A jeweler could sell a watch at an inflated price, simply because it had a desirable appearance, *e.g.*, gold or silver. The demand for gold and silver jewelry became so high that electrochemists would electroplate (or gild) anything that could conduct electricity: dinnerware, candlesticks, musical instruments, and religious symbols are just a few examples. Innovative Russian electrochemists, pioneered by Boris Jacobi (1801-1874), even gilded large bronze statues with precious metals. With personal financial assistance from Tsar Nicholas, Jacobi oversaw the largest electroplating facilities of the times, gilding enormous domes to fit atop the country's cathedrals and other architectural features for municipal buildings. Figure 64⁹¹ is an example of the many gold-plated domes found in Russia that were electroplated during this economic boom. During the late 1800s, electroplating was used for other purposes rather than decoration, and as properties of other metals began to be vetted out, metals like zinc (anti-oxidant), nickel (wear and corrosion protection), tin (corrosion protection in the food industry due to its nontoxicity), and chromium (corrosion protection with a decorative shine) were utilized for their special properties.⁹² Although the fundamental procedure of electroplating has changed very little, there are other techniques to adsorb material due to an electromotive force.

The impetus for modern electroplating was the advent of electronics, aviation, and space flight, and with these advances, scientists and engineers began to look for more finely tuned properties. In the mid to late 1980s,^{93,94}

electrochemists discovered how to migrate and manipulate suspended colloids capable of carrying charge (by use of an applied electric field), so dyes, ceramics, and polymers could also be deposited electrochemically onto a cathode. The term “electroplating” began to be phased out of the scientific community because of its history of metal-on-metal plating. “Electrophoretic deposition” is the term used today to describe the plating of any material onto a cathode as a response to an electric field, whether dissolved in electrolyte solution or dispersed.



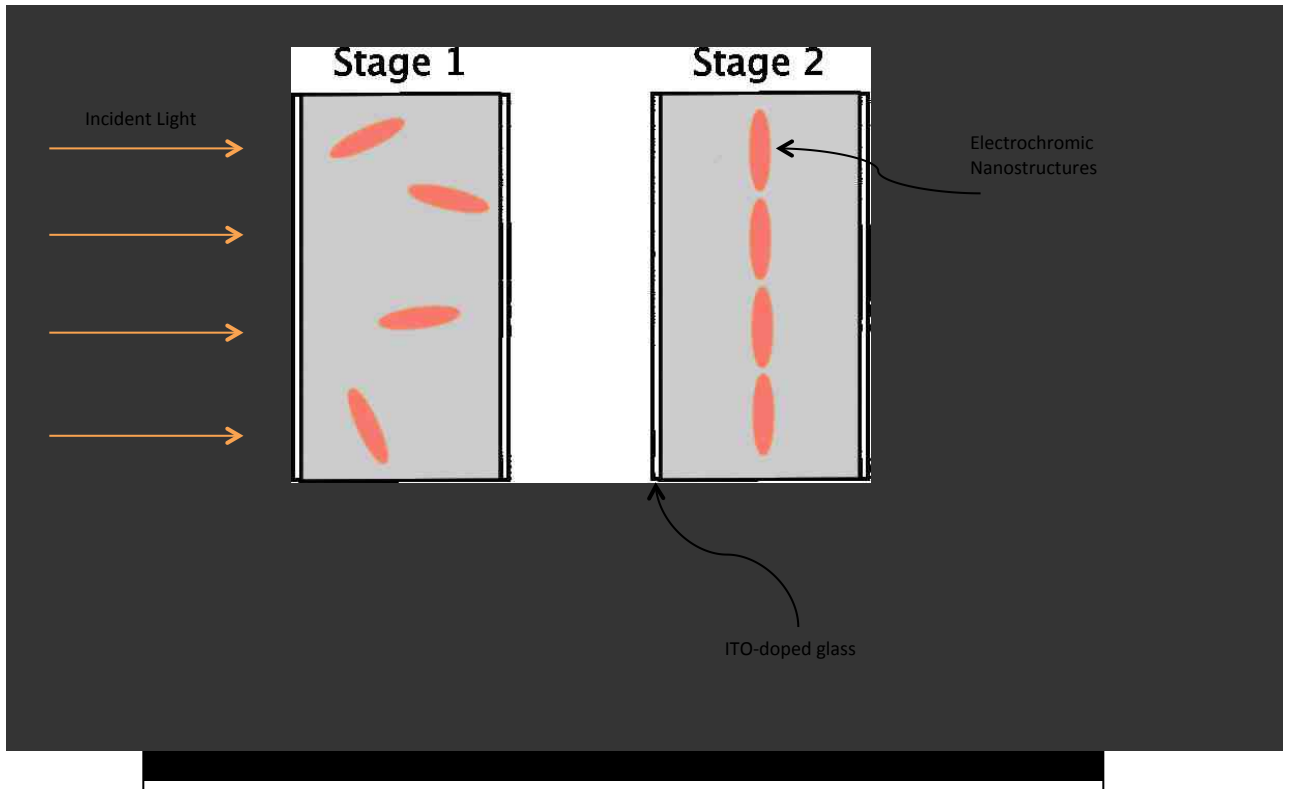
In the early 1990s, indium-tin oxide (ITO) and fluorine-doped tin oxide (FTO) began opening new doors in the field of electrophoretic deposition. ITO and FTO can be applied as nanometer-thick thin films that can be uniformly

applied to many surfaces, including glass.^{95, 96} A couple of the most exciting properties of these thin films is that they are transparent and conductive.⁹⁷ Once the properties of these transparent, conductive thin films were published in 1991, research in “smart” windows, LED screens, and solar cell technology began to explode. Figure 65 depicts this new-found interest by analyzing the number of publications in ITO advances since 1991.

1.2 Optical Modulation of Smart Windows

A smart window is a technology that allows the user to modulate optical properties of a window by way of inducing an electric field. Currently, within the commercial sector, opacity is the only property being modulated. Electrophoretic smart windows operate by utilizing two facing ITO-doped glass sheets separated by a thin liquid medium.⁹⁸ As a potential is created on one side of the glass, material is deposited onto the glass to create a desired effect. Metal oxides are most commonly used in today's smart window technology: vanadium,⁹⁹ tungsten,¹⁰⁰ zirconium,¹⁰¹ and lithium¹⁰² oxides are all being pursued in active research. A direct competitor with electrophoretic designs, however, is electrochromic smart window technology. Electrochromic devices can also modulate their optical properties through an induced electric field, but the chemistry within these devices is very different than the subtle and gradual deposition of electrophoretics. Electrochromic materials do not deposit material; rather, a crystal lattice of material is within a conductive medium sandwiched between two pieces of ITO-doped glass.¹⁰³ When an electric field is not present, the lattice is ordered or disordered in a specific manner, achieving a "stage 1" optical property. When a potential is applied to the material, the suspended crystals align with the field to form a "stage 2" optical property. Electrochromics change their optical properties very quickly, but current technology only allows for two stages of optical modulation. Research is currently being conducted to

create many layers of different crystalline lattices in order to accommodate many different optical modulations.¹⁰⁴ Figure 66 is an illustration of the more common two-stage window.



The advantage of an electrochromic window is fast responsivity, but there is a drawback if the user desires gradual modulation. An electrophoretic window, albeit much slower in achieving desired optical properties, can be fine-tuned to meet many different demands. Currently, smart windows are being utilized in office spaces, high speed trains, and public bathrooms that have a stage 1 transparent view and a stage 2 opaque view for privacy. Electrochromic devices are more desirable for high traffic areas that give the consumer an instant gratification of pushing a button and instantly observing a change in the window.

Electrophoretic devices are more suited for behind-the-scenes climate control and gradient optical modulation.

The interest and intrigue for electrochemical adaptive optics has many other applications outside of office buildings and public transportation. As well, NASA and other space entities are interested in smart window technology for their spacecraft. After initial tests, however, electrochromic devices were deemed unworthy for spaceflight due to the harsh environment in space. High-energy particles, micrometeoroids, and other dangers limit the scope of exterior smart windows, yet they are still viable for use within a manned hull for information displays and heads-up displays. Electrophoretic deposition devices are gaining in popularity for exterior smart glass technology in space due to its higher resilience and reparability.

1.3 Space Weather's Effects on Space Vehicle Components

1.3.1 Cosmic Rays

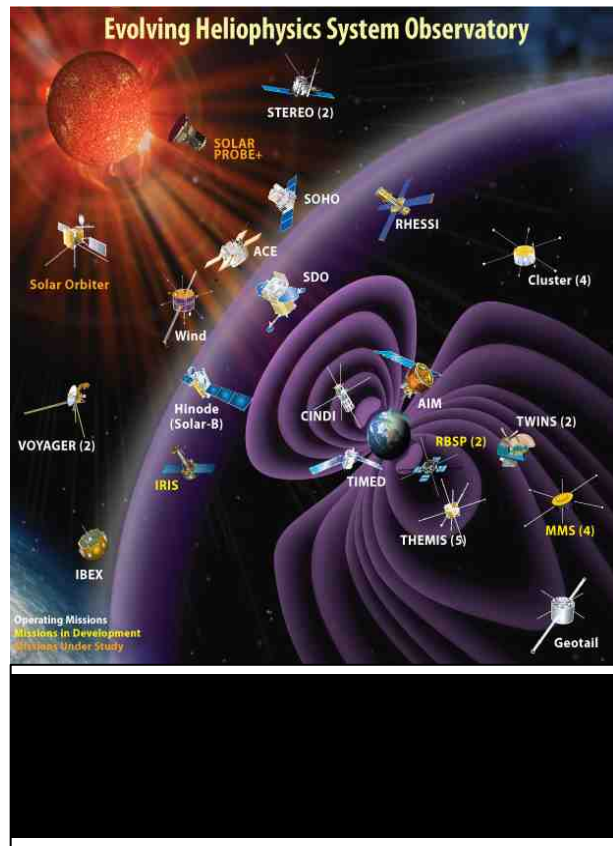
Cosmic rays are high-energy protons and atomic nuclei originating outside of our solar system,¹⁰⁵ which can have damaging effects on spacecraft, with little to no warning. For example, the Voyager 2 space probe malfunctioned in 2010 due to a flipped bit in the electronics system, deemed to be caused by a cosmic

ray interaction.¹⁰⁶ Cosmic rays are thought to be the greatest obstacle in long-distance manned space travel due to the lack of shielding technology.¹⁰⁷

Fortunately, many sources of cosmic rays are quasi-periodic,¹⁰⁸ but more research is needed for prediction, warning, and protection from interstellar cosmic rays. If an electrochromic smart window were infiltrated by one high-energy particle or electron, the entire system could fail since the optical modulation relies heavily on a consistent and reliable crystal lattice. Electrochromics rely on chemical and structural uniformity, but electrophoretics do not necessarily have to be chemically pure, as long as the impurity does not reduce or oxidize within the electrochemical window. Better detection and shielding will need to be implemented in order to defend against harmful cosmic rays.

1.3.2 Solar Events

Solar events range from the constant bombardment of solar radiation to the intense and sporadic coronal mass ejections. Much of the damaging radiation from the sun is blocked by the planet's atmosphere, but satellites



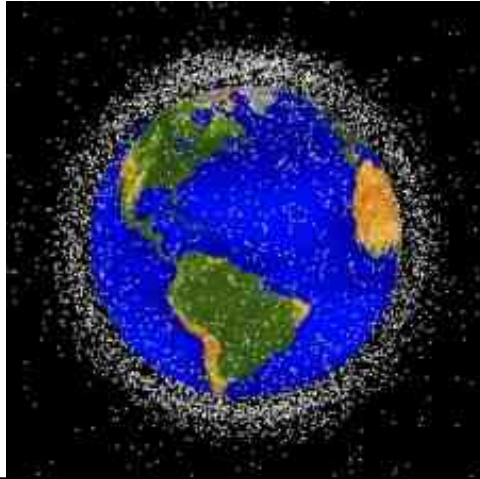
and other spacecraft need space hardening technology for the long-term exposure of radiation and to the bursts of extreme radiation during solar flares.¹⁰⁹ The most common discharges from the sun during a coronal mass ejection are electrons, protons, atomic elements like helium and oxygen, and high-energy magnetic fields. Fortunately, terrestrial and satellite warning systems are in place to give 6-10 minutes warning time of incoming solar flares (see Figure 67).¹¹⁰

Electrochromic devices, unless equipped with space environment hardening technology, would be unsuitable for space use. The crystalline structure is very sensitive, and any perturbations in electric fields due to the effects of incoming magnetic fields and high-energy particles can have disastrous consequences. This is one challenge for any new material or technology for space use because it is difficult to simulate and test all the particle and energy interactions that are possible in space. More research needs to be performed for space-worthy electrophoretic devices to determine how deposited vs. undeposited materials react under these environments, but electrophoretic devices will be a more promising technology as they can function in an impure environment.

1.3.3 Micrometeoroids and Space Debris

In addition to man-made objects, there are millions of micrometeoroids orbiting the earth, and although most are very small, multiple direct hits can be mission-altering. All these objects are travelling at velocities near 10 km/s

(22,000 mph)¹¹¹ and can cause



catastrophic damage to space vehicles and potential harm to astronauts. There are three classes of micrometeoroids: small (<1 cm), medium (diameter between 1 cm and 10 cm), and large (>10 cm). Small micrometeoroids do not pose much of a threat—at impact, their effect is much like sandblasting, although over a long period of time this can compromise a mission. Large micrometeoroids will certainly damage a satellite or other spacecraft, but these are easily detected and can be maneuvered around. The medium-sized micrometeoroids are actually the most dangerous because they are very difficult to detect, and they can penetrate many materials on a space vehicle. Figure 68 is an illustration of how much space debris can be determined by location (>10 cm or approximately the diameter of a softball).

Micrometeoroids and space debris impact is a problem for the entire space vehicle, not just for a space-ready smart window. However, very small

micrometeoroids could damage glass easily and then users would lose all functionality of the window. This is not the case for most other materials on the exterior of the spacecraft, with solar panels, imaging devices, and sensors being the exceptions. One advantage that electrophoretic devices may have over their electrochromic partners is that once a piece of glass is cracked by a micrometeoroid impact, an electrophoretic deposit of conductive material may be able to repair or cover the hole created by the debris, but this has yet to be tested.

1.4 Heat Transfer in Space

As humanity expands its horizons beyond planet Earth, new technologies and methods are required to accommodate the different environments presented in space. Not only do scientists and engineers have to look for ways to protect the spacecraft and astronauts from the devastating effects of space weather, they also need to rethink and retool for science experiments and everyday activities. For example, performing simple chemistry experiments in a zero gravity environment proves to be problematic when one is accustomed to the effects of gravity. Techniques such as filtration, extraction, and even stirring in a reaction flask are just three examples. Even beyond that, all aspects of life change drastically when one exits the atmosphere—heating and cooling have to

be reconfigured, bathrooms must be accommodating to zero gravity, and even eating and drinking become chores.

One very bulky, heavy, and expensive system that all space vehicles require is a heating and cooling system.¹¹² Thermal conduction (the collision of particles within proximity of each other) and convection (heat exchange in fluids and solids through diffusion and temperature gradients) are nearly non-existent in space due to the lack of matter, and so the only heating mechanism available is thermal radiation from the sun. When electromagnetic waves hit a space vehicle, the energy is either absorbed by the exterior of the vehicle or reflected back into space. The absorbed energy, in the form of heat, can then be transferred to the interior by means of convection through a series of heat pipes scattered throughout the space vehicle or, if an atmosphere exists inside the space vehicle, like the International Space Station, the energy can be transferred by the collision of the atmospheric molecules.¹¹³ All heat sources have to be calculated and configured within the spacecraft, *i.e.*, the sun, solar panels, and wiring, *etc.* External to these sources, there are heating and cooling systems in place to ensure optimal operating temperatures.

The cost of space vehicles can range into the dozens of millions of dollars upwards to several billion dollars, depending on their sophistication and scope of mission.¹¹⁴ The optimal operating temperature of any space vehicle is given as a range, depending on the systems on board. For example, hydrazine (N_2H_4), a very common space fuel for thrusters, freezes at $2^\circ C$ and boils at $114^\circ C$. The

circuitry within the space vehicle also has an optimal operating temperature range, usually much larger than the fuel (on the order of a few hundred degrees Celsius), but typically, the fuel reservoir and the circuitry for on-board operations are so far separated that independent heating systems have to be designed to keep each system within its optimal operating temperature. Aeronautical

Material	Thermal Conductivity (W/m ⁻¹ K ⁻¹)
Copper	386
Gold	315
Iron	80
Lead	35
Nickel	91
Silver	418
Titanium	19



engineers custom design each space vehicle for a precise heat balance.¹¹⁵

There are two types of heating systems for space vehicles: active and passive. Active heat systems are controlled by sensitive thermocouples in order to maintain the optimal operating temperatures within the vehicle.

One of the more sophisticated active heating systems on current space vehicles is louvers. Louvers are shutters with a series of adjustable slats fixed upon windows and heat pipes. Louvers may be adjusted to accommodate changes in heating environments, such as when a space vehicle enters or leaves daylight. Table 4¹¹⁶ shows a variety of metals used in louver design, but the reader should not assume this list to be an exhaustive toolkit for an aeronautical engineer. Other active heating systems, though less sophisticated than louvers, include

small heaters within the space vehicle (only usable in an atmosphere), or high resistance circuitry connected to heat pipes that can be closed in order to add heat to the system. Heaters and high-resistance wiring are undesired heating systems because their failure could result in spark emission, potentially causing more damage to surrounding systems. Passive systems include insulating blankets that keep heat from radiating into space and high-reflective material on the exterior of the vehicle to reduce solar absorption, though these are not adaptable. Once they are installed on a space vehicle, they cannot be adjusted or moved. Cooling systems are rare on unmanned space vehicles, simply because heat is constantly lost to the vacuum of space through radiation into the universe, but more care must be taken to maintain comfortable temperatures for astronauts on manned missions.

The methodology for heating space vehicles has not changed much since the dawn of the space race. Modern heating systems still utilize the basic principles used over 50 years ago, and now many aerospace companies are actively researching new and innovative methods to transfer heat within a space vehicle in an efficient and lightweight manner.

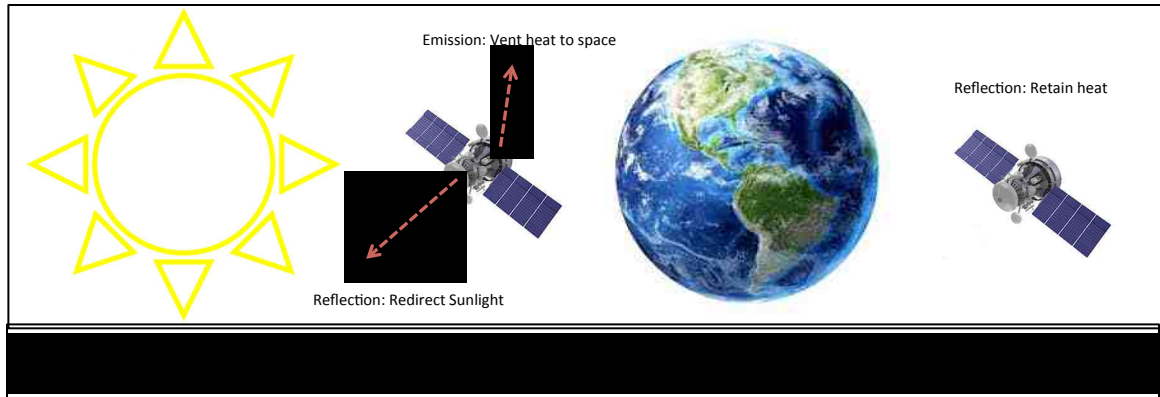
1.5 Electrophoretic Deposition in Fine-Tuning Thermal Control

Electrophoretic deposition of silver can produce a cohesive mirror, capable of reflecting a broad spectrum of electromagnetic energy.¹¹⁷ By installing silver

electrophoretic devices on the exterior of a spacecraft, these devices can be utilized to fine-tune IR radiation transmissivity by forming a well-ordered mirror. Electrophoretic mirror deposition is a better selection for thermal control than electrochromic devices because electrophoretics utilize a gradual deposition process, so as each layer is deposited, a thicker mirror is formed over time, rather than an “on” and “off” function in the electrochromic counterpart. This allows for selective attenuation and reflectivity so that operable temperatures can be tuned to the user’s need.

Electrophoretic devices can be a new viable option for aeronautical engineers with respect to thermal control on a space vehicle. When a space vehicle is in direct sunlight, electrophoretic windows can allow thermal radiation to enter. When heat is no longer desired to enter the space vehicle, electrophoretic deposition of silver can be enabled—this mirror will then reflect heat back into the universe, while also reflecting the thermal energy back into the space vehicle as an insulating force. While in earth shade, the mirror can be used to insulate the system, drastically reducing heat loss from the space vehicle, or the mirror could be turned off slowly if the space vehicle is too warm. When successful, this device will provide great utility to space entities due to reducing the cost, size, weight, and power requirements of all future space vehicles because many heavy and expensive heating techniques will be outdated. Figure 69 illustrates this concept. A three-stage electrophoretic device has been developed using an organic substrate;¹¹⁸ namely, black, transparent,

and mirror. This technology as-is would be inadequate for a space environment due to the volatility of the substrate; however, it provides a perfect test bed for proving the concept.



Based on the preceding introduction, our goals were to simulate an electrophoretic mirror using a bench-top electrochemical cell and test its viability in reflecting IR radiation and visible light. To prove the concept, a DMSO-based substrate was utilized due to its availability and cost. Transparent Indium-tin oxide conductors fused on silica glass were used as electrodes in order to simulate the transparent and mirror states of the device.

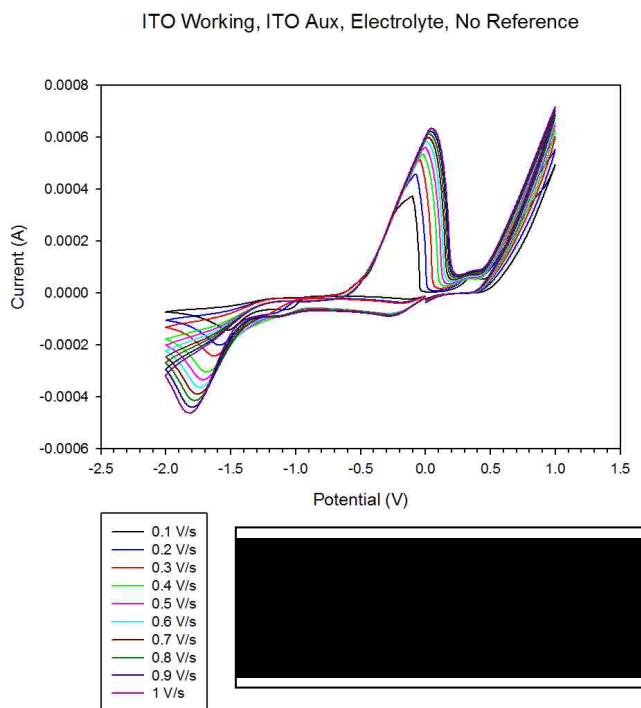
Chapter 2: Results and Discussion

2.1 Electrolyte Performance

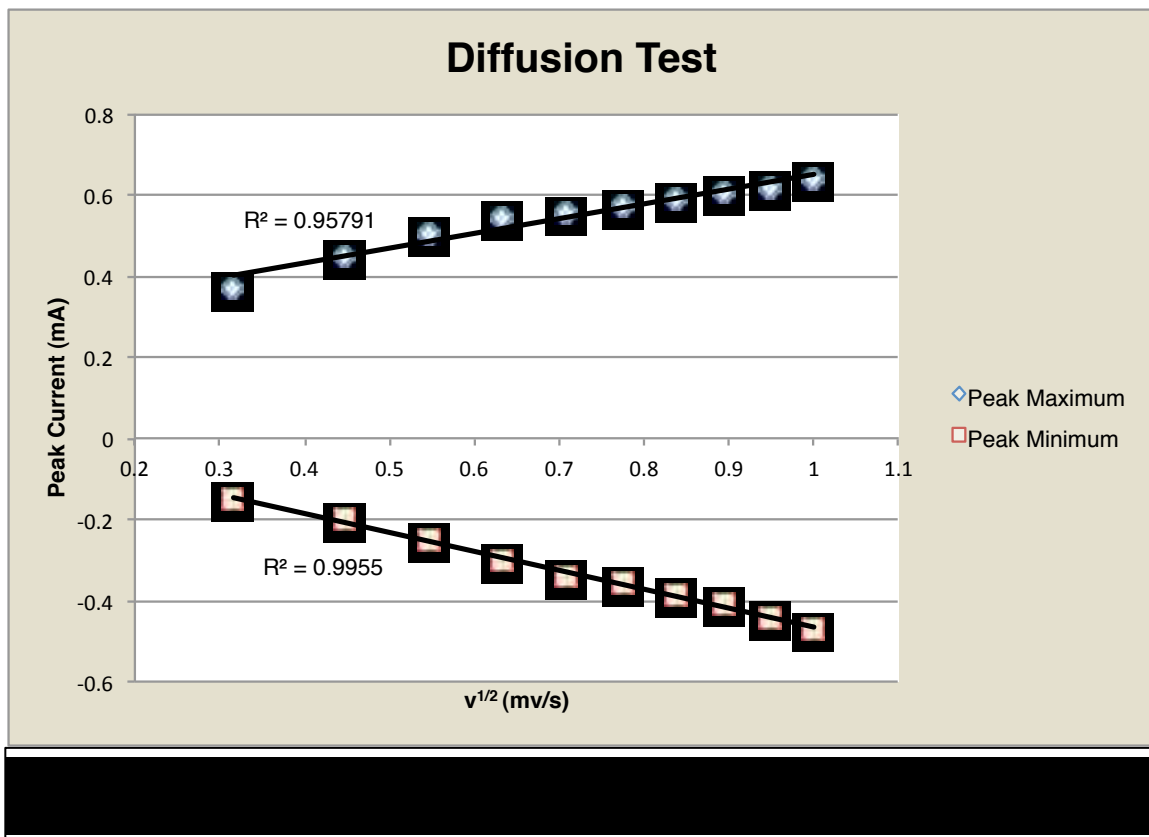
A standard three-electrode electrochemical cell was utilized to determine standard potentials of the various components of the electrolyte solution. ITO on glass was used as the working and counter electrodes. Using platinum is highly discouraged since it catalyzes a side-reaction during voltage ramps.

The standard electrolyte solution²⁹ composed of dimethyl sulfoxide (DMSO),

250 mM tetrabutylammonium bromide (TBABr), 50 mM silver nitrate, 10 mM copper chloride, and 10 wt% polyvinyl butyral (PVB). The flow of electrons is imperative in this cell, so TBABr is used because it is ionically separated in DMSO and it is non-reactive to any of the species in the solution. It was previously reported that copper co-deposits with the silver to aid in reversible deplating. The PVB forms a gel to make the electrolyte easier to use while



making the reversible electrochemical mirror (REM) device—the low viscosity of DMSO would make it very difficult to make the REM device without letting air bubbles get trapped during construction. In order to determine full reversibility of the plating and deplating of the mirror, cyclic voltammogram experiments were established with different ramping rates. Figure 70 displays the results of this test, ranging from 0.1 V/s to 1.0 V/s and Figure 71 illustrates the diffusion test derived from the Cottrell Equation,¹¹⁹ $D = \frac{i^2}{vn^3(FAc)^2}$. The Cottrell equation can be simplified to $i = kt^{1/2}$. A linear regression between $t^{1/2}$ and i delineates diffusion-controlled current, meaning that redox reactions occur so quickly that the reaction rate is equivalent to the diffusion rate. A nonlinear regression would indicate other rate-limiting steps involved in the reaction, *e.g.*, association or dissociation

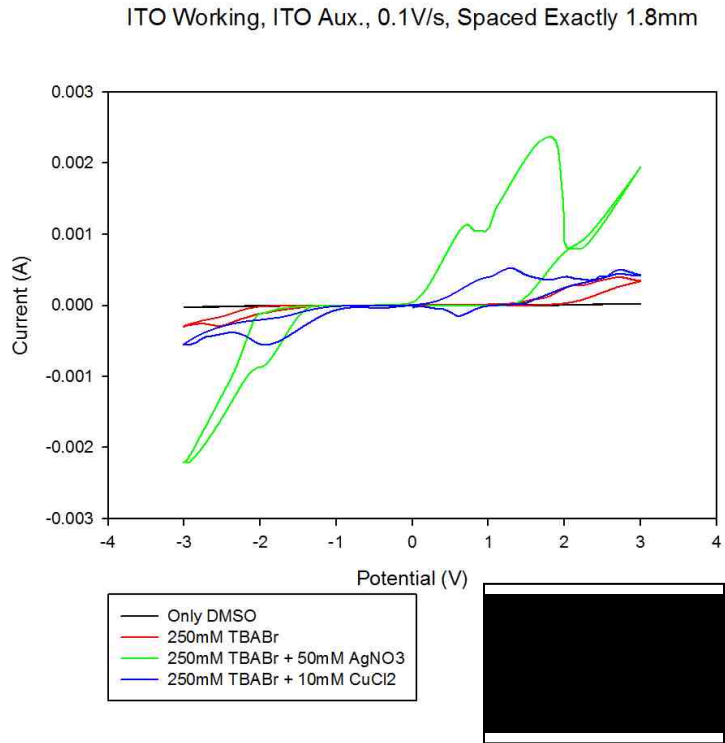


of a ligand or a change in geometry.¹²⁰

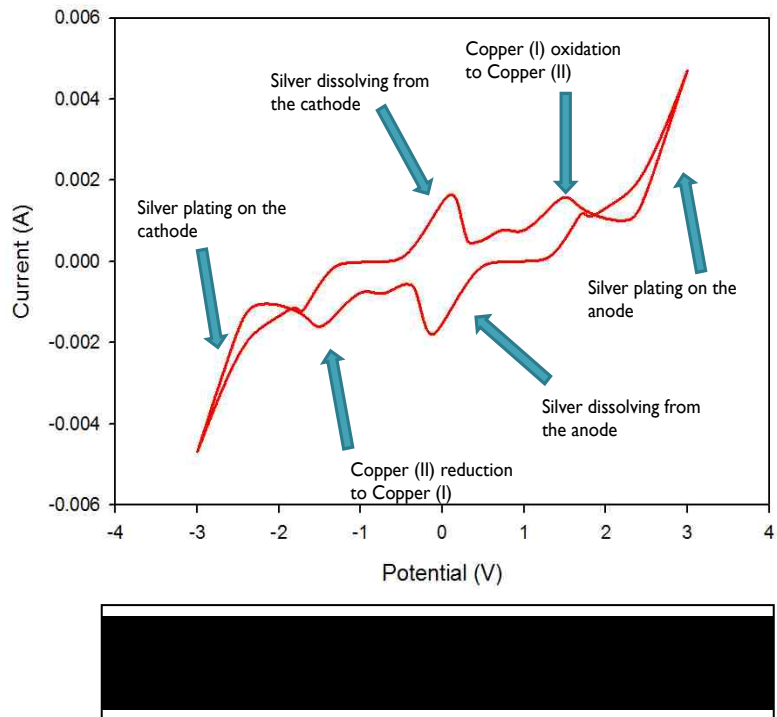
Next, the electrochemical window needed to be established, in tandem with isolating each component of the electrolyte solution.

Araki²⁹ *et al.* used an electrochemical window from -2.0 V to 1.0V.

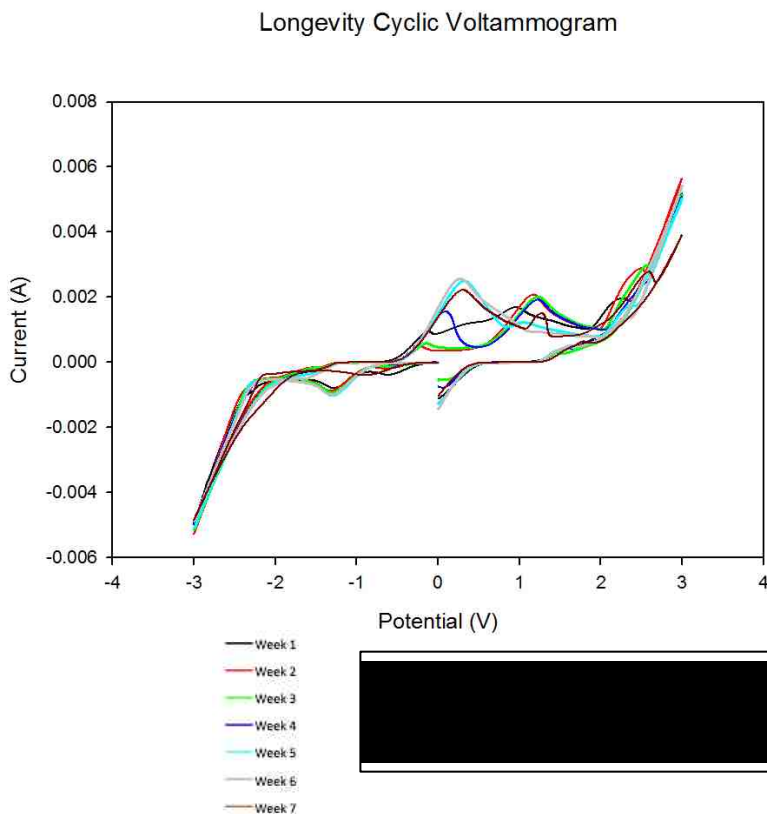
Figure 72 displays an expanded electrochemical window from -3.0 V to 3.0 V with isolated electrolyte components. As evidenced in Figure 72, the Cu^{2+} to Cu^{1+} and Ag^{1+} to Ag^0 transitions occur nearly in the



Typical Cyclic Voltammogram of REM Device

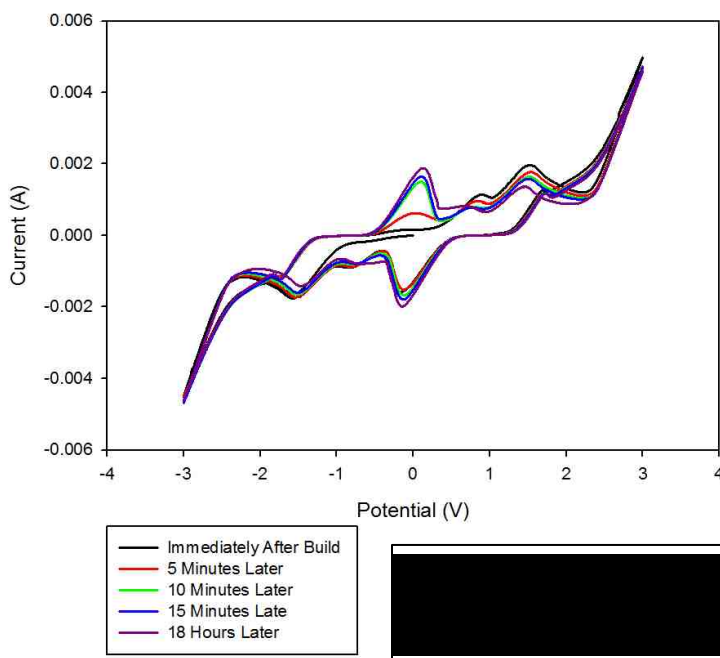


same potential, confirming that when combined, the silver and copper will co-deposit. Br^- , from the dissociation of tetrabutylammonium bromide, reduces to Br^{3-} at $\sim -2.1 \text{ V}$,¹²¹ but this has not shown to have any ill effects on the reversibility of the mirror plating.



Since these devices are to be used for long periods of time without being replaced, longevity experiments were conducted. Figure 73 shows the typical CV features so the reader may orient him/herself to the plating and dissolving regimes. The first longevity experiment (see Figure 74) was designed for a REM device to be used only once per day for seven weeks. The second experiment (Figure 75) was a cyclic voltammogram of a REM device that ran continuously for 18 hours. In both figures, the performance of the device can be measured by the solvation rate of the mirror. The solvation peak at 0.2 V is proportional to the rate of solvation, and from weeks 1-3, solvation rates were low. The very first experiment showed peak broadening during the solvation period. This has been

Continuous Cyclic Voltammograms Immediately After Device Fabrication

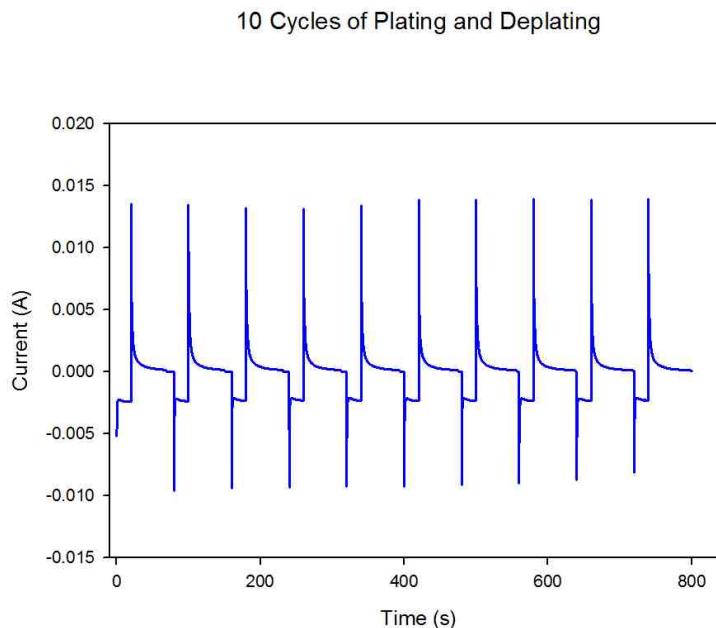


observed for all devices when immediately tested after their construction: the mirror does not solvate back into solution very well—this is because there is a stabilization time with the electrolyte gel

matrix. Through observing the dissolving of the mirror, solvation would take approximately three times longer than the actual plating on the ITO. On week 4, a transition is occurring, and solvation becomes much faster than previous weeks. Eventually, weeks 5 and 6 show full optimization of the solvation peak, where we observe the dissolving of the mirror 33% faster than when the device was first made. The device does not improve beyond a 1:2 ratio of plating: deplating times, and with just one cycle per day, the device is optimized in 3 weeks. With continuous cyclic (Figure 75), however, the same ratio is achieved after 10 minutes. The stabilization of the TBABr and PVB matrix could be stabilized through continuous cycling of the device, rather than waiting three weeks for the gel to stabilize. It was also observed when REM devices were built with very thin Teflon spacers (<200 μm), the PVB gel would form visible cross-

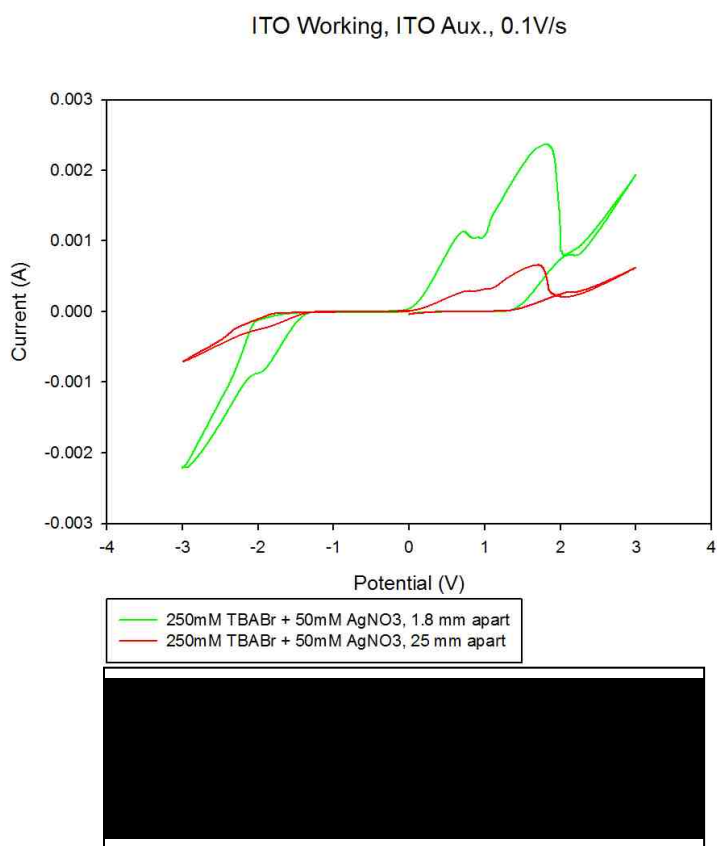
linking bridges with the ITO glass, eventually preventing reversible plating. When the gel was removed, these bridges were also eliminated.

CVs are powerful tools because the experiments show



changes in the medium as the potential is slowly ramped. Stepping voltages provide a different picture, and Figure 76 illustrates that the device works very well under plating and deplating voltages with no ramping in-between. The negative current is the plating regime, while the positive current is the deplating or dissolving of the mirror. The shape of the curves is interesting to note. While plating the current is very high and immediately tapers after the initial nucleation. The deplating regime looks like a $1/x$ regression since less material is present on the ITO over time (very similar to the kinetics of radioactive decay).

During initial experimentation, it was observed that dangling two facing ITO-doped glass slides in electrolyte solution would provide inconsistent and unreliable results. Even still, the silver plating on the ITO was black and metallic, but it certainly was not reflective. After investigation of this strange occurrence, it



was discovered that these plating systems have an optimal coupling distance for pristine plating. Figure 77 shows an example CV of the difference between plating and the distance of ITO electrodes. The difference in amplitude of the peak currents at

1.8 mm apart vs. 5 mm apart is striking. When the amplitude in the plating regime increased, a highly reflective silver mirror appeared, and the deplating was fast and uniform. The opposite can be said of the much larger distance. Future research will be conducted to optimize this distance for plating.

Investigation into the electrolyte was engaged. First, a saturated solution of AgNO₃ was prepared, but once a 2:1 TBABr:AgNO₃ threshold was crossed, AgBr formed and precipitated out of solution. In this system, a 2.1:1 TBABr:AgNO₃ ratio was maintained and labeled as “saturated”, even though the saturation point of Ag⁺ in DMSO was not approached. Araki *et al.* reported that the CuCl₂ was essential in the reversibility of the reaction. In order to test this

hypothesis, several electrolyte solutions were made and their plating was determined. CuSO_4 and CuI were used as a replacement for CuCl_2 . The $\text{AgNO}_3/\text{CuSO}_4$ solution did not deposit any material at all, and the CV was relatively flat. The AgNO_3/CuI solution only plated a black film that was difficult to dissolve back into solution. Although the copper cations are important for reversibility, the chloride anions provide the environment needed to plate a shiny mirror. Other metal chlorides will be investigated to optimize reversibility and optical modulation.

After these experiments, CuCl_2 was replaced with equivalent amounts of acetaminophen, L-tyrosine, citric acid, and potassium chloride. The hypothesis was that none of these additives would help mirror formation, but surprisingly, all four of them formed a reversible mirror, with the citric acid solution forming a mirror as reproducible as the CuCl_2 system. Longevity experiments were performed on these solutions, and they all failed in producing mirrors after a week, but the possibility of doping the system with inorganic and organic additives will prove to be interesting research.

2.2 Optical Properties

The most important application of these reversible mirrors involves their optical properties. FTIR transmittance, single-wavelength reflectance, and multi-

wavelength reflectance

measurements were

carried out in order to

characterize the

optical properties of

the reversible mirrors.

The first

experiments to be

carried out were to see

how reflective the

mirrors are in a broad

spectrum of the IR region. Thermal radiation is represented by the IR region of the electromagnetic spectrum, and so the mirror's performance in the IR region is of great importance.

Figure 78 shows the IR transmittance vs. plating time. The upper-most black line represents the optical transmittance of the glass and electrolyte solution.

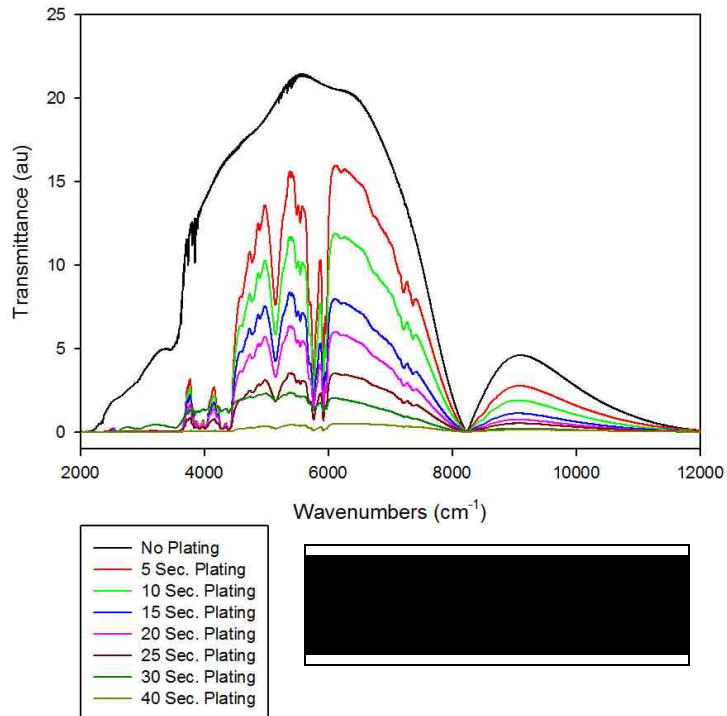
In the visible light, these are transparent, but the window of 2000 cm^{-1} to $12,000\text{ cm}^{-1}$ was chosen because the glass slides and electrolyte are very high absorbers outside that region.

As this research advances, zinc selenide¹²² and sapphire¹²³ cover glass will be investigated, since these materials are IR transparent.

Even after 5 seconds of plating, a significant decrease in transmittance can be observed, and within 40 seconds of plating at 2.8V, nearly

98% of the incident light is reflected back to the laser source, absorbed by the

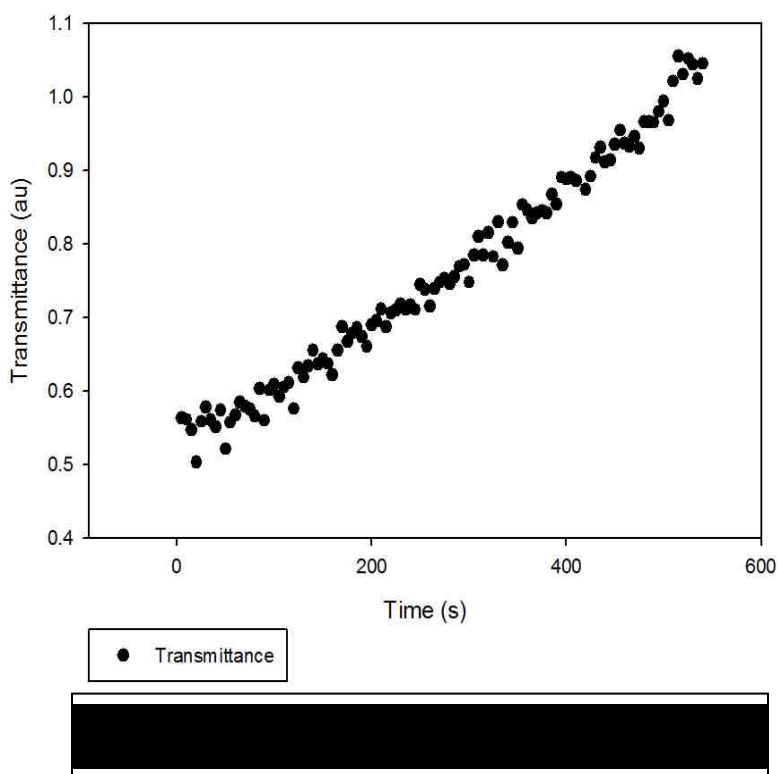
Transmittance of REM at 2.8v Vs. Time



mirror itself, or scattered away from the detector. More STAR (scattering, transmission, absorbance, reflectance) measurements will need to be taken to determine the ratio of the afore-mentioned optical properties in a more sophisticated experiment.

It was observed during this experiment that the silver plate dissolves

Transmittance Vs. Time, Natural Dissolution, 5972 cm⁻¹



naturally when a potential is not applied.

This correlates to the CVs already covered in the previous section—that at 0 V, there is slow solvation of the mirror back into solution. Figure 79 displays the transmittance change over time as the mirror

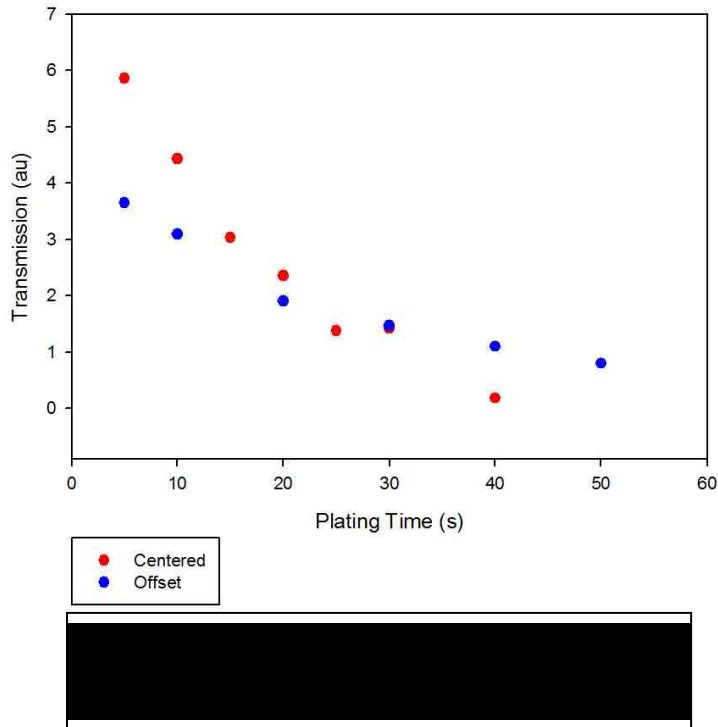
slowly dissolves naturally. The wavenumber 5972 cm⁻¹ was chosen because it is one of the peaks in the FTIR experiment that shows drastic change over time, and that particular wavelength could be used to isolate transmittance of the mirror. Interesting to note, the mirror was visibly gone at approximately six minutes, but the transmittance still increased steadily several minutes after the

mirror seemed to disappear. Collaborators at the Air Force Research Laboratory are currently investigating this system of solvent clusters and their effect upon transmittance and reflectance.

The REM window is circular, and therefore, there are three different plating structures that are built during deposition, if the deposition rate is constant and assuming the ITO surface is smooth. If the plating were uniform, the mirror structure would be cylindrical (Figure 80a). If, however, the plating were not uniform, the architecture of the mirror could be a dome or a bowl, depending on whether the plating occurs faster in the center or the edge (Figures 80b and 80c). In order to determine if the plating is uniform, the IR laser source was directed through the center of the window and through the edge. Figure 81 displays the peak transmittance vs. plating time at 5972 cm^{-1} at the center of the window and the edge. If the plating were uniform on the edges and center, the decreases in transmittance as plating time increases would be identical; however, this pattern is not observed. The center of the window has a much sharper decline in



Transmission Vs. Plating Time, 2.8V, 5972 cm⁻¹

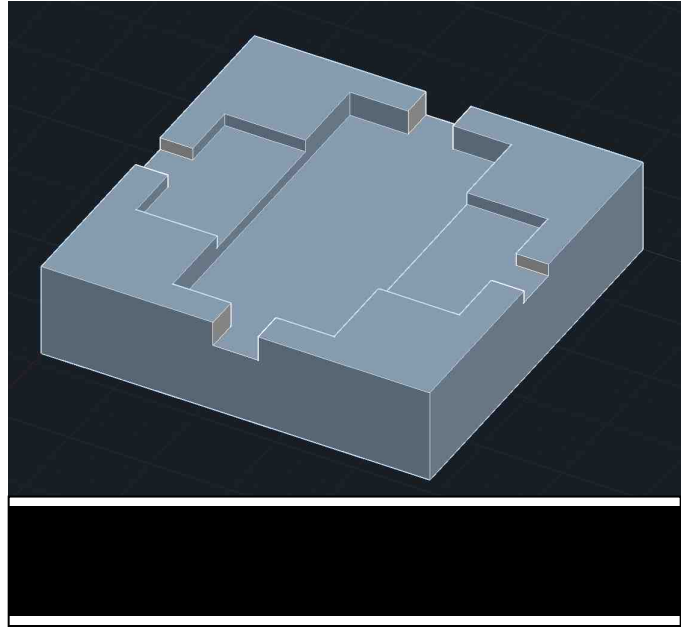


transmission than the edges, showing that the plate does not form uniformly on the atomic scale. Initially, the edge plates more material than the center, but after 30 seconds, the center has more deposited material. This

suggests a hybrid structure between the dome and bowl architectures: that a bowl forms initially, but then it fills in with silver nanoparticles. Surface imaging techniques have to be employed in order to understand the plating architecture.

In order to utilize an atomic force microscope or surface profilometer, a different REM housing needed to be designed and built. Since the mirror dissolves naturally, a quick and easy method needed to be developed to perform surface imaging of the formed mirror. A disadvantage with the original aluminum housing was that it simply took too long to unscrew four bolts and remove the aluminum plate from the glass slides. By the time the bolts were removed, the mirror had already vanished. Figure 82 is the design that was proposed for the new housing. The housing is made of Teflon polymer, and it enables very quick

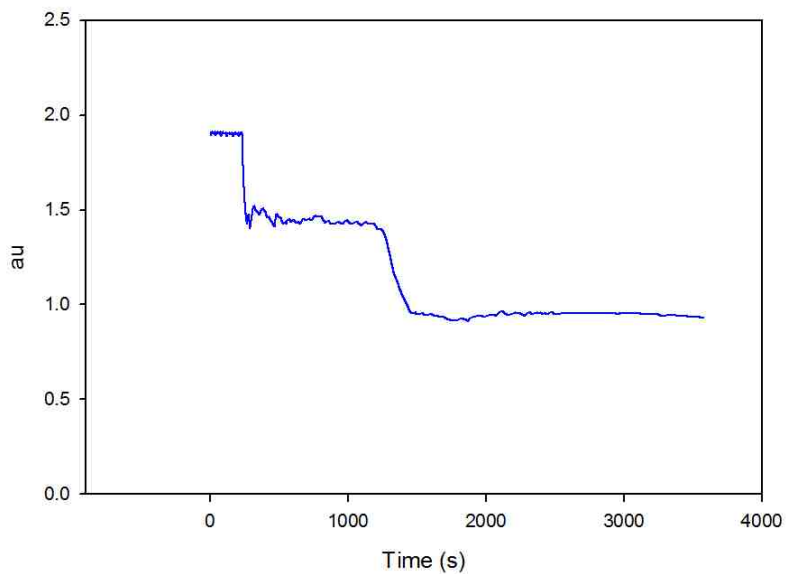
removal of the glass slides when the plating time is complete. When the glass slides were removed from the new housing, exposure to air immediately oxidized the silver mirror, turning the shiny metal film into a tarnished, metallic layer within minutes. Ag^0



readily oxidizes in air due to the presence of low levels of ozone (O_3).¹²⁴ In order to determine the nano-architecture of the silver deposit, experiments need to be conducted in an inert atmosphere.

The mirror's instability is an undesired feature since an intended optical property would only be fleeting. Therefore, by using a 633 nm, 5 mW laser and a feedback loop designed in Labview,

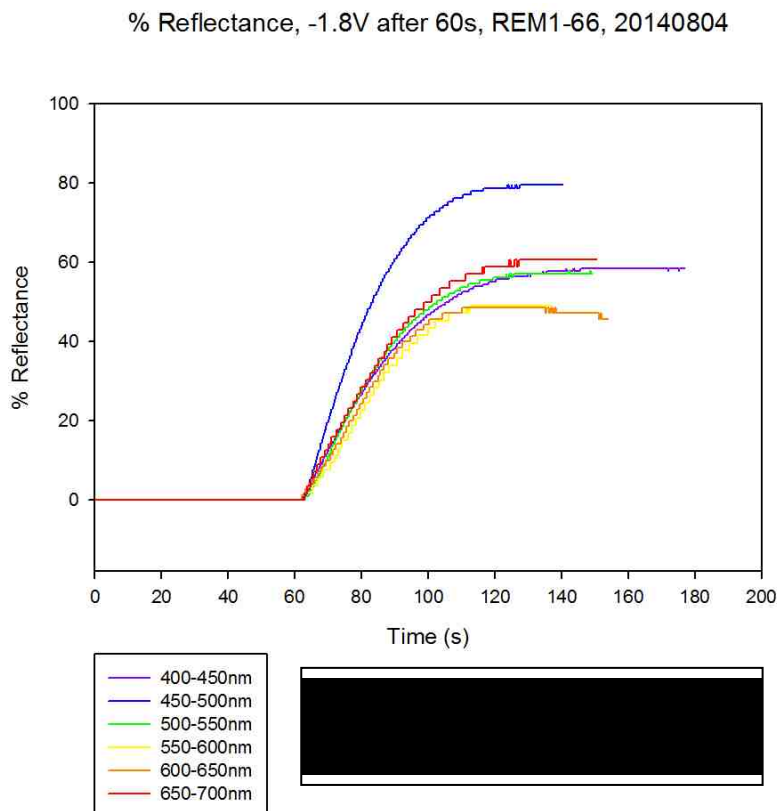
Transmittance at 75% and 50%, 633nm



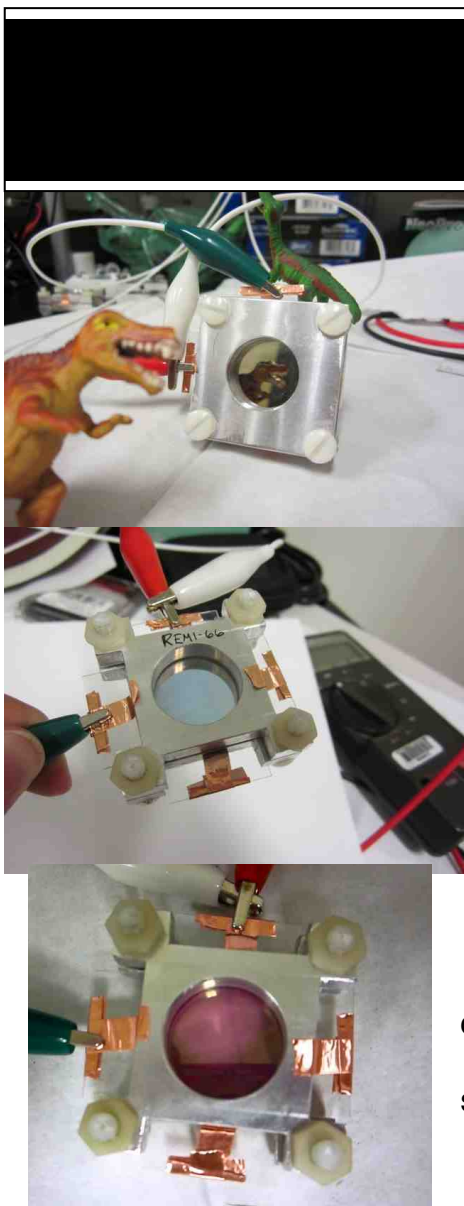
mirror stabilization was achieved. The potential required to plate silver onto the ITO is 2.5 V, and as discovered by the Labview program the potential required to maintain the mirror at its current state is ~ 0.8 V. This is an important step in electrophoretic mirror technology, as low power (~ 0.8 V at 2 mA is 1.6 mW) is required to stabilize the mirror, which is a very attractive feature in fine-tuning optical properties for space and other applications. Figure 83 displays the stabilization of the mirror. It was shown earlier (Figure 79) that the mirror was completely dissolved within 10 minutes, but by applying low voltage in the feedback loop, 75% transmittance for a 633 nm laser was maintained for nearly 1000 seconds (~ 17 minutes), and 50% transmittance was maintained for over 2000 seconds (~ 33 minutes). This proves the device's viability in optical modulation.

By using a white light source and filtering different wavelengths, the device's performance in reflecting these various spectra of light was determined.

Figure 84 depicts the reflectivity of the



reversible mirror of these different bands of visible light. UV light was unavailable to our research team at the time of experimentation, but UV transmission and reflection experiments should be performed in the future. A simple pattern cannot be determined from these experiments, but it does show that the mirror reflects different wavelengths of light differently. It is important then to test other systems in the future in order to create a portfolio of best-fit optical properties for a customer, mission, or application.



By establishing voltage ramps or constant voltages, a reflective surface develops on the REM device. If the user applies a short burst of high voltage (ranging from 3-4.5 V), a range of nanoparticle sizes can be deposited on the ITO. Then, using a much lower potential (ranging from 1.3-1.8 V), the film can be grown using the nanoparticles as a seed layer. The result is a colored window rather than a reflective mirror (although if left to continue plating even at very low voltages, a mirror will eventually form).

Figure 85 is a set of pictures that illustrates the color modulation of the REM device. Figure 85a shows full reflectivity during a 2.5 V plating

session of the REM device. Figure 85b depicts a light blue film. This was created by pulsing a 4.5 V surge for 0.2 s and then building up a silver nanoparticle layer at 1.8 V for 15 s. Figure 85c shows a pink film in the REM device that was produced with a shock of 4.1 V for 0.3 s and a building-up time of 10 s at 1.8 V. Although the mirror formation was expected, the colored film was not. It is believed that these nanoparticles are experiencing surface plasmon resonance in the visible spectrum. Small nanoparticles absorb in the blue light wavelength (400-500 nm) and reflecting red light (~700 nm). Larger nanoparticles red-shift in absorbance and then reflect blue light.¹²⁵ This is consistent with our experimental findings because the red film always appears before the blue film.

2.3 Spot Deposition and Mirror Migration

By collaborating with the Cold Atom Laboratory at the Air Force Research Laboratory (AFRL) at Kirtland AFB, NM, a new type of device was built. Electrically isolated sections of the ITO layer created by etching the glass with a high power laser capable of etching 50 μm -wide channels. Twelve 30° wedges were engraved into one glass slide, and Figures 86a and 86b display the result. Each wedge is electrically isolated from each other, so that precise patterns can be mirrored or colored as desired. Programs in Labview can be created in order to demonstrate the migration of the mirror in an assortment of patterns as well.

The drawback of using the laser engraver is the permanence of the pattern.

Future investment with the Advanced Materials Lab—a Sandia National

Laboratory and University of

New Mexico collaborative

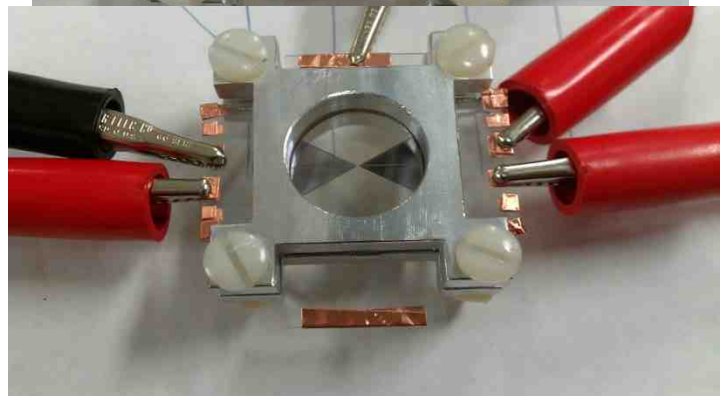
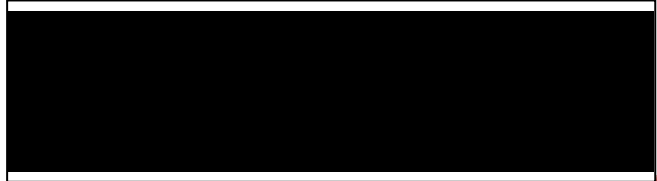
effort—will investigate 3D

lithography techniques so

that an array of patterns can

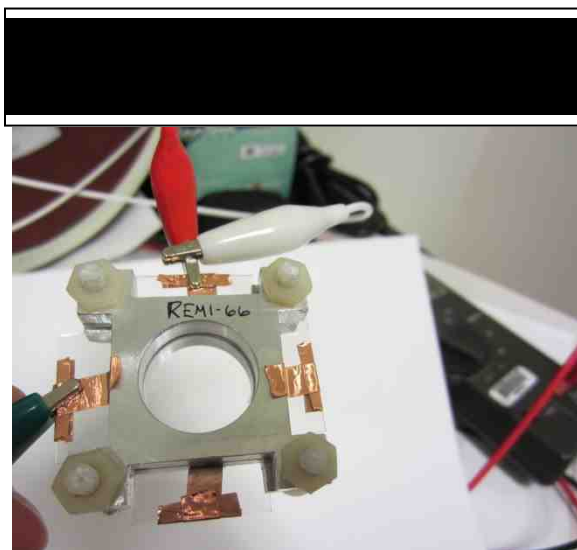
be developed without

damaging the ITO layer.



Chapter 3: Experimental

Silver nitrate, copper (II) chloride, tetrabutylammonium bromide, dimethyl sulfoxide, and Butvar B-98 were purchased from Sigma Aldrich and used without further purification. ITO-doped glass slides were supplied by Delta Technologies (25 mm x 50 mm x 0.7 mm, with an evenly dispersed ITO layer of 60-100 nm on

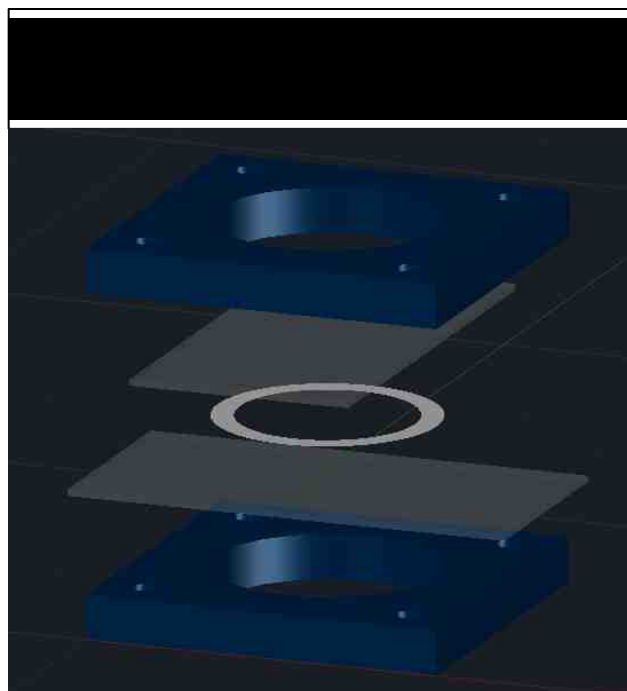


one side). An aluminum housing was designed to hold the glass slides together while experiments were performed. Figure 87 shows a typical REM device. Two 2 in. x 2 in. aluminum plates maintain tension on the ITO-doped glass slides by tightening a set of four Teflon screws.

A Teflon spacer was sandwiched in-between the glass slides—200 or 500 μm were typical sizes that were employed. Lastly, copper foil tape was used as a protector of the ITO layer from the alligator clips used to deliver potential differences. Figure 88 is an exploded view of the REM device.

The ITO-doped glass was not used as delivered. First, each slide was submerged in a beaker of acetone and sonicated for five minutes. The slide was then washed twice with acetone and allowed to air-dry. It was then submerged in

a beaker of ethanol and sonicated again for 10 minutes. The slide was carefully removed and washed with deionized water and ethanol. Finally, the remaining ethanol was removed with a stream of clean, dry air. Mixing acetone and water or ethanol formed an undesirable cloudy film



on the ITO, so care must be taken to ensure the acetone is evaporated completely from the slide.

To prepare the gel electrolyte for the electrochemical cell, 85 mg AgNO_3 (0.5 mmol), 806 mg Bu_4NBr (2.5 mmol) as supporting electrolyte, and 13 mg CuCl_2 were dissolved in 10 mL DMSO. 10% Butvar B-98 was mixed into the solution vigorously with a glass stir rod. Care must be taken with stirring in the host polymer to ensure an homogenous mixture to form a thick, smooth gel. Careless stirring will result in a clumpy, useless electrolyte gel. All electrochemical analyses were conducted on a CH Instruments 660s Electrochemical Workstation.

3.1 Summary and Future Work

With thorough examination of an organic substrate used for electrophoretic deposition, we show that a reversible mirror can be employed to obtain a desired optical transmittance and reflectance. We also show the possibility of the same system filtering bands of visible light. Although not inducing an instantaneous change provided by electrochromics, electrophoretics prove to have more desirable properties due to adaptability and reliability. Within 40 seconds, the electrophoretically-deposited silver reflected over 98% of IR radiation, proving that this technology can control thermal uptakes and losses in a terrestrial or space settings. We also discovered other uses for this technology with spot depositions and mirror migrations that could be very useful in different applications.

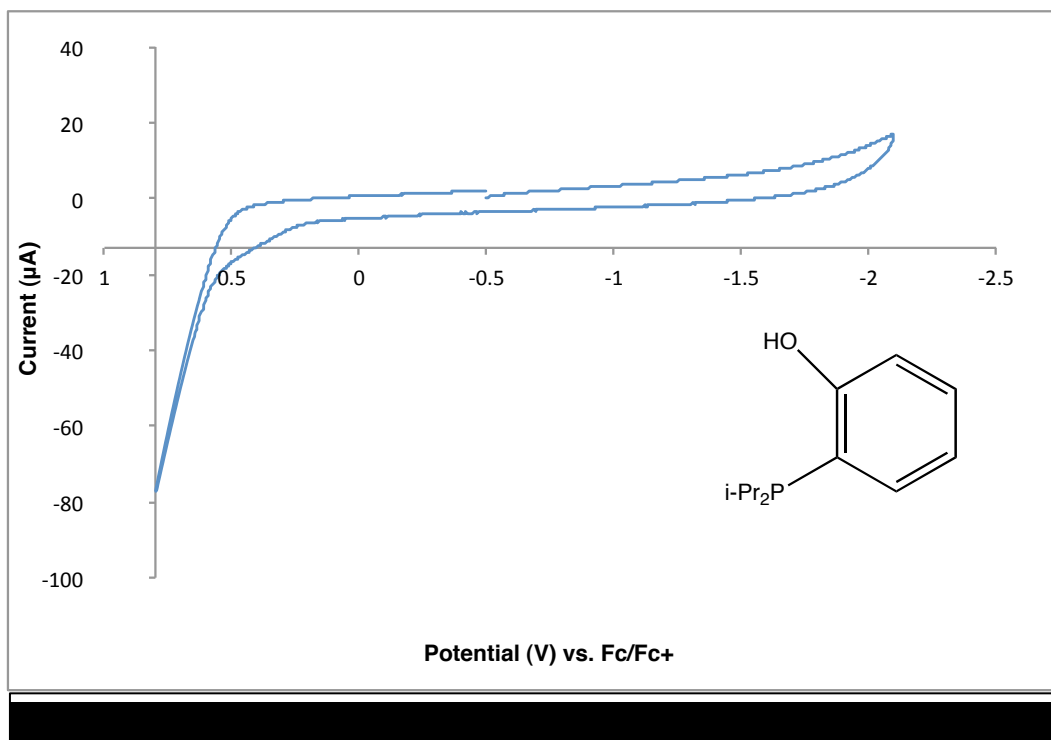
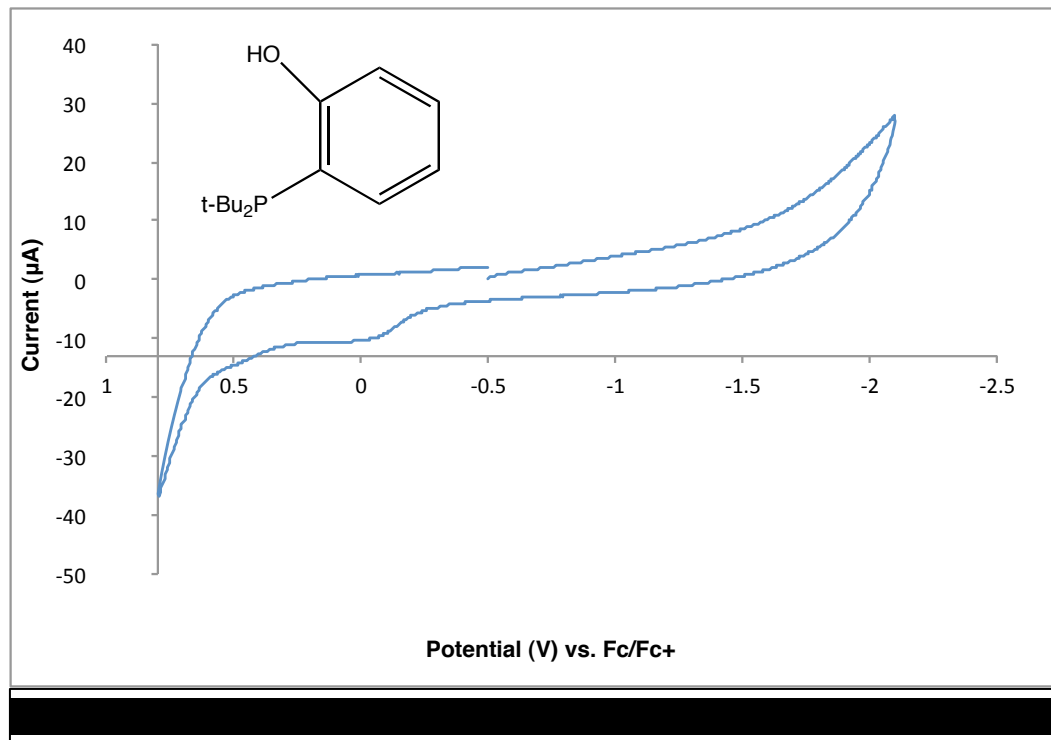
The investigation of electrophoretic deposition of silver has only just begun. The overall study of silver deposition from organic media has been studied extensively, so now the group's research will move to deposition in ionic liquid media. Organic media would be unsuitable for space applications due to their immediate volatility when exposed to a vacuum. To date, there are only a few publications on the electrophoretic deposition of metal from ionic liquids: aluminum,¹²⁶ magnesium,¹²⁷ and silver.^{128,129} Aluminum and magnesium do not offer the desired optical reflectance that silver does, and so immediately, the group will begin to research silver deposition. Other metals will follow in the

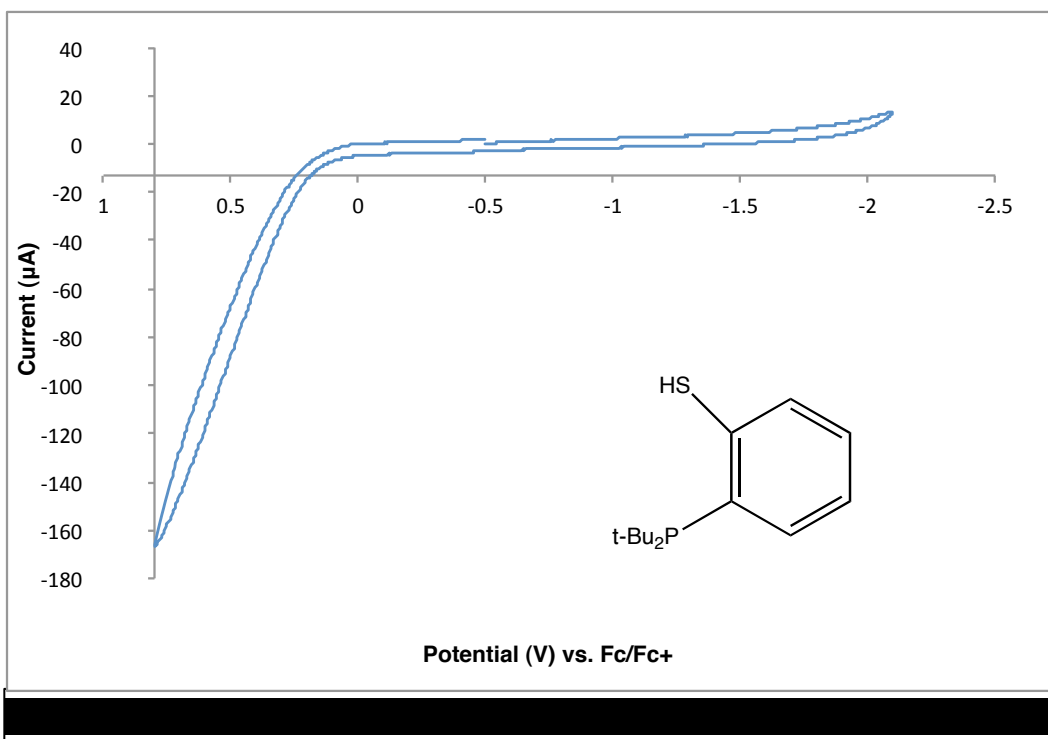
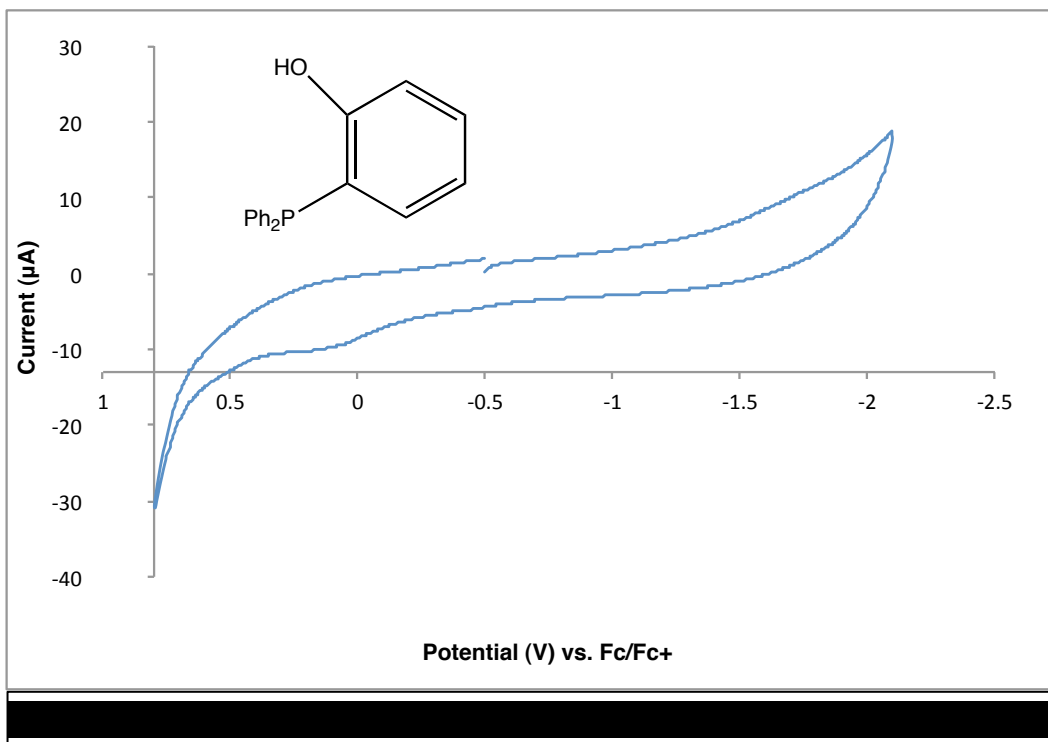
future, but silver holds the best promise for thermal control. There are thousands of ionic liquids to choose from,^{130, 131, 132, 133, 134} so the research team will conduct a variety of electrochemistry experiments to determine which candidates are optimal in their transport of electrons and redox species. Ionic liquids will be most advantageous in many space applications due to their very low volatility, chemical resilience, and large electrochemical window.

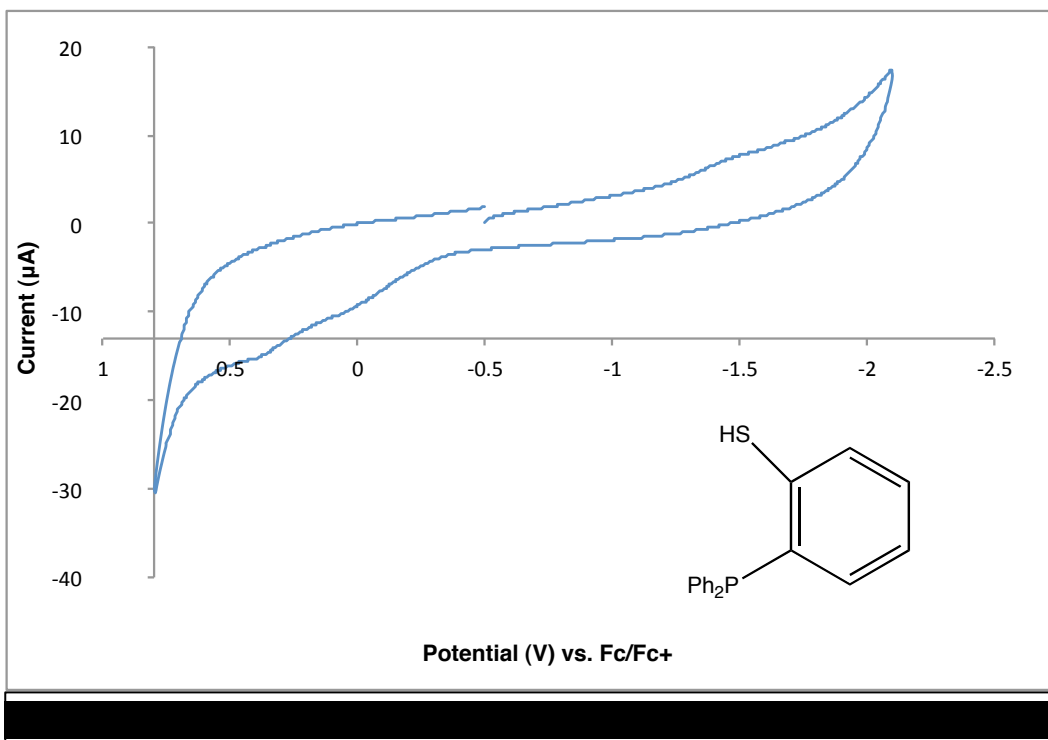
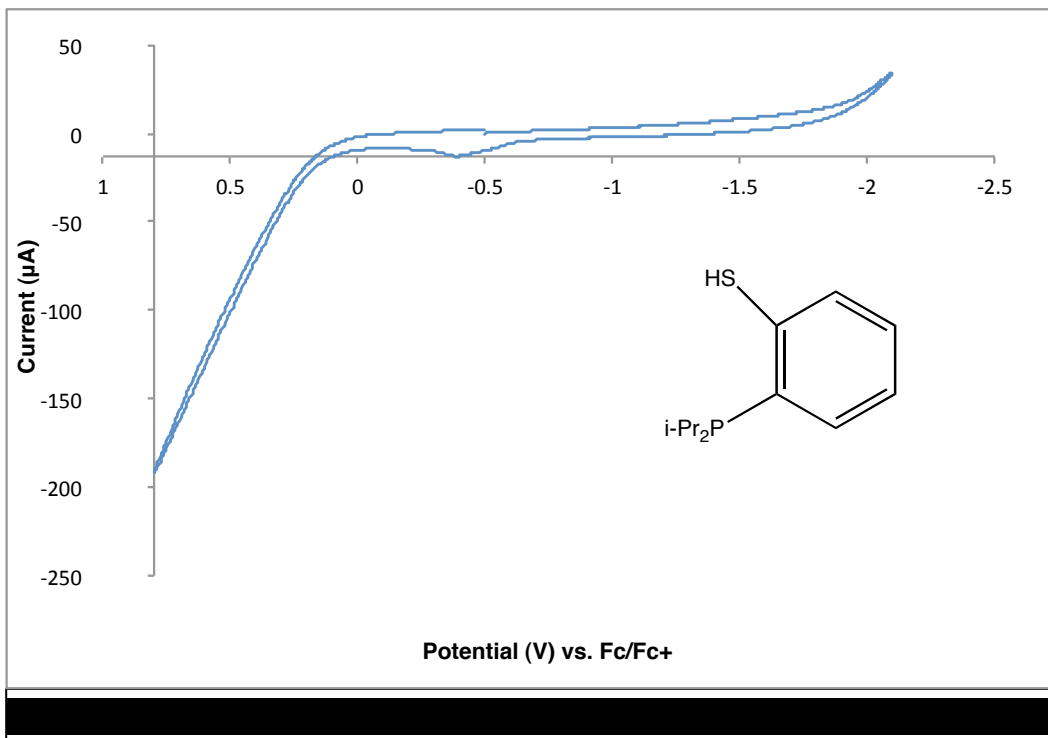
With respect to spot deposition and mirror migration, the research group hopes to obtain much larger pieces of ITO-doped glass and employ 3D lithography techniques to form patterned circuits. The plating does not drift away from the working electrode, meaning, that if the working electrode were a point source and the counter electrode was a large square plate, the plating would only occur at the pixel where the working electrode emanated an electric field. This is an important observation, and further work will be done to determine the validity of this technology in information display technologies.

Appendix 1

Figures **A1-A6** display the cyclic voltammograms of ligands 1-6 at 0.5 Vs^{-1} in $0.10 \text{ M Bu}_4\text{NPF}_6$ in THF under an Ar(g) saturated atmosphere.



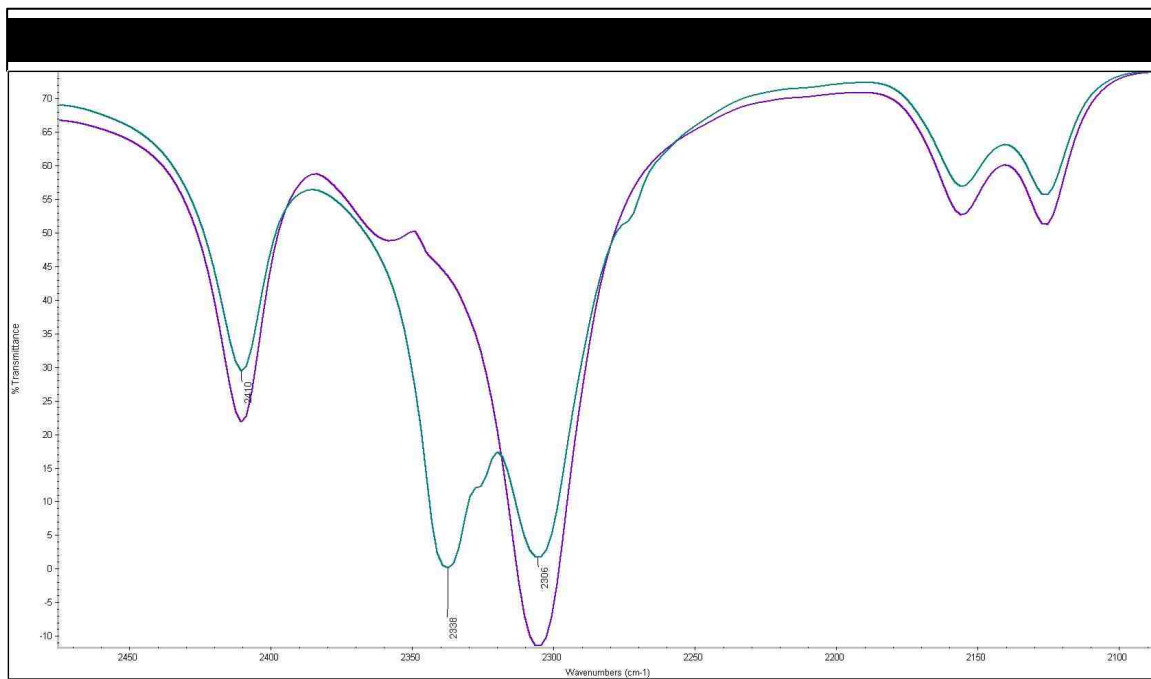




Appendix 2

Compound	1	17	17+
Empirical Formula	C ₁₄ H ₂₃ OP	C ₂₃ H ₃₁ PSZr	C ₄₆ H ₂₈ BF ₂₀ PSZr
Fw	238.29	461.73	1125.74
Cryst. Size (mm)	0.33 x 0.21 x 0.20	0.11 x 0.10 x 0.08	0.72 x 0.43 x 0.37
Cryst. Syst.	Monoclinic	Monoclinic	Triclinic
Space Group	P2(1)/c	Cc	P-1
a, Å	12.5801(5)	14.5998(14)	11.0308(2)
b, Å	10.0266(4)	15.2389(14)	12.0175(3)
c, Å	12.2556(5)	10.2268(9)	16.7618(4)
α, deg.	90	90	82.6820(10)
β, deg.	111.976(2)	108.490(5)	81.2200(10)
γ, deg.	90	90	79.3960(10)
Volume (Å ³)	1433.55(10)	2157.9(3)	2147.15(8)
Z	4	4	2
Calc. Density, g/cm ³	1.104	1.421	1.741
μ(MoK _α), mm ⁻¹	0.172	0.685	0.465
Indep. Reflecns.	2941	4056	10601
T, K	173(2)	173(2)	173(2)
R1, wR2 (all data)	0.0659, 0.1439	0.0223, 0.0653	0.0504, 0.1009
R1, wR2 [<i>I</i> >2σ(<i>I</i>)]	0.0478, 0.1314	0.0207, 0.0563	0.0361, 0.0881
GOF on F ²	1.073	1.165	1.060

Appendix 3



References

-
- ¹ World Energy Outlook 2013 Factsheet, International Energy Agency; Paris, France, (accessed Aug 24, 2014).
- ² United States Census Bureau. Population Clock. <http://www.census.gov/popclock/> (accessed Aug 24, 2014).
- ³ International Energy Agency. CO₂ Emission from Fuels Combustion— Highlights, **2013**; <http://www.iea.org/publications/freepublications/publication/co2emissionsfromfuelcombustionhighlights2013.pdf> (accessed Aug 24, 2014).
- ⁴ Garcia, R. A.; Cabeza, M.; Rahbek, C.; Araujo, M. B. *Science*, **2014**, *344*, 1247579.
- ⁵ Mackenzie, C. L.; Ormondroyd, G. A.; Curling, S. F.; Ball, R. J.; Whiteley, N. M.; Malham, S. K. *PLoS One*, **2014**, *9*, e86764/1.
- ⁶ O'Brien, M. J.; Philipson, C. D.; Tay, J.; Hector, A. *PLoS One*, **2013**, *8*, e70287.
- ⁷ Newingham, B. A.; Vanier, C. H.; Charlet, T. N.; Ogle, K.; Smith, S. D.; Nowak, R. S. *Glob. Chang. Biol.* **2013**, *19*, 2168.
- ⁸ Vaisanen, M.; Ylanne, H.; Kaarlejarvi, E.; Sjogersten, S.; Olofsson, J.; Crout, N.; Stark, S. *Nat. Clim. Change*, **2014**, *4*, 384.
- ⁹ Sovada, M. A.; Igl, L. D.; Pietz, P. J.; Bartos, A. J. *PLoS One*, **2014**, *9*, e83430/1.
- ¹⁰ Prietzel, J.; Christophel, D. *Geoderma*, **2014**, *221-222*, 28.
- ¹¹ Leitner, W. *Angew. Chem., Int. Ed. Engl.* **1995**, *34*, 2207.

-
- ¹² Notz, R.; Toennies, I.; Scheffknecht, G.; Hasse, H. *Chem. Ing. Tech.* **2010**, *82*, 1639.
- ¹³ Zhang, X.; He, X.; Gundersen, T. *AIChE Annu. Meet. Conf. Proc.* **2012**, 1.
- ¹⁴ Hong, S.-H.; Jang, M.-S.; Cho, S. J.; Ahn, W.-S. *Chem. Commun. (Cambridge, U. K.)* **2014**, *50*, 4927.
- ¹⁵ Sabouni, R.; Kazemian, H.; Rohani, S. *Environ. Sci. Pollut. Res.* **2014**, *21*, 5427.
- ¹⁶ Anderson, M.; Wang, H.; Lin, Y. S. *Rev. Chem. Eng.* **2012**, *28*, 101.
- ¹⁷ Benson, Eric E., Kubiak, C. P., Sathrum, Aaron J., Smieja, Jonathan M., *Chem. Soc. Rev.* **2008**, *38*, 89.
- ¹⁸ Hori, Y. *Electrochemical CO₂ Reduction on Metal Electrodes* Springer, 2008; Vol. 42.
- ¹⁹ Aresta, M. *Act. Small Mol.* **2006**, 1-41.
- ²⁰ Wang, G.; Zhang, X.; Chen, K.; Wang, Z.; Wang, T.; Wang, D.; Qu, J.; Wang, J.; Zhou, Z.; (Wuhan Kelin Fine Chemical Co., Ltd., Peop. Rep. China).
Application: CN, 2015, p 13.
- ²¹ Anderson, A. B.; Asiri, H. A. *Phys. Chem. Ch. Ph.*, **2014**, *16*, 10587.
- ²² Li, Y.-N.; Ma, R.; He, L.-N.; Diao, Z.-F. *Catal. Sci. Technol.* **2014**, *4* (6), 1498-1512.
- ²³ Xu, Y.-f.; Wang, J.-b.; Liu, H.-j.; Zhang, X.-l. *Xiandai Huagong*, **2013**, *33*, 70.
- ²⁴ Bard, A. J.; Faulkner, L. R. *Electrochemical Methods*, 2001.

-
- ²⁵ Sawyer, Donald T.; Sobkowiak, Andrzej; Roberts, Julian L. *Electrochemistry for Chemists*, 1995, 2nd Ed.
- ²⁶ Gritzner, G; Kuta, J, *Pure & Appl. Chem.*, **1982**, 54(8), 1527-1532.
- ²⁷ Aresta, M.; Dibenedetto, A.; Angelini, A. *Chem. Rev.* **2014**, 114, 1709.
- ²⁸ J. M. Saveant, *Chem. Rev.*, 2008, **108**, 2348.
- ²⁹ Hansen, H. A.; Varley, J. B.; Peterson, A. A.; Norskov, J. K. *J. Phys. Chem. Lett.* **2013**, 4, 388.
- ³⁰ Qiao, Jinli, *Chem. Soc. Rev.*, **2014**, 43, 631–675.
- ³¹ Ramesha, G. K.; Brennecke, J. F.; Kamat, P. V. *ACS Catalysis*, **2014**, Ahead of Print.
- ³² Y. Hori, *Handbook of Fuel Cells*, John Wiley & Sons, Ltd, 2010.
- ³³ K. Watanabe, U. Nagashima and H. Hosoya, *Chem. Phys. Lett.* **1993**, 209, 109–110.
- ³⁴ Hatsukade, T.; Kuhl, K. P.; Cave, E. R.; Abram, D. N.; Jaramillo, T. F. *Phys. Chem. Chem. Phys.* **2014**, 16, 13814.
- ³⁵ Chen, Y. H.; Li, C. W.; Kanan, M. W. *J. Am. Chem. Soc.* **2012**, 134, 19969–19972.
- ³⁶ K. Ogura, H. Yano and F. Shirai, *J. Electrochem. Soc.* **2003**, 150, D163–D168.
- ³⁷ Chi, D.; Yang, H.; Du, Y.; Lv, T.; Sui, G.; Wang, H.; Lu, J. *RSC Advances* **2014**, Ahead of Print.
- ³⁸ Seshadri, G.; Lin, C.; Bocarsly, A. B. *J. Electroanal. Chem.* **1994**, 372, 145.
- ³⁹ Dickie, D. A.; Coker, E. N.; Kemp, R. A. *Inorg. Chem.* **2011**, 50, 11288.

-
- ⁴⁰ Atkins, P. O., Tina; Rourke, Jonathan; Weller, Mark; Armstrong, Fraser.
Inorganic Chemistry, Oxford University Press, 2004, 4th Ed.
- ⁴¹ Chapman, A. M.; Haddow, M. F.; Wass, D. F. *J. Am. Chem. Soc.* **2011**, *133*, 18463.
- ⁴² Welch, G. C.; Cabrera, L.; Chase, P. A.; Hollink, E.; Masuda, J. D.; Wei, P.; Stephan, D. W. *Dalton Trans.* **2007**, 3407
- ⁴³ Stephan, D. W.; Erker, G. *Chem. Sci.* **2014**, *5*, 2625.
- ⁴⁴ Lawrence, E. J.; Oganessian, V. S.; Hughes, D. L.; Ashley, A. E.; Wildgoose, G. *J. Am. Chem. Soc.* **2014**, *136*, 6031.
- ⁴⁵ Stephan, D. W. *Top. Curr. Chem.* **2013**, *332*, 1.
- ⁴⁶ Kehr, G.; Schwendemann, S.; Erker, G. *Top. Curr. Chem.* **2013**, *332*, 45.
- ⁴⁷ Flynn, S. R.; Wass, D. F. *ACS Catal.* **2013**, *3*, 2574.
- ⁴⁸ Atkins, P. O., Tina; Rourke, Jonathan; Weller, Mark; Armstrong, Fraser.
Inorganic Chemistry, Oxford University Press, 2004, pp 219-228. 4th Ed.
- ⁴⁹ Evans, D.; Osborn, J. A.; Wilkinson, G. *J. Chem. Soc. [Section] A: Inorganic, Physical, Theoretical*, **1968**, 3133.
- ⁵⁰ Smith, J. G. *Organic Chemistry, 2nd ed.*, 2007, 606-631.
- ⁵¹ Snieckus, V. *Chem. Rev.* **1990**, *90*, 879.
- ⁵² Francis A. Carey, R. J. S. *Advanced Organic Chemistry, Part A: Structure and Mechanisms, 4th ed.*, 2000, 206-207.
- ⁵³ Tolman, C. A. *Chem. Rev.* **1977**, *77*, 313.
- ⁵⁴ Boehm, S.; Fiedler, P.; Exner, O. *New J. Chem.* **2004**, *28*, 67.

-
- ⁵⁵ Bornand, M.; Torker, S.; Chen, P. *Organometallics*, **2007**, *26*, 3585.
- ⁵⁶ Block, E.; Ofori-Okai, G.; Zubieta, J. *J. Am. Chem. Soc.* **1989**, *111*, 2327.
- ⁵⁷ Morales-Morales, D.; Rodriguez-Morales, S.; Dilworth, J. R.; Sousa-Pedrares, A.; Zheng, Y. *Inorg. Chim. Acta.* **2002**, *332*, 101.
- ⁵⁸ Yardley, J. P.; Fletcher, H., III *Synthesis*, **1976**, 244.
- ⁵⁹ Jameson, C. J.; De Dios, A. C. *Nucl. Magn. Reson.* **2014**, *43*, 49.
- ⁶⁰ Kuhl, O. *Phosphorus-31 NMR Spectroscopy: A Concise Introduction for the Synthetic Organic and Organometallic Chemist*, 2008.
- ⁶¹ Bryliakov, K. P.; Talsi, E. P.; Bochmann, M. *Organometallics*, **2004**, *23*, 149.
- ⁶² Camara, J. M.; Petros, R. A.; Norton, J. R. *J. Am. Chem. Soc.* **2011**, *133*, 5263.
- ⁶³ Jantunen, K. C.; Scott, B. L.; Kiplinger, J. L. *J. Alloys Compd.* **2007**, *444-445*, 363.
- ⁶⁴ Petasis, N. A.; Bzowej, E. I. *J. Am. Chem. Soc.* **1990**, *112*, 6392.
- ⁶⁵ IR Data obtained from: <http://webbook.nist.gov/cgi/cbook.cgi?ID=C124389&Type=IR-SPEC&Index=1#IR-SPEC> (accessed Nov 13, 2014)
- ⁶⁶ Horton, A. D.; Orpen, A. G. *Organometallics*, **1991**, *10*, 3910.
- ⁶⁷ Jutzi, P.; C. Muller. *Organometallics*, **2000**, *19*: 1442.
- ⁶⁸ Chapman, A. M.; Haddow, M. F.; Wass, D. F. *J. Am. Chem. Soc.* **2011**, *133*, 8826.
- ⁶⁹ Federsel, C.; Boddien, A.; Jackstell, R.; Jennerjahn, R.; Dyson, P. J.; Scopelliti, R.; Laurency, G.; Beller, M. *Angew. Chem. Int. Ed.* **2010**, *49*, 9777.
- ⁷⁰ Froehlich, J. D.; Kubiak, C. P. *Inorg. Chem.* **2012**, *51*, 3932.

-
- ⁷¹ Peterson, A. A.; Abild-Pedersen, F.; Studt, F.; Rossmeisl, J.; Norskov, J. K. *Energy & Environmental Science*, **2010**, *3*, 1311.
- ⁷² Dobrovetsky, R.; Stephan, D. W. *Angew. Chem. Int. Ed.* **2013**, *52*, 2516.
- ⁷³ Seshadri, G.; Lin, C.; Cocarsly, A. B. *J. Electroanal. Chem.* **1994**, *372*, 145.
- ⁷⁴ Zink, D. M.; Bachle, M.; Baumann, T.; Nieger, M.; Kuhn, M.; Wang, C.; Klopfer, W.; Monkowius, U.; Hofbeck, T.; Yersin, H.; Brase, S. *Inorg. Chem.* **2012**, *52*, 2292.
- ⁷⁵ Garcia-Alvarez, R.; Garcia-Garrido, S. E.; Diez, J.; Crochet, P.; Cadierno, V. *Eur. J. Inorg. Chem.* **2012**, *2012*, 4218.
- ⁷⁶ Schilter, D.; Rauchfuss, T. B.; Stein, M. *Inorg. Chem.* **2012**, *51*, 8931.
- ⁷⁷ Bakhoda, A.; Safari, N.; Amani, V.; Khavasi, H. R.; Gheidi, M. *Polyhedron*, **2011**, *30*, 2950.
- ⁷⁸ Geiger, W. E. *Organometallics*, **2007**, *26*, 5738-5765.
- ⁷⁹ Wilkinson, G.; Rosenblum, M.; Whiting, M. C.; Woodward, R. B. *J. Am. Chem. Soc.* **1952**, *74*, 2125-6.
- ⁸⁰ Bollermann, T.; Gemel, C.; Fischer, R. A. *Coordin. Chem. Rev.* **2012**, *256*, 537-555.
- ⁸¹ Kang, P.; Cheng, C.; Chen, Z.; Schauer, C. K.; Meyer, T. J.; Brookhart, M. *J. Am. Chem. Soc.* **2012**, *134*, 5500-5503.
- ⁸² Donovan, E. S.; McCormick, J. J.; Nichol, G. S.; Felton, G. A. N. *Organometallics*, **2012**, *31*, 8067-8070.

-
- ⁸³ Costentin, C.; Drouet, S.; Robert, M.; Saveant, J.-M. *J. Am. Chem. Soc.* **2012**, *134*, 11235-11242.
- ⁸⁴ Shriver, D. F., and M. A. Drezdson. *The Manipulation of Air-sensitive Compounds*. 2nd ed. New York: Wiley, 1986. Print.
- ⁸⁵ Barry, B. M.; Stein, B. W.; Larsen, C. A.; Wirtz, M. N.; Geiger, W. E.; Waterman, R.; Kemp, R. A. *Inorg. Chem.* **2013**, *52*, 9875.
- ⁸⁶ Bryliakov, K. P.; Talsi, E. P.; Bochmann, M. *Organometallics*, **2004**, *23*, 149.
- ⁸⁷ Camara, J. M.; Petros, R. A.; Norton, J. R. *J. Am. Chem. Soc.* **2011**, *133*, 5263.
- ⁸⁸ Jantunen, K. C.; Scott, B. L.; Kiplinger, J. L. *J. Alloys Compd.* **2007**, *444-445*, 363.
- ⁸⁹ Saucedo, A.S.A.; Hagenbach, A.; Abram, U., *Polyhedron*, **2008**, *27*, 3587 – 3592.
- ⁹⁰ Blair, A. *Plat. Surf. Finish.* **1998**, *85*, 64.
- ⁹¹ "Moscow City, Russia (Moskva)." *Welcome to Moscow*. Web, accessed 18 Aug. 2014.
- ⁹² Freudenberger, R. *Jahrbuch Oberflächentechnik* **2001**, *57*, 33.
- ⁹³ Maiti, H. S.; Datta, S.; Basu, R. N. *J. Am. Ceram. Soc.* **1989**, *72*, 1733.
- ⁹⁴ Cannio, M.; Novak, S.; Besra, L.; Boccaccini, A. R. *Ceramics and Composites Processing Methods*, **2012**, 517.
- ⁹⁵ Ohta, W. *Proc. Int. Conf. Vac. Web Coat., 5th* **1991**, 2.
- ⁹⁶ Subrahmanyam, A.; Vasu, V. *Solid State Mater.* **1991**, 264.

-
- ⁹⁷ Xu, X.; Lei, G.; Xu, Z.; Shen, M. *Proceedings of SPIE-The International Society for Optical Engineering*, **1991**, 1519, 525.
- ⁹⁸ Zhao, J.; Qu, H.; Li, Y.; (Harbin Institute of Technology, Peop. Rep. China). **2014**, 8
- ⁹⁹ Xiao, X.; Xu, G.; Chai, G.; Zhang, H.; Zhan, Y.; Sun, Y.; (Guangzhou Institute of Energy Conversion, Chinese Academy of Sciences, Peop. Rep. China). **2014**, 7
- ¹⁰⁰ More, A. J.; Patil, R. S.; Dalavi, D. S.; Mali, S. S.; Hong, C. K.; Gang, M. G.; Kim, J. H.; Patil, P. S. *Mater. Lett.* **2014**, 134, 298.
- ¹⁰¹ Shen, N.; Chen, S.; Chen, Z.; Liu, X.; Cao, C.; Dong, B.; Luo, H.; Liu, J.; Gao, Y. *J. Mater. Chem. A*, **2014**, Ahead of Print.
- ¹⁰² Ramadan, R.; Kamal, H.; Hashem, H. M.; Abdel-Hady, K. *Sol. Energy Mater. Sol. Cells*, **2014**, 127, 147.
- ¹⁰³ Cai, G. F. Z., D.; Xiong, Q.Q.; Zhang, J.H.; Wang, X.L.; Gu, C.D.; Tu, J.P. *Sol. Energy Mater. Sol. Cells*, **2013**, 117, 231.
- ¹⁰⁴ Prochazka, J.; Kavan, L.; Zikalova, M.; Frank, O.; Kalbac, M.; Zikal, A.; Klementova, M.; Carbone, D.; Graetzel, M. *Chem. Mater.* **2009**, 21, 1457.
- ¹⁰⁵ Mavromichalaki H, Souvatzoglou G, Sarlanis C, *Adv. Space Res.* **2006**, 37, 1141
- ¹⁰⁶ Globus, AI (10 July 2002). "Appendix E: Mass Shielding". *Space Settlements: A Design Study*. NASA, accessed Aug 19, 2014.

-
- ¹⁰⁷ Atkinson, Nancy (24 January 2005). "Magnetic shielding for spacecraft". *The Space Review*, accessed Aug 19, 2014.
- ¹⁰⁸ Kudela K., Storini M., Hofer M. Y. and Belov A. *Space Sci. Rev.* **2000**, *10*, 153.
- ¹⁰⁹ Bucík R., Bobík P. *Adv. Space Res.* **2008**, *42* (7) 1300.
- ¹¹⁰ Valach F., Revallo M., Hejda P., Bochníček J. *Acta Astronautica*, **2011**, *69*, 758.
- ¹¹¹ Micrometeoroids and Orbital Debris (MMOD) - NASA - White Sands Test Facility, Las Cruces, NM, accessed Aug 19, 2014.
- ¹¹² Fox, A. *Proceedings of the Intersociety Energy Conversion Engineering Conference*, **1989**, *24th*, 63.
- ¹¹³ O'Brien, R. C.; Ambrosi, R. M.; Bannister, N. P.; Howe, S. D.; Atkinson, H. V. *J. Nuc. Mater.* **2008**, *377*, 506.
- ¹¹⁴ Leontiev, A. I.; Diev, M. D.; Cykhotsky, V. M.; Prokhorov, Y. M.; Bednov, S. M.; Desyatov, A. V.; Blinkov, V. N.; Gorbenko, G. A.; Kopyatkevich, R. M. *AIP Conference Proceedings*, **1997**, *387*, 541.
- ¹¹⁵ Stevenson, J. A. G., J. C. *Radiation Heat Transfer Analysis for Space Vehicles*, United States Air Force, 1961.
- ¹¹⁶ Kreith, F. *The CRC Handbook of Thermal Engineering*, 1999.
- ¹¹⁷ Besra, L.; Liu, M. *Prog. Mater. Sci.* **2006**, *52*, 1.
- ¹¹⁸ Araki, Shingo, *Adv. Mater.* **2012**, *24*, OP122-OP126
- ¹¹⁹ Felton, G. A. N.; Petro, B. J.; Glass, R. S.; Lichtenberger, D. L.; Evans, D. H. *J. Am. Chem. Soc.* **2009**, *131*, 11290

-
- ¹²⁰ Bard, A. J.; Faulkner, L. R. "Electrochemical Methods. Fundamentals and Applications", 2nd Ed. Wiley, New York. 2001.
- ¹²¹ Branigan, E. T.; Halberstadt, N.; Apkarian, V. A. *J. Chem. Phys.* **2011**, *134*, 174503/1.
- ¹²² Cheng, N.; Xue, K.; Tang, X. *Hongwai Yanjiu*, **1984**, *3*, 123.
- ¹²³ Feng, L.; Liu, Z.; Wang, Y.; (Northwestern Polytechnical University, Peop. Rep. China). Application: CN, 2011, p 8.
- ¹²⁴ Stoullil, J.; Anisova, M.; Mistova, E.; Fojt, J. *Anti-Corros. Method. M.* **2014**, *61*, 38.
- ¹²⁵ Bohrenm, C. F.; Huffman, D. R. Absorption and Scattering of Light by small particles; John Wiley and Sons, Inc.: New York, 1983.
- ¹²⁶ Moustafa, E. M. *J. Phys. Chem. B* **2007**, *111*, 4693-4704
- ¹²⁷ Zhao, QingSong *Int. J. Electro.* **2012**, 701741, 1-8
- ¹²⁸ Basile, Andrew, *Electrochimica Acta* *56*, **2011**, 2895-2905
- ¹²⁹ US Patent# US6552843 (B1) 2003-04-22.
- ¹³⁰ Wang, Pu, *Surf. Coat. Technol.* **2006**, *201*, 3783-3787
- ¹³¹ Best, A.S. *J. Electrochem. Soc.* **2010**, *157* (8), A903-A911
- ¹³² Dilasari, Bonita, *J. Korean Electrochem. Soc.* **2012**, *15*(3), 135-148
- ¹³³ Kamavaram, Venkat, *Light Metals*, **2002**, 253-258
- ¹³⁴ Marciniak, Andrzej, *Int. J. Mol. Sci.* **2010**, *11*, 1973-1990